Micro/nano-scale manipulation of Material Properties

by

Farhana Baset

Thesis submitted to the
Faculty of Graduate and Postdoctoral Studies
In partial fulfillment of the requirements
For the Ph.D. degree in
Physics

Department of Physics
Faculty of Science
University of Ottawa

0.1 Abstract

Femtosecond laser interaction with dielectrics has unique characteristics for micromachining, notably non-thermal interaction with materials, precision and flexibility. The nature of this interaction is highly nonlinear due to multiphoton ionization, so the laser energy can be nonlinearly absorbed by the material, leading to permanent change in the material properties in a localized region of μm^3. This dissertation demonstrated the potential of these nonlinear interactions induced changes (index modification and ablation for machining) in the dielectrics and explored several practical applications.

We studied femtosecond laser ablation of poly-methyl methacrylate (PMMA) under single and multiple pulse irradiation regimes. We demonstrated that the onset of surface ablation in dielectric surface is associated with surface swelling, followed by material removal. Also, the shape of the ablation craters becomes polarization dependent with increasing fluence, except for circular polarization. The morphology of the damaged/ablated material was examined by optical and scanning electron microscopy. The dynamics of laser ablation of PMMA was simulated using a 2 dimensional Molecular Dynamics model and a 3 dimensional Finite Difference Time Domain model. The results from numerical simulations agreed well with experimental results presented in this thesis.

We also demonstrated the formation of nano-pillar within the ablation crater when the surface of bulk-PMMA was irradiated by two femtosecond pulses at a certain delay with energies below single shot ablation threshold. With increasing fluence, the nanopillar vanished and the structure within the ablation crater resembled volcanic eruption. At higher fluences we demonstrated nanoscale porosity in PMMA.

For application, a novel in-line fiber micro-cantilever was fabricated in bend insensitive fiber, that provides details of in-line measurement of frequency and amplitude of vibration, and can be further extended to be used as chemical/bio and temperature sensors. By modifying the refractive index at random spacing within the single mode fiber core, a unique quasi-random micro-cavities fiber laser was fabricated, which exhibits comparable characteristics with a commercial fiber laser in terms of narrow linewidth and frequency stability.

0.2 Sommaire

L'interaction des lasers femtosecondes avec les diélectriques démontre d'uniques caractéristiques pour la micromachinerie, notamment les interactions non thermiques avec les matériaux, la précision et la flexibilité. La nature de cette interaction est grandement non linéaire grêce à l'ionisationpar multiple photons, ce qui fait en sorte que l'énergie du laser peut être absorbe non linéairement par le matériel, causant ainsi des changements permanents aux propriétés du matériel dans une région localisée de μm^3. Cette dissertation démontre le potentiel de ces changements induits d'interactions non linéaires dans les diélectriques (modification d'index et ablation pour machinerie) et explore quelques applications pratiques.

Nous avons étudié l'ablation laser du poly-méthyle methacrylate (PMMA) sous les régimes d'irradiation d'une et de multiples impulsions. Nous avons démontré que l'initiation d'ablation de surface diélectrique est associée au gonflement de la surface, suivi par l'enlèvement de matériel. Aussi, lorsque la fluence augmente, la forme du cratère d'ablation devient dépendante de la polarisation et ce, excepté pour la polarisation circulaire. La morphologie du matériel endommagé/ablaté a été examinée par microscopie optique et électronique à balayage (SEM). La dynamique d'ablation par laser du PMMA a été simulée à laide dun modèle de dynamique moléculaire à 2 dimensions et d'un modèle de différences finies dans le domaine temporel (FDTD) à 3 dimensions. Les résultats des simulations numériques étaient en accord avec les résultats expérimentaux présentés dans cette thèse.

Nous avons aussi démontré la formation de nano-piliers à l'intérieur des cratères d'ablation lorsque la surface de la masse de PMMA était irradiée par deux impulsions femtosecondes avec un certain espacement temporel et des énergies en dessous du seuil d'ablation pour une seule impulsion. Alors que la fluence augmentait, les nano-piliers disparaissaient et la structure interne des cratères rappelait une éruption volcanique. À fluences élevées, nous avons démontré la porosité nanométrique dans le PMMA.

Pour les applications, une nouvelle fibre micro-cantilever a été fabriqueé dans une fibre infléchissable. Elle peut fournir les mesures de fréquences et d'amplitude de vibrations et peut aussi être utilisée comme capteurs chimique/bio et thermique. En modifiant l'indice de réfraction dans le coeur de la fibre à mode singulière à des espacements aléatoires, un laser à fibre à microcavités quasi aléatoires a été fabriqué. Celui-ci démontre des stabilités de fréquences et largeurs spectrales comparables à celles d'un laser à fibre commerciale.

0.3 Acknowledgements

My current thesis, including other theses that I have accomplished in graduate school and prior to, is the result of many individual's persistence, generosity, compassion, hard work and friendship. First of all, I would like to thank my family. My parents always granted me with the liberty to choose anything I wanted as my career.

I would like to thank Dr. Ravi Bhardwaj for brilliant supervision during my PhD and giving me the opportunity to be in his group and the liberty to pursue the research of my choice. I have had the opportunity of being in contact with him on a very regular basis. He always managed to make himself available to provide invaluable input on the analysis of my results, discussion and writing of all publications. Thus, he provided me tremendous help and guidance through out my graduate studies. Dr. Ravi also gave me a chance to present my work at a few international conferences. I found these conferences as a great opportunity to meet leading scientists in my field.

A big thank to Mike Wong for his help and support throughout my thesis, always having the patience to answer my numerous questions.

I would also like to thank Jean-Michel Guay, my research partner with whom I did many experiments, and Dr. Ana Villafranca for their help and their valuable input throughout the dielectric studies. I owe thanks to the rest of the group members for numerous productive discussions and for providing a good working atmosphere.

Dr. Xaoyi Bao, Dr. Ping Lu and Y. Li, University of Ottawa Physics department, who provided useful information and analysis of the fabricated fiber device, as well as constant supply of fibers to perform femtosecond modification as well as etching within the fibers.

Thanks to Dr. Lora Ramunno and Dr. Konstantin Popov, University of Ottawa Physics department, for executing the numerical simulations to support our experimental results for dielectric studies.

I would also like to thank each of the faculty members who provide me the opportunity to be a teaching assistant for them: Dr. Stadnik and Dr. Czajkowski.

The study of dielectrics would not have been possible without the support of the Science machine shop who provided a constant supply of PMMA samples, and Lucaz for LabVIEW assistance . And a special thanks to Dr. Arnaud Weck and Dr. Andrew Pelling for letting me use SEM and AFM respectively, to analyse the results of the experiments.

To all my friends and family who are the best one could ask for. They are the reason

for great joy every time I board a plane to go home.

Finally, I would like to thank my husband, Assaduz Zaman, for giving me confidence and many advices on my study and research; as well as his love, patience and support during all these years for keeping me motivated.

Acknowledgements of financial supports: The authors would like to thank Natural Science and Engineering Research Council, Canadian Foundation for Innovation and the Ontario Ministry of Economic Development and Innovation for financial support.

0.4 List of publications included in this thesis

The work presented in this thesis has been previously published in the form of several refereed journal articles and one manuscript is in process for publication.

1. **F. Baset**, K. Popov, A. B. Villafranca, J-M Guay, Z. Al-Rekabi, A. E. Pelling, L. Ramunno and V. R. Bhardwaj
   Femtosecond laser induced surface swelling in poly-methyl methacrylate
   Optics Express **21**, 12527 (2013)

2. J-M Guay, A. B. Villafranca, **F. Baset**, K. Popov, L. Ramunno, and V. R. Bhardwaj
   Polarization-dependent femtosecond laser ablation in poly-methyl methacrylate
   New Journal of Physics **14** 085010 (2012)

3. **F. Baset**, K. Popov, A. B. Villafranca, A. M. Alshehri, J-M Guay, L. Ramunno and V. R. Bhardwaj
   Nano-pillar formation by two-pulse femtosecond laser ablation in poly-methyl methacrylate
   In preparation (2014)

4. **F. Baset**, A. B. Villafranca, J-M Guay and V. R. Bhardwaj
   Femtosecond laser induced porosity in poly-methyl methacrylate
   Applied Surface Science **282**, 729-734 (2013)

Additional publications by the author

The following publication is not directly related to work presented in this thesis.

5. P. Lu, Y. Xu, **F. Baset**, X. Bao and V. R. Bhardwaj
   In-line fiber microcantilever vibration sensor
   Applied Physics Letters **103**, 211113 (2013)

6. Y. Li, P. Lu, **F. Baset**, Z. Ou, J. Song, A. Alshehri, V. R. Bhardwaj, and X. Bao
   Narrow linewidth low frequency noise Er-doped fiber ring laser based on femtosecond laser induced random feedback
   Applied Physics Letters **105**, 101105 (2014)

7. Y. Xu, P. Lu, Z. Qin, J. Harris, **F. Baset**, P Lu, V. R. Bhardwaj, and X. Bao
   Vibration sensing using a tapered bend-insensitive fiber based Mach-Zehnder interferometer
   Optics Express **21(3)**, 3031-3042 (2013)

Contents

List of Figures

Chapter 1

Introduction

1.1 Overview

Interaction between intense femtosecond laser pulse and dielectric materials leads to micro/nano scale structuring of materials by altering it's electronic, optical and physical properties. The progress of fabrication technologies compatible with a high degree of miniaturization and alteration of material properties has been followed for decades for applications in intrinsic multidisciplinary interests intersecting physics, chemistry, biology and fluid dynamics. The market of different micro/nano-manufacturing applications, such as material nanostructuring, nanoelectronics, nanophotonics and nanobiotechnology is estimated at several billion in 2020. The production of these nano-technologies requires the development of 2 dimensional (2D) and 3 dimensional (3D) dedicated tools that can lead to micro/nano-scale manipulation of material properties.

The current fabrication techniques to create micro or nanoscale patterns are photolithography [1, 2, 3], soft lithography [4], stereolithography [5], and hot embossing imprint lithography [6]. These techniques have multiple processing steps and are suitable for 2-dimensional, microscale configurations. Laser processing of materials has advantages over these fabrication techniques since it has a non-contact and flexible single step setup that can operate in air, vacuum or liquid environment, making it very attractive as manufacturing tool in many applications. The experimental evidence of light amplification by induced emission of light in a ruby crystal in 1960 [7] was preceded by theoretical proposal of light amplification by stimulated emission of radiation by Albert Einstein in 1917. Since then, the application of these radiation sources has been a key for many micro/nano-fabrication processes, with particular interest in direct laser abla-

tion and writing of devices. In laser-matter interactions, laser energy can be nonlinearly absorbed by the material, leading to permanent damage. The nature of these nonlinear interactions and the changes produced in the material has several practical applications. There is a rapid evolution of laser sources with increasing number of possible applications during the last four decades.

For the past few decades, effort was underway to produce shorter and shorter optical pulses. In the context of laser science, the term ultrashort or, ultrafast refers to the subset of pulsed lasers capable of producing light pulses with sub-picosecond pulse duration (1 ps = $10^{-12}s$) and these ultrafast laser systems are capable of achieving sub-micrometer resolutions. Ultrafast lasers became the ideal source of energy for many applications such as, industrial material processing, scientific experiments in spectroscopy and interferometry for different kinds of accurate measurements, medical applications such as cancer treatment, eye and cosmetic surgery and as a cutting tool for general surgery [8]. Moreover, ultrafast lasers have greatly impacted many aspects of human life by being used as passive optical components, such as communication, optical data storage [9, 10, 11] and sensor applications utilizing photonics technology. The advantages of multiple passive optical components, such as optical sensing and optical processing technologies can be brought together in the form of integrated optical devices [12, 13, 14], providing the compactness and reliability of miniaturized integrated systems with the aid of micro/nano-fabrication processes provided by ultrafast lasers. The fabrication of devices for these applications requires very deep knowledge of light-matter interactions and exploration of materials and micro/nano fabrication techniques to fully achieve the possibilities of this technology.

The fleeting interaction between fs laser pulses and material has enabled fundamental insight into the nature of matter. Femtosecond laser induced ablation and modification of dielectrics has been an area of intensive applied and fundamental research for over three decades. Research has been partially motivated by the possibility of femtosecond laser induced micro/nano-scale processing of dielectrics. For the most of the available commercial femtosecond laser systems, the intensity at the focus can reach 10^{13} W/cm^2 at relatively low pulse energies when the laser is tightly focused inside the transparent material. As a result, nearly any material including wide band-gap dielectrics, such as polymers and fused silica, can be easily ionized through nonlinear absorption, resulting in optically induced breakdown. Moreover, during the laser material processing, the absorbed pulse energy only can transfer to the lattice on the order of 10 picosecond (ps), which suggests the thermal relaxation time for a tightly focused femtosecond laser

pulse is even smaller than the timescale of laser-matter interaction. In contrast to the material modification using nanosecond or longer laser pulses, for the femtosecond laser interaction with the materials, an enhancement in the localization of energy deposition leads to increase in lateral and vertical precision of the ablated features. As a result, a very clean modified region with minimum collateral damage and heat affected zone can be induced, making it a promising technique for high precision micro/nano-structuring. Additionally, the nonlinear absorption process induces modification that can be confined to a very small volume with tight focusing where the local intensity is higher than the threshold for modification. Thus, by moving the transparent material relative to the focal spot of the laser beam, the focal volume located inside the bulk material can be modified without affecting the surrounding region, allowing three-dimensional microfabrication with sub-micrometer precision at any depth. By producing three-dimensionally localized refractive index changes in the bulk of a transparent material, femtosecond laser sources are opening the door to the fabrication of a wide variety of optical devices. With constant advances in ultrafast laser technology, femtosecond micro/nano-machining workstations are beginning to enter the mainstream industrial market.

Experimental discoveries have stirred interest in the understanding of the physical mechanisms behind laser-matter interactions, phase transformation, internal modification of material (permanent, or temporary) and material removal after laser irradiation, that ultimately leads to micro/nano structuring. Despite the promise of ultrashort laser pulses in processing wide bandgap dielectric materials for a variety of applications including laser surgery, integrated optics, optical data storage, and 3D micro/nano structuring, the mechanisms of inducing different structural changes in transparent materials is still not fully understood. For example, how does the crater evolve in bulk material? Does the material ablation start with direct material removal or, with surface swelling followed by the material ejection in bulk material? What is the role of polarization in the interaction of intense light pulses with solids? What could be the possible mechanism for the formation of the specific morphology of the ablation crater on the bulk dielectric surface, resulting from femtosecond laser-dielectric interaction? This thesis work addresses some of these issues, and some questions remain still open.

With the knowledge of previously explored experimental and theoretical observations, our investigations in the field of femtosecond laser interaction with transparent material began. The main objective of this thesis is to explore novel applications and gain mechanistic insight resulting from femtosecond laser-dielectric interaction. Depending on the focusing position of the laser beam, surface ablation/patterning, or bulk modification

could be realized in transparent materials using focused femtosecond laser irradiation. The work presented in this thesis deals with femtosecond laser ablation and micromachining of wide bandgap dielectric materials, such as poly-methyl methacrylate (for ablation and index modification) and single mode fiber core made up with fused silica (for refractive index modification). Poly-methyl methacrylate (PMMA) is a major polymer in the series of acrylics with a variety of applications in the field of engineering, semiconductor packaging, microelectronics and medical applications due to its biocompatibility. For PMMA, I studied damage and ablation thresholds and morphologies ex-situ, while the dynamics of ablation (initiation of ablation in bulk dielectrics with surface swelling, evolution of ablation crater and its polarization dependence, porosity) are captured with ultrafast microscopy and compared with numerical analysis. For SMF (made up with fused silica), I explored parameters for refractive index modification inside fiber and (combined with/or) efficient etching conditions. These studies demonstrate fundamental aspects of this unique laser-dielectric interaction, while exposing novel applications of femtosecond laser machining previously unexplored.

1.2 Contribution to the field

This thesis details the results of both the fundamental and the applied features of femtosecond laser ablation and modification of poly-methyl methacrylate (both) and single mode fiber (modification). In several cases our experimental results are supported by the numerical simulations. Most of these results have been published as journal articles and one manuscript is in process.

For convenience, the experiments are divided into two sets: Chapters 4 and 5 describe the single and multiple pulse ablation experiments of poly-methyl methacrylate, and Chapter 6 describes the applied part of this thesis, involving etching and/or, internal modification of single mode fiber. The samples were irradiated by 70 fs laser pulses at the center wavelength of 800 nm. The diagnostic tools used to analyse the single/multi-pulse laser ablation craters on the surface of bulk dielectrics includes optical, scanning electron and atomic force microscopy. The theoretical predictions of all these experimental results are confirmed by numerical simulation of different relevant models.

I was the primary contributor to most of the experiments related to ultrashort pulse ablation/modification, etching and writing of the majority of the manuscripts presented. These experimental results provide better understanding of ultrashort laser-solid interaction. Femtosecond laser ablation/modification of materials depends on different parame-

ters to optimize the process for a specific application. Therefore, thorough investigations have been made to identify the exact ablation mechanism. I executed all the laser ablation and modification experiments, systematic etching procedure and scanning electron microscopy, optical microscopy and the data analysis. Also purchasing and assembling of the experimental apparatuses related to this thesis was my responsibility. All the researchers who collaborated are co-authored in the publications presented in this thesis. Each publication corresponding to a specific set of experiments includes acknowledgements at the beginning of the section where each paper is presented.

While revealing the fundamental physics of underlying fs laser ablation mechanism, this dissertation also offers noteworthy practical impact related to fs laser machining of materials. The techniques and methods presented in this dissertation can be extended to a broad range of materials, and the author is hoping that suggestions for future research will yield equally worthwhile results.

1.3 Organization of the dissertation

Chapter 2 presents an overview of different micro/nano-structuring technologies and highlights the differences and benefits of ablation mechanisms with femtosecond lasers over other lasers with longer pulse durations. This chapter also provides a brief literature review of the key experiments in the study of the dynamics and a discussion of physical mechanisms of the interaction of such short laser pulses with the dielectric materials, particularly relevant to experiments and results presented in this thesis.

Chapter 3 includes the details of the laser system, experimental setup and the analytical techniques used in sample fabrication and analysis for femtosecond laser structuring. This chapter also gives a detailed description of various control parameters and their impact in optimizing the micro/nano-scale modification by femtosecond laser pulses.

Chapter 4 presents a series of experimental investigations of a single femtosecond laser pulse induced ablation of the poly-methyl methacrylate. These studies are the first systematic investigation of the onset of laser damage/ablation and evolution of the crater formation as a function of pulse energy and number of pulses on the surface of bulk PMMA. Both the damage and ablation threshold measurement were done for PMMA. The experimental analysis by scanning electron microscopy (SEM) and atomic force microscopy (AFM) reveals that the single pulse laser ablation of PMMA starts with surface swelling followed by material ejection at relatively low fluence regime. With further increase in fluence, the dimension of the ablation crater becomes polarization

dependent for single pulse ablation. This polarization dependence was also preserved for line ablation (when the laser focus is moved with a specific speed) within the quasi-periodic structures inside the ablated region. The theoretical predictions of all these experimental findings were compared with numerical simulations based on a molecular dynamics (MD) method for surface swelling experiments and with a finite difference time domain (FDTD) simulation for polarization dependent studies. Excellent agreement between experimental data and simulation was observed.

Chapter 5 deals with the multiple pulse ablation studies in PMMA. When two pulses of a femtosecond laser are incident on the surface of bulk PMMA at a certain delay with pulse energy lower than the single pulse ablation threshold, a nano-pillar is formed in the middle of the ablation crater on the surface of the bulk PMMA surface. At higher fluence, the nano-pillar disappears. The fs laser ablated craters were characterized as a function of laser fluence. The MD simulation reveals the conditions required for the formation of nano-pillar like structure. The following part of this chapter presents results from investigations regarding fs laser induced porosity within the ablation crater of PMMA as a function of laser fluence and number of laser shots. Analysis of SEM images revealed the dependence of porous area fraction and the pore size distribution with pulse energy when the laser focus was stationary. In the line ablation regime, the dependence of porous area fraction as a function of scanning speed and laser pulse energy was investigated.

Chapter 6 initiates the more applied part of the thesis. A fiber-based microcantilever vibration sensor was fabricated by chemical etching of a bend-insensitive fiber and fusing it with a single mode fiber, and offered an in-line measurement of frequency and amplitude of vibration. Experimental results were supported by theoretical analysis and detect a wide range of continuous vibration frequency (5Hz-10 kHz) with a significant signal-to-noise ratio (maximum of 68 dB). The following section demonstrates the potential of a novel compact fiber laser, fabricated by femtosecond laser modification within the fiber core with random spacing. The systematic experimental study of this quasi-random fiber laser demonstrated the presence of quasi-random micro-cavities laser with both the random and fixed cavity features, characterized by compact size, narrow-linewidth, low relative intensity noise (RIN) and high frequency stability. These investigations are the first detailed study of their respective fields. Brief investigations on microcantilever (in SMF) and microfluidic channel (in bulk fused silica) fabricated by femto-etch technique shows potential to be used as acoustic sensor and biomedical sensor, respectively.

Chapter 7 summarizes the key results obtained in this thesis and provides a broader outlook by proposing future avenues of research to address several still unanswered ques-

tions regarding femtosecond laser irradiation of dielectrics.

Chapter 2

Background

The goal of this chapter is to introduce the main mechanisms for energy absorption and deposition (resulting in rapid build up of free carriers and coupling with the lattice subsystem) in laser irradiated dielectric materials, when the photon energy is small compared to the material band-gap. An overview of different micro/nano structuring techniques along with a brief literature review of the key experiments in micro/nano-structuring is presented. This chapter also provides answers to the questions related to the advantage of femtosecond lasers as an indispensable tool for basic research in the field of laser-material interactions and explores a wide range of laser induced effects, from surface patterning/ablation to in-volume modifications in wide bandgap dielectrics. A more thorough literature review, exclusive to each set of experiments, is included in each of the papers presented in the following chapters.

2.1 Overview of Different Micro/Nano Structuring Techniques

In recent years, micro-/nanoscale machining became increasingly important due to its massive application in both research and industry for surface structuring, photonics and biomedical applications. There are wide ranges of micro-/nano-scale fabrication techniques, available in both clean room and non-clean room environments.

The contemporary fabrication techniques to create micro or nanoscale patterns are photolithography [1, 2, 3], soft lithography [4], stereolithography [5], and hot embossing imprint lithography [6] and these techniques are very advantageous in mass production of 2-dimensional, microscale configurations. Photolithography is a powerful way to create a

high resolution pattern, but multiple steps with chemical solvents are required. Besides, residual chemical agents left on the surface could be harmful for bio applications [15]. Soft lithography techniques can rapidly produce a micro-contact printing at a low cost, but this technique is still restricted by development of appropriate masters. Stereolithography requires several steps to create three dimensional scaffolds. An advantage of hot embossing is that it can print a micropattern into organic materials at low cost, but it still needs a silicon master fabricated by standard micromachining techniques. Moreover, lithography based technologies struggle to achieve 3-dimensional configurations and nanoscale geometries.

Reactive ion etching is (RIE) is another micro/nano fabrication method based on etching technology. In this method chemically reactive plasma is used to remove unwanted material deposited on wafers [16]. But damages due to high energy ions and defects because of unintentional residual deposition make this technique less attractive for micro/nano fabrication. An alternative approach to RIE is ion milling, which is a dry ion etching method. In this process, ions are accelerated and bombard the surface of the target, which is mounted on a rotating table inside a vacuum chamber [17]. Another popular technique for micro-/nano-scale fabrication is using an atomic force microscope (AFM). The AFM probe tip provides accuracy in machining as small as the size of the tip, even to nanometer precision [18, 19]. To construct sub-micron features by scratching the surface of a soft material, the sharp tip of an AFM with silicon or diamond tip etching or micromilling can be used. While this method offers flexibility to fabricate complex geometry in non-clean room environment, it is not always a worthwhile choice due to the AFM tip wear and this being a relatively slow process [15].

The next obvious choice for micro/nano fabrication process is using laser light. Laser processing has become a very attractive manufacturing tool for various applications because of having a non-contact and single-step flexible set up that can operate in air, vacuum or liquid environment. As a result, tool wear as in traditional mechanical machining is not a significant concern. For this reason, laser material processing by focused laser energy has been used in industries for many years for many different applications such as, welding, cutting, drilling, engraving, and other modification of the materials.

The choice of laser system depends on the required application. Laser radiation can be produced in two different operating modes (for example: continuous and pulsed mode) and in different media (for example: solid state, gas, dye). Based on pulse durations and operating wavelength, laser can be divided in a wide range of choices from milliseconds to femtoseconds. While nanosecond pulsed excimer gas lasers radiate in the deep ultraviolet

(UV) (wavelength 157 to 351 nm), femtosecond or millisecond pulsed solid state lasers radiate at 266 to 1070 nm. Example of continuous wave (cw) operated laser is CO_2 gas laser, which radiates in the IR (10.6 mm) and is generally used for macroscopic processing.

Nd:YAG, CO_2, Excimer, and copper vapor lasers are mostly used as a non-contact and non-clean method [20, 21, 22, 23, 24, 25, 26]. For wide bandgap dielectric material, Ultra Violet (UV) laser and Excimer laser are generally used because of the high absorption properties of the dielectric material. Pulse-widths of these laser systems usually range from continuous wave (CW) through milliseconds to hundreds of picoseconds. The interaction of these lasers with dielectric material induce photochemical reaction which enables micro/nano fabrication [22, 23, 25, 27]. The drawbacks that made these nanosecond lasers a rather disadvantageous option for industrial applications are corrosive gas handling and UV radiation damages [28]. Also, during conventional laser material processing, the region surrounding the laser irradiated zone experiences thermal effects due to the heat diffusion process and leads to a heat affected zone (HAZ) in the material. The HAZ consists of microcracks and voids, and the material properties can change permanently. This HAZ appears because the pulse-width of most conventional laser systems are longer than the time required for thermal diffusion of the most materials, resulting in significant penetration length of thermal diffusion in the material , leading to a HAZ. Therefore, utilizing conventional laser system may lead to limitations for micro/nano-scale laser-material processing.

2.2 Advantages of using femtosecond lasers

The advent of ultrashort pulsed lasers has initiated a whole new field of scientific investigations by overcoming some limitations of long pulse laser system for micro and/or nanoscale fabrication. Pulse duration of laser systems with typically less than 1 picosecond (10^{-12} s) are generally referred to as femtosecond lasers or ultrashort pulsed lasers. Typical laser-material interactions for the ultrashort pulse duration are quite different from the long-pulsed laser case due to several unique characteristics of ultrashort laser pulses. Very fast processes, such as, electron-phonon scattering, phonon vibration, chemical bond breaking can be measured directly by time resolving with fs laser pulses. A short pulse is also able to create extremely nonequilibrium conditions. For example, a fs pulse can excite electrons to a very high temperature, while the ions are still cold since valence electrons respond much promptly to the short pulse compared to the ionic

core. Also, ultrashort pulsed lasers (femtosecond and picosecond lasers) are capable of achieving very high peak laser intensity with low pulse energies. With pulsed lasers, the intensity of peak instantaneous power can be drastically increased by decreasing the pulse duration [29]. For example, a laser pulse with a pulse-duration of 100 fs and pulse energy of 0.33 mJ when focused to a diameter of 20 μm yields a peak intensity of 10^{15} W/cm^2. For a 10 nanosecond laser pulse to acquire the same intensity, pulse energy of 100 J would be required [28]. Such enormous intensities can be achieved with a table-top fs laser system, that may lead to nonlinear processes and evoke efficient absorption in wide bandgap materials. The nonlinear nature of the laser energy deposition mechanisms confines any subsequent material change to the focal volume with submicrometer precision. This spatial confinement associated with laser-beam scanning or sample translation, makes it possible to micromachine geometrically complex structures in three dimensions.

During the excitation of the electrons by a fs laser pulse, laser energy is deposited to the substrate at a time scale much shorter than both the heat transport (micro- to nanoseconds) and the electron-phonon coupling (nano- to picoseconds). The resulting light-matter interaction process becomes essentially frozen in time, minimizing collateral damage to the region around the focal spot and decoupling thermal effects from the excitation [30]. The ultrashort pulse is completed earlier than hydrodynamic expansion and material removal. As the ablation process can be temporally separated into energy deposition and material removal, the ejected material does not interact with the laser pulse. The combined effect of femtosecond laser ablation results in an improvement in the localization of energy deposition with reduced shock and heat affected zone (limiting the penetration depth of thermal diffusion in the material) leading to precise ablated features. Furthermore, femtosecond laser processing is known to be a deterministic process since it is independent of the defect electrons to be required to seed the absorption process. On the other hand, a large quantity of seed electrons are generated through nonlinear ionization from the first tens of femtoseconds of the pulse. The confinement and repeatability of the nonlinear excitation make it possible to use the femtosecond laser-induced damage for practical purposes.

2.3 Femtosecond versus nanosecond laser ablation

There are some qualitative differences in the damage mechanisms for long and short laser pulses, which contributes to the final state of the ablated morphology. Optical damage depends on laser fluence (or, on laser intensity) as well as on pulse duration.

The fluence (energy per unit area) required to produce damage increases with pulse duration whereas, the intensity required to produce laser damage decreases with pulse duration. For comparatively longer pulses (pulse durations longer than a few tens of ps),

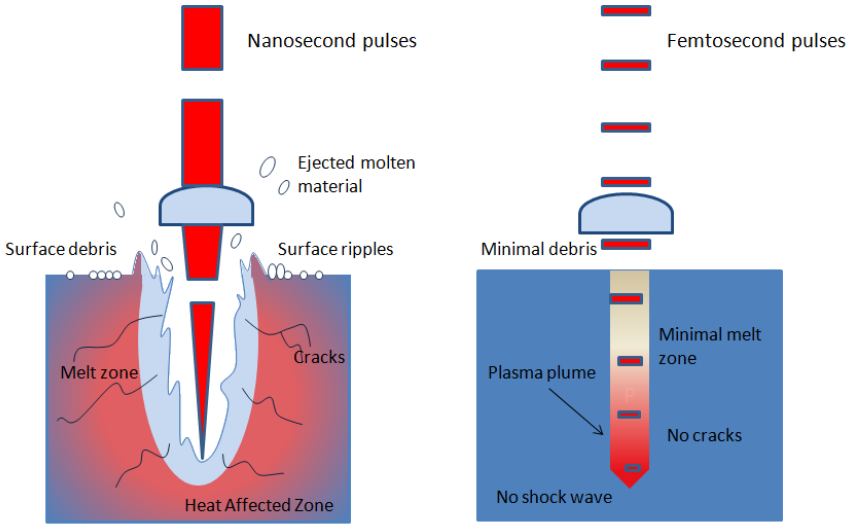

Figure 2.1: Schematic diagram shows a comparison between nanosecond (left) and femtosecond (right) laser pulses. This demonstrates the absence of thermal damage (such as, melt, cracks and heat affected zone) (left) using sub-picosecond pulses which are shorter than the thermal expansion time.

a substantial amount of energy is transferred by thermal diffusion from the laser excited electrons to the lattice on the time scale of the pulse duration. Then the temperature of the laser irradiated region becomes sufficiently high to melt or fracture, leading to permanent damage of the material [31]. Since the damage threshold is determined by the relative rate of energy deposition and thermal diffusion, the threshold fluence for optical damage will scale as the square root of the pulse duration [32]. But this scaling dependence deviates for pulses shorter than 10 ps [33].

As explained in section 2.5.1, for nanosecond pulse duration, avalanche ionization is assumed to be the dominant mechanism of laser induced breakdown; whereas multiphoton ionization is the key mechanism for ultrashort pulses. For ultrashort pulses, the nonlinear absorption occurs on a time scale shorter than the time scale for energy transfer to the lattice, resulting in negligible coupling between the absorption and lattice heating processes [34]. Electrons in the conduction band are heated by the laser pulse much faster than they can cool by phonon emission, diffuse out of the irradiated volume,

or, recombine with their parent ion. The energy is transferred from the electrons to the lattice only after the laser pulse is gone. This rapid deposition of energy into the material on a time scale much shorter than the thermal diffusion time, leads to ablation of material on the surface or permanent structural change in the bulk.

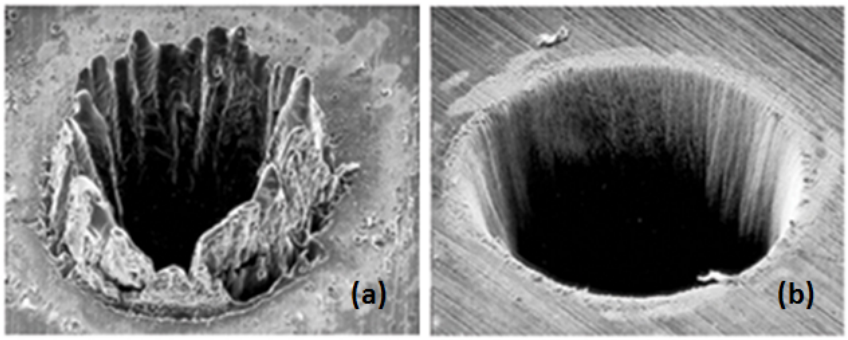

Figure 2.2: Ablation of stainless steel using nanosecond pulses (left) and femtosecond pulses (right). This demonstrates the absence of thermal damage (left) using sub-picosecond pulses which are shorter than the thermal expansion time. Image obtained from [35], with permission from Springer.

Additionally, short pulses require less energy than longer pulses to reach the intensity necessary to produce optical breakdown. As a result, they deposit less energy in the material. Less energy deposition leads to an improvement in the localization of energy deposition, which results in more precise ablation or bulk material modification with reduced heat and shock affected zone. Furthermore, femtosecond pulse does not interact with the ablated material while longer pulses result in sputtering of the target surface, since considerable amount of laser energy can be absorbed in the ablated plasma plume. Figure 2.1 shows the difference between femtosecond and nanosecond laser pulses when focused onto a small spot size of micrometer scale. For example, when a 10 fs laser pulse with energy of 1 mJ is focused to a 20 μm spot diameter, the resulting peak intensity is on the order of 3.19×10^{18} W/cm^2. To generate the same amount of peak intensity with the same spot size, the ns laser pulses require 10^5 times (1000 J) the energy required by fs laser pulses.

Figure 2.2(a) shows a scanning electron micrograph (SEM) of a crater produced by nanosecond laser pulses (pulse width $\sim$33 ns) on stainless steel. A significant portion of solidified droplets are ejected with the formation of high-rim crater. It is obvious from the SEM image that the particles deposited on the sample surface are produced

by the ejection of molten material which is a direct consequence of the thermal effects characteristic of nanosecond laser ablation. The situation is different when femtosecond laser pulses are used for ablation. Figure 2.2(b) shows an SEM image of femtosecond laser (pulse width ∼200 fs) ablation of the same stainless steel having different properties. The ablation craters are clean and the effect of thermal melting is very much reduced [35].

2.4 Ultrashort laser pulses in transparent materials

The work presented in this thesis deals with several aspects of the interaction of intense femtosecond laser pulses with transparent materials. A femtosecond pulse with only moderate energy can have an extremely high peak power and peak intensity, that can lead to nonlinear response of the material. When a tightly-focused femtosecond pulse is focused inside transparent material, it initiates laser-induced optical breakdown by which optical energy is transferred to the material causing ionization of a large number of electrons. As a result, the ionized electrons can cause permanent material modification by transferring energy to the lattice. Together with the tight focusing and the nonlinear nature of the absorption, the absorption becomes confined to the focal volume inside the bulk of the material without causing any absorption at the surface, resulting in localized deposition of energy in the interior of the sample. On a later time-scale, this leads to a phase or structural modification, leaving behind a localized permanent change in the index of refraction. Besides, the interaction of a high energy laser beam with a solid surface can result in laser ablation; a process in which material are removed from the sample surface [36].

The processes involved in laser-solid interactions are complicated and the mechanisms of interactions are different depending on the type of the material (conductor, semiconductor, or dielectric) and on the laser characteristics (wavelength, pulse duration, and fluence). The majority of the results presented in this thesis are outcomes from laser ablation and modification of poly-methyl methacrylate and single mode fiber made up with fused silica, which are classified as wide bandgap dielectrics. This section will review some of the basic physics that governs how femtosecond laser pulses behave in wide bandgap dielectric materials.

2.5 Laser induced breakdown

The dynamics of the ablation process can be divided roughly into two stages: the photon energy absorption, primarily through free electron generation and heating, and the redistribution of the absorbed energy to the lattice, leading to material removal [37], which will be discussed in the following subsections.

2.5.1 Energy absorption by nonlinear ionization

Laser-induced breakdown is initiated when a significant amount of laser energy is absorbed by the target material, which leads the material to transform into an absorbing plasma by the intense laser pulse [28]. Such breakdown occurs when the density of electrons (known as critical plasma density) reaches approximately 10^{18} cm^{-3} for nanosecond or longer laser pulses and 10^{21} cm^{-3} for femtosecond laser pulses of wavelengths in the visible and near IR [28, 38]. These high electron densities provide strong optical absorption in the plasma that can cause strong heating and damage to the material [38].

The beginning of laser induced breakdown requires the presence of seed electrons, whose mechanisms depend on the inherent material properties [38, 28]. In metals, free conduction band electrons are able to directly absorb the incident laser energy through single photon absorption (linear absorption) and rise to higher energy levels [28]. The electron energy is then transferred to the lattice via electron-lattice collisions, which leads to material breakdown. If sufficient energy is deposited into the surface of a material through linear absorption, material ablation can occur. For materials which are transparent to the laser wavelength such as transparent dielectrics, there are no free conduction band electrons available to absorb the incident laser photons. Moreover, the valence electrons are so firmly bound to their nuclei that their ionization potential is greater than the incident laser energy. Thus, the interband excitation in dielectrics can only occur if the incident photon energy exceeds the bandgap energy of the dielectric material. As a result, at lower laser intensity, the bound electrons do not absorb the laser light. So how can laser-induced breakdown be initiated in such a transparent dielectric material? The answer is, nonlinear processes such as multiphoton ionization and avalanche ionization are necessary to promote the initial creation of the free-carriers [39, 40, 37, 41]. As reported in the literature, these nonlinear processes are briefly discussed in the following sections.

Photoionization

Photoionization refers to direct excitation of the electron by the laser field. Depending on the laser frequency and intensity, there are two different regimes of photoionization, the multiphoton ionization (MPI) regime and the tunneling ionization (TI) regime. High intensity, achieved by peak power in fs laser ablation, makes it possible to simultaneously absorb multiple photons and to create high electron densities through photoionization as well as localized plasma formation through avalanche ionization. All of these subsequent processes lead to permanent damage and ablation.

At high laser field strength ($>10^9$ W/cm^2) and high laser frequencies (but not high enough that single photon absorption can occur) of femtosecond laser pulses, nonlinear ionization is usually described in terms of the simultaneous absorption of several photons by an electron, shown in Figure 2.3(a). A bound electron can be lifted from its bound energy level, or valence band, to the free energy level, or conduction band, by simultaneously absorbing n photons. That is, the number of absorbed photons times photon energy should be equal or greater than the ionization potential, or bandgap ($n\hbar\omega \geq E_g$, where E_g is the bandgap energy, ω is the laser frequency, $\hbar$ is Planck's constant, and n is the minimum number of required photons to cross the bandgap) [42, 28]. For example, if the wavelength of the laser is 800 nm, the laser photon energy is calculated to be 1.55 eV. It requires at least 4 photons absorption for a material with 6 eV of ionization potential. For this reason, it is called multiphoton absorption. Since multiphoton ionization is an n-th order process, it is significant only at very high laser field strength.

For strong laser fields and comparatively low laser frequency, nonlinear photoionization is governed by the tunneling process. In tunneling ionization, the electric field of the laser suppresses the Coulomb well that binds a valence electron to its parent atom. If the electric field is very strong, the Coulomb well can be suppressed enough that the bound electron tunnels through the short barrier and becomes free, as shown schematically in Figure 2.3(a).

The transition between multiphoton ionization and tunnelling ionization was expressed by Keldysh in terms of the adiabaticity parameter, also known as the Keldysh parameter [43, 44, 45, 46]. This parameter is defined as,

$$\gamma = \frac{\omega}{e}\sqrt{\frac{mc\epsilon_0 E_{\mathrm{g}}}{I}} \tag{2.1}$$

where ω is the laser frequency, I is the laser intensity, m and e are the mass and charge of an electron, c is the speed of light, E_{g} is the bandgap of the material, and ϵ_0 is the

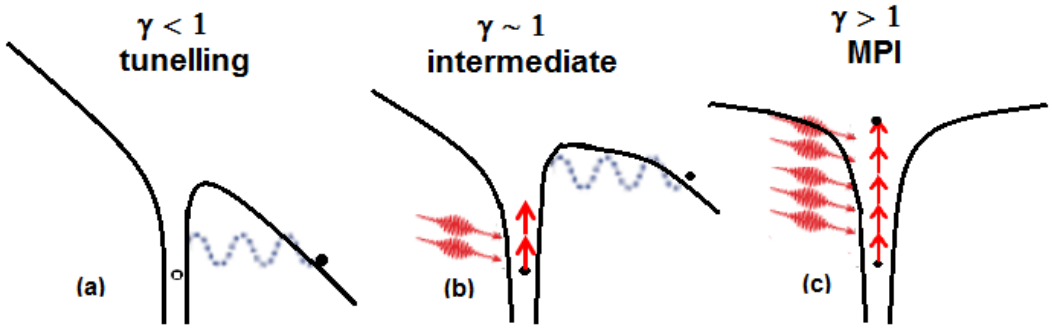

Figure 2.3: Schematic diagram of photoionization for different values of the Keldysh parameter.

permittivity of the free space. Keldysh concluded that, multiphoton ionization prevails over tunneling ionization when Keldysh number is $\gamma >> 1$, and tunnel ionization prevails over MPI when $\gamma < 1$ [47]. In the intermediate regime, the photoionization is a mix between tunneling and multiphoton ionization as depicted in Figure 2.3(b).

The photoionization rate depends strongly on the laser intensity. The rate of multiphoton absorption is proportional to the intensity of the laser radiation [28]. In the multiphoton ionization regime, the rate is $P(I)_{MPI}=\sigma_k\ I^k$ where, σ_k is the multiphoton absorption coefficient for k-photon absorption [48].The number of photons required is determined by the smallest k which satisfies the relation $k\hbar\omega \geq E_g$. Conversely, the tunneling rate scales more weakly with the laser intensity than the multiphoton rate.

The photoionization rate and Keldysh parameter as a function of laser intensity has been explored for 800 nm light in fused silica (7.5 eV band gap) [47]. Researchers have successfully fit their data using rates from Keldysh's theory [34, 31]. Simulations for other laser wavelengths and material band gaps consistently show the very abrupt transition from a multiphoton to tunneling regime at a Keldysh parameter of about 1.5. Some recent experiments have called Keldysh's theory into question. Lenzner et al. found that they could not account for the pulse duration dependence of the surface damage threshold of fused silica with the ionization rates predicted by Keldysh, and that the multiphoton ionization coefficients that best fit their data were several orders of magnitude smaller than those predicted by Keldysh's theory [49]. More experimental and theoretical work is necessary to resolve this issue.

Avalanche ionization

As mentioned earlier, at low intensities the bound electrons do not absorb the laser energy, and to initiate a laser-induced breakdown seed electrons are required. These seed electrons can be supplied by thermal excitation from impurity states (naturally present in any material) into the conduction band, but the intensities available with femtosecond pulses are high enough that even in the absence of any free carriers, avalanche ionization can be seeded by carriers that are directly photoexcited by multiphoton or tunneling ionization [50, 28]. An initially free electron linearly absorbs several laser photons through free-carrier absorption, then impact ionizes another electron. The accelerated seed electrons are excited by the high electromagnetic field of the incident laser radiation and gain enough kinetic energy to release bound electrons by colliding with them (impact ionization). During this collision nearly all of the free electron energy is transferred to the bound electron. The newly freed electrons gain enough energy to free more electrons, and repeating itself, creating an avalanche effect (Figure 2.4): the density of free-electron increases exponentially. The longer the pulse is, the higher is the density of free electrons as well as the probability of collisions, which grows into an avalanche process with longer pulse durations [51, 28, 34]. Therefore, the avalanche ionization process can be summarized by stating that, as the leading edge of the pulse approaches the focus, photoionization processes begin to promote electrons from the valence band to the conduction band, and these free electrons act as the seed for avalanche ionization, which exponentially increase the free carrier density as the most intense section of the pulse arrives.

In contrast to damage produced by longer pulses, damage in transparent materials caused by femtosecond lasers exhibits a sharp threshold, and is significantly more deterministic in nature. The reason is that the intensities produced by femtosecond pulses are high enough to allow multiphoton absorption early in the pulse. Therefore, MPI produces a large number of free carriers that seed the avalanche, and so the onset of damage is much less statistical, making it straightforward to identify a particular damage threshold. For nanosecond and longer laser pulses, ionization occurs through avalanche ionization alone, which relies on the presence of low concentration (i.e. about 10^8-10^{13} cm^{-3}) of free electrons due to metal impurities or, thermally excited carriers. The number of these free carriers within the focal volume of tightly focused pulses is ~ 1. Moreover, the number of these free carriers can vary significantly from volume to volume within the same sample, leading to statistical behavior in exhibiting threshold for damage, which explains

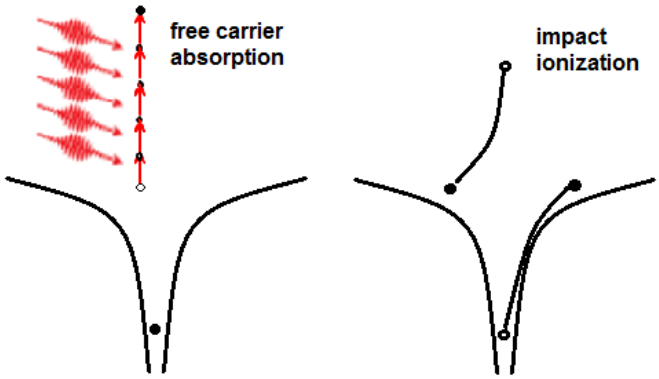

Figure 2.4: Schematic diagram of avalanche ionization. Several laser photons are linearly absorbed by an initially free electron through free-carrier absorption, then impact ionizes another electron. The electrons are promoted from the valence to the conduction band in a solid, as shown in Figure 2.3, rather than ionized.

the large fluctuations in the threshold fluence required to produce laser-induced breakdown with nanosecond laser pulses [51, 52]. But the nonlinear processes (avalanche and multiphoton ionization) occur simultaneously during the laser-material interaction; for fs pulses, photoionization takes place during the leading edge of the pulse and avalanche ionization during the trailing edge of the pulse [53]. Hence it is difficult to assess the contribution of each channel and more experiments are needed to quantitatively clarify the relative role of different ionization mechanisms.

A model of avalanche ionization was developed by Stuart et al., where the avalanche rate depends linearly on the laser intensity such that, $\eta\alpha = I$. Here α is the avalanche ionization coefficient and η is the avalanche ionization rate [34]. According to the Drude model, the heating of the electrons in the conduction band is taken into account. Stuart's model also makes the flux doubling approximation, which states that an electron in the conduction band impact ionizes an electron from the valence band as soon as it has enough energy to do so. This model also assumes that the energy distribution of electrons in the conduction band does not change shape as the electron density grows. Recently, some researchers have raised questions regarding this model [54, 52]. For example, Thornber predicts an avalanche rate that depends on the square root of the laser intensity [55]. More experimental and theoretical work is necessary to resolve and accurately model the dependence of avalanche ionization on laser intensity.

During femtosecond laser irradiation, it takes some time to build up avalanche ion-

ization. When the pulse duration is extremely short (< 100 fs), the contribution from avalanche may be insignificant because only few cycles of avalanche can be involved, depending on the collision time of the specific material. As the multiphoton and avalanche processes further ionize the bound electrons, plasma with a critical density is created, and this initiates the breakdown of transparent material. The critical plasma density refers to the electron density that is grown through avalanche ionization until the plasma frequency of the electrons in the conduction band equals the frequency of the incident laser radiation. Subsequently, the dielectric material becomes more absorbing (the absorption, initially is negligible due to the very low free-electron density). Close to the ablation threshold, the free-electron density in the conduction band of the dielectrics is in the order of 10^{21} cm^{-3} [56]. At this stage it is expected that a large fraction of the laser pulse energy will be reflected while the rest of the pulse energy will be absorbed in the focal volume which leads to permanent damage in the material [57, 58].

2.5.2 Plasma defocussing

Beside strong absorbing effect at high intensity, the complications associated with self-focusing comes into effect. Self-focusing results from the intensity dependence of the refractive index, given by the total refractive index $n{=}n_0{+}n_2 I$, where n_0 is the ordinary (low I) refractive index and n_2 is the nonlinear index. In other words, the spatial variation of the intensity profile of the laser pulse leads to a variation in the spatial refractive index profile in dielectrics. Since n_2 is positive in most materials, the refractive index is higher at the centre of the beam compared to the wings. This variation in refractive index acts as a lens and tends to focus the laser beam inside dielectric. With increasing pulse power, the self-focusing becomes stronger until the critical power of the self-focusing is achieved, which can be expressed by the following equation [51],

$$P_{cr} = 3.77\frac{\lambda^2}{8\pi n_0 n_2} \tag{2.2}$$

At the peak power of the laser pulse P_{cr}, it balances diffraction and a filament is formed. If the peak power of the laser pulse exceeds further this critical power for self-focusing, the laser beam will collapse catastrophically within the material causing damage.

In practice, other mechanisms (such as, plasma defocusing) stop the collapse of the beam inside the dielectric due to self-focusing. In particular, as the laser beam self-focuses, the intensity rises and eventually becomes sufficient to nonlinearly ionize elec-

trons and generates electron-hole plasma inside the material. Due to nonlinear ionization, the plasma can have a defocusing effect on the laser pulse. This defocusing effect results from the negative contribution of the free electrons to the refractive index. Because of the typical Gaussian spatial intensity profile of the beam, the spatial distribution of the electron density is the highest at the center of the beam and decreases radially outward. The real part of the refractive index (n) is modified by the generation of the electron-hole plasma, satisfying the following condition, $\omega_p/\omega \ll n_0$, where ω_p is plasma frequency and ω is laser field frequency), and can be expressed by the following expression [59],

$$n = n_0 - \frac{N}{2N_0N_e} \tag{2.3}$$

where N_e is the characteristic plasma density for which the plasma frequency is equal to the laser frequency, ϵ_0 is the electric permittivity and m^* is the effective mass of electron. The plasma density can be expressed by the following equation,

$$N_e = \frac{\omega^2\epsilon_0 m^*}{e^2} \tag{2.4}$$

When the plasma density reaches 10^{17}-10^{18} cm^{-3}, it leads to a decrease in refractive index. Accordingly, the refractive index is the smallest on the beam axis and this spatial distribution of the refractive index (i.e. electron plasma) forms a negative lens. As a result, the beam is defocused by the plasma which acts as a diverging lens. The negative contribution to the refractive index due to the plasma balances the nonlinear index n_2, which in turn balances self-focusing [60]. Moreover, the unique mechanism of plasma defocusing limits the intensity achieved in self-focusing phenomena.

2.5.3 Energy transfer

Following the material breakdown process, launched by raising the free electron density to a critical value, the free electrons thermalize within the electron subsystem via carrier-carrier scattering in several tens of femtoseconds. The energy is transferred from electrons to the lattice by electron-phonon relaxation on a timescale ranging from a few 100 fs to a few picoseconds, depending on the material [61, 62].

Despite numerous experimental and theoretical investigations, there exist a few disputes in predicting the dissipation of the absorbed energy into the lattice and the subsequent material removal mechanisms during ultrashort laser ablation in dielectrics [63]. The precise phase change mechanism relies on the absorption characteristics of specific

classes of materials and the strength of the electron-lattice interaction [63]. The primary phase change mechanisms are thermal processes (non-equilibrium thermal vaporization and melting) and non-thermal processes (the Coulomb explosion and electrostatic ablation). While nonlinear effects and short timescales associated with femtosecond lasers are expected to lead ablation through nonthermal material removal, complex morphologies perceived on the ablated dielectric surface imply the opposite [64, 65].

After a thermal equilibrium is attained between atoms and electrons, the lattice will eventually attain a specific temperature that will lead the lattice to go through a volumetric phase change along with material decomposition. Since extreme temperature of the material induces the material disintegration, this mechanism is known as thermal ablation. An alternative to the thermal ablation method is a non-thermal ablation process, also termed as Coulomb explosion. Due to the generation of free electrons, there exists Coulomb forces among the atoms. In the Coulomb explosion process, the decomposition of material is triggered between electron cloud and atoms by the repulsive forces, resulting from Coulomb forces between the two subsystems [66]. Both thermal and non-thermal ablations contribute to the formation and expansion of plasma during femtosecond laser irradiation.

For femtosecond laser ablation of dielectrics, the Coulomb explosion (non-equilibrium thermal ablation) is widely accepted to be the prevailing mechanism when the laser fluence is above the threshold fluence. At that fluence for ultrashort pulses, as opposed to long pulses (>10 ps), melting is considerably reduced and insignificant, since the hydrodynamic (liquid phase) motion of dielectrics is generally negligible. When the temperature reaches higher than the vaporization temperature, material will be removed. But if this negligible amount of melting is taken under consideration, the phase change will occur when the lattice attains the temperature higher than the melting temperature (specific temperature at which any specific material softens) for dielectrics. Besides, since this melted area of the dielectric surface is strongly ionized, this molten region can be ablated by the pressure and strong electric field generated by the femtosecond pulse [67].

2.5.4 Subsequent processes

Once the energy is transferred to the lattice, several processes occur at nanosecond timescale. For example, a pressure or a shock wave separates from the dense, hot focal volume within a couple of nanoseconds [68, 69], followed by the thermal energy diffusion out of the focal volume on the microsecond timescale. When the energy becomes high

enough, these combined processes lead to melting or, non-thermal ionic motion and leave behind permanent structural changes [70].

The high density plasma generated by intense illumination of dielectrics at high intensities becomes very energetic due to efficient absorption of light, as discussed in previous sections. The laser heated plasmas are expanded, followed by a hydrodynamic expansion of the ablated material, resulting in the ejection of fast ions within a few ps after the initial excitation [71, 72]. Numerous theoretical investigations have attempted to explain the fundamental mechanisms leading to material removal including: spallation, explosive boiling, vaporization and melt expulsion [73, 74, 75]. The initiation of a precise expansion mode depends on the amount of energy absorbed and material composition.

When the incident laser fluence is slightly increased beyond the damage threshold (minimum fluence at which damage to the target is induced) of any particular material, the fast energy deposition of a short-pulse laser leads to an abrupt temperature rise in the focused area. As a result spallation occurs, causing mechanical fracture of brittle material or, promoting cavitation and fragmentation in a metastable liquid, due to accumulation of high tensile stresses at the laser irradiated spot [76].

As the fluence is further increased, the irradiated surface can overheat beyond the limit of its thermodynamic stability, leading to phase explosion or, explosive boiling [76]. The phase explosion is a process where a system is pushed into a metastable region as a result of rapid heating and the superheated metastable liquid undergoes an explosive liquid-vapor phase transition into a stable two-phase state because of a massive homogeneous nucleation of vapor bubbles. This process is followed by an explosive decomposition of the overheated material into a mixture of vapor and liquid droplets. Eventually, the ultrashort pulse irradiated surface becomes melted and the molten material is heated beyond its thermodynamic boiling temperature, leading to bubble formation followed by ejection of material. Below the threshold fluence for plasma formation, phase explosion is known to be the key mechanism in femtosecond ablation [77].

On the other hand, at a fluence above the threshold of plasma formation, a layer of material surface can be atomized and removed through vaporization. Here, vaporization is not indicated by evaporation from the surface layer; instead vaporization illustrates complete dissociation of the material as the absorbed energy exceeds the cohesive energy of the lattice [78, 79].

2.5.5 Final state of the ablated material

In the femtosecond pulse ablation regime, the timescale for the overall ablation process is on the order of several 10 ns. The timescale associated with the transfer of absorbed optical energy by the electrons to the lattice is over a picosecond, followed by separation of a pressure or a shock wave from the dense hot focal volume within a few nanoseconds. The thermal energy diffuses out of the focal volume on a microsecond timescale [80]. This shock-like deposition of energy into the material, on a time scale much faster than the thermal diffusion time, leads to ablation of material on the surface or, permanent structural change in the bulk. The final state of the material relies on the amount of absorbed energy, material removal mechanism and successive cooling rates. This final state of the ablated material can be characterized by its morphology, crystal structure and chemical composition. The work presented in this thesis is carried out with laser beams that have a near Gaussian spatial profile. Therefore, the energy deposition is not uniform across sample surface which affects the morphology of the ablated region by varying the associated density and temperature gradients. By carrying out a postmortem analysis on the ablated/modified region, analysis of fluence dependent features (i.e. crater profiles, crater depth, crater diameter, local changes in crystallography and chemistry) can be correlated to different dynamic mechanisms.

For example, the analysis of the depth of the ablated craters can offer an approximation of the energy deposition profiles. Other than fundamental investigations, the postmortem analysis can provide a huge variety of information relevant for practical applications of ultrashort laser pulse in material processing and micro/nanomachining. For instance, analysis of the final state and fluence dependence of ablated volume or, crater depth can estimate the ablation threshold and ablation rates. Also, the interaction of intense femtosecond lasers with material surface induces locally modifying the physical state, mechanical, optical, and chemical properties, that might have potential application in mesoscopic research.

2.5.6 Dielectric modification

In a wide band-gap material, several common processes including stress-induced changes, densification, changes in effective temperature, color center formation and ion diffusion, are responsible for the observed change in refractive index. The relative importance of each mechanism varies significantly according to the material properties and laser exposure parameters [80]. For example, SiO_2 a 5 membered ring structure is also known

as fused silica. The exposure of appropriate laser parameters inside SiO_2 will change the chemical affinity of the sample along the laser illuminated path. The resultant laser-silica interaction leads to bond breaking, and the 5-membered ring is reduced to 3, resulting in densification and refractive index modification [81].

In transparent materials, the threshold for producing permanent structural change coincides with the threshold for optical breakdown and plasma formation [31]. When the laser intensity exceeds the threshold intensity due to the high atomic density of the medium, a critical plasma is formed, which is restricted to expand and is confined to the interaction region, as the temporal peak of the pulse passes through the laser focus. Therefore, unlike surface ablation, the plasma is confined to the interaction region and is not free to expand. This plasma strongly absorbs energy from the second half of the laser pulse, depositing enough energy to produce permanent structural change.

For femtosecond laser pulses, breakdown occurs even with less energetic laser pulses, leading to less energy deposition and smaller structural changes. Therefore, there is no ablation and removal of material. Instead, with suitable laser exposure conditions, a permanent and localized increase in the refractive index is possible [82]. Because the absorption in a transparent material is nonlinear, it can be confined within a micrometer sized volume, or even smaller than the focal volume [83, 81, 84].

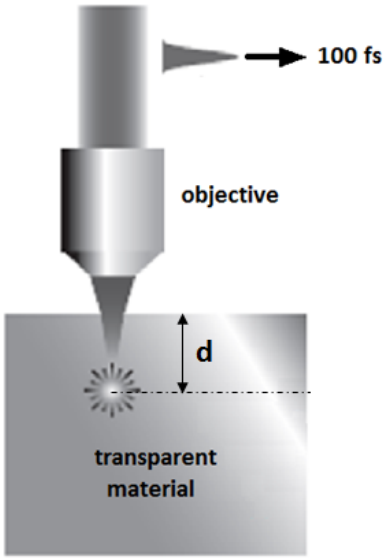

Figure 2.5: Schematic diagram of the focusing setup used to produce structures in bulk dielectric using femtosecond laser pulses. The beam was focused at a depth d μm from the surface.

The extent of modification to the refractive index within the focal volume is dependent on the change in the density induced within that region, in accordance with the energy delivered to the interaction region [83]. There are three major phenomena reported in the literature when focused intense fs pulses interact with transparent dielectrics with increasing intensity: such as, smooth refractive index changes, birefringent zones and microvoid disruptions. When the fs laser pulses have energy close to the threshold, it results in uniform refractive index change of the material, which is called isotropic refractive index change (Δn) for a very short range of pulse width and fluence. This uniform modification, achieved by scanning the laser focus through the material, has been associated with uniform positive refractive index changes (of the order of 5×10^3 for fused silica) and is suitable for writing a three-dimensional object, which is widely known as a low loss optical waveguide [85]. Waveguides, the basic building block of any photonic device, have a higher refractive index in the laser modified region compared to the surrounding regions as shown in Figure 2.6. This makes them ideal to guide optical waves by total internal reflection. Conversely, this smooth modification range is not suitable for fabrication of microchannels since the etching selectivity is very weak.

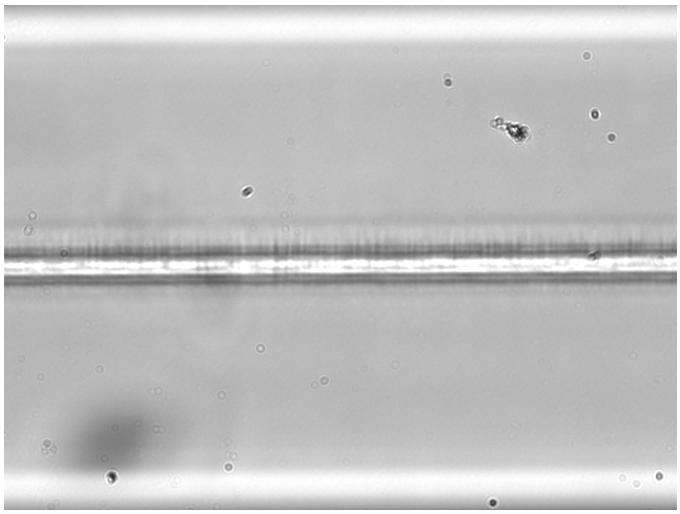

Figure 2.6: Results obtained from experiments done with a single mode fiber. The laser beam focused inside the core of single mode fiber, created plasma in a confined region causing a chemical re-structuration within the interaction region which leads to permanent refractive index changes within the core. This picture was taken by a CCD camera mounted to an optical microscope using a 40x objective.

At moderate energies and under some specific conditions, the modifications within the focal volume would transform into self-ordered multiple periodic regions with the modification confined to nanometer dimensions. Such modification leads to the formation of nanostructures; commonly known as the birefringent refractive index change mechanism. The nano-planes, as shown in Figure 2.7, are oriented perpendicular to the electric vector of the laser beam and created as an outcome of localized ionization and linearly polarized laser-plasma interaction. This leads to interference phenomena between the incident light field and the electric field of a bulk electron plasma wave and results in periodic modulations in the electron plasma density. Consequently the non-uniform nano-plasmas will randomly grow into nano-planes due to local field enhancements. These nanostructures inside a material have a wide field of applications from building of gratings to 3D optical data storage devices [86]. Figure 2.7 shows periodic nanostructures inside fused silica at a separation of ≈250 nm using a central wavelength of 800 nm and 50 fs pulses [81].

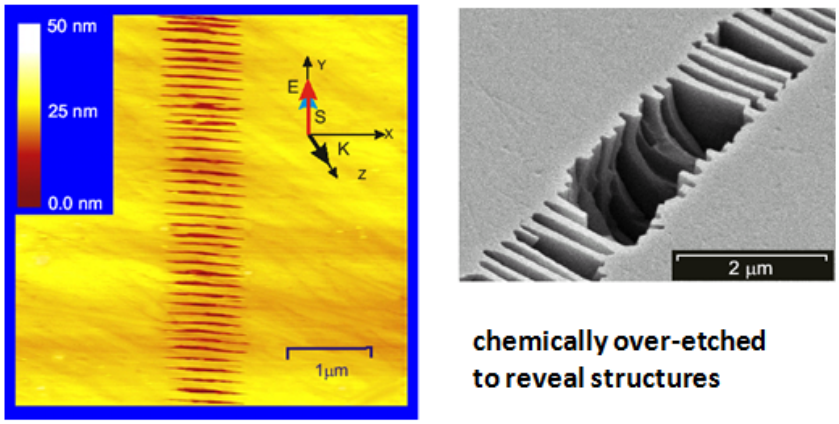

Figure 2.7: Atomic force micrograph of the periodic array of nanoplanes obtained by scanning (**S**) the focus along the polarization direction (**E**). The periodicity is ∼250 nm for 800 nm light inside fused silica. Image obtained from [81], with permission from the Institute of Physics (IOP).

An interesting outcome of the polarization-selective etching experiment of the generated nanogratings is that, it exhibits dramatic differences in the etch rate for different orientations of the electric field vector with respect to the writing direction [87]. When the modification is induced by linearly polarized light perpendicular to the writing direction, the generated nanogratings will be aligned with the writing direction and the resulting

cumulative etch rate will be very high as the acid flow will be virtually unobstructed and proceeds along large distances in a parallel fashion. Therefore, this particular modification range is very suitable for fabrication of microchannels due to the strong etching selectivity.

With further increase in energy, the modification leads to void formation. At such high laser energy, hot electrons and ions may explosively expand out of the focal volume into the surrounding material [88]. This explosive expansion leaves a void or, a less dense central region surrounded by a denser halo. During the laser processing of polymers, cross-linking and depolymerization are two further mechanisms which can influence the resulting morphology [89]. Their contribution to the refractive index varies, particularly as a function of repetition rate [90]. Depolymerization has been observed in PMMA; when intense laser pulses are focused inside bulk PMMA they cause photoionization and breaks in the PMMA chains. Later, these detached PMMA chains tend to cross-link with each other, which leads to permanent chemical re-organization. The cross-linking increases the density, which in turn increases the refractive index within the interaction region inside PMMA [91].

Chapter 3

Experimental Set Up and Procedure

This chapter includes the details of the experimental set up consisting of femtosecond laser and machining systems, the experimental methods used in sample preparation and analysis and theoretical models.

3.1 Short Description of Femtosecond Laser System

This work reports all experiments that were performed with a commercial amplified Ti:sapphire laser system. The laser system includes a femtosecond oscillator, a regenerative amplifier and an optical parametric amplifier pumped by another femtosecond amplifier.

The light source used in this dielectric study is a Kerr lens mode-locked Ti:sapphire oscillator (Tsunami, Spectra-Physics) capable of producing pulses of less than 30 fs with a maximum pulse energy of 8 nJ at a central wavelength of 800 nm and repetition rate of 76 MHz. The oscillator is pumped by a 5 W Nd:YVO_4 diode solid-state laser (Millenia, Spectra-Physics, 532 nm). The pulses from the femtosecond oscillator are then sent into the regenerative amplifier (Spitfirepro, Spectra-Physics) for energy amplification. The regenerative amplifier is composed of a special cavity design enabling the passage of a single seed pulse, from the oscillator, to pass through the Pockels cell and into the cavity. At the entrance of the amplifier, the pulse is first temporally stretched in order to prevent the catastrophic self-focusing of the light onto the Ti:sapphire crystal. The pulse is amplified and recompressed by a grating compressor. The output power of the amplifier is 2.5 W and produces pulses of 46 fs in duration at a repetition rate of 5 kHz. The amplifier is pumped by a 30 W frequency-doubled Nd:YLF (Empower,

Spectra-physics, 527 nm) laser.

3.2 Laser Ablation/Modification Set Up

The beam delivery schematic and the ablation/modification setup is shown in the Fig. 3.1. The dielectric setup is mounted on an optical breadboard in an upright position and bolted to the optical table. A small percentage of the beam from the output of the laser is reflected by a beam sampler (BSF10-B1, Thorlabs, 650-1050 nm) and directed into an autocorrolator for monitoring the pulse duration. The laser beam is directed into the dielectric setup by three dielectric mirrors (Ml-M3) and passes through a gradient neutral density filter (Thorlabs, NDC-100C-4M) to control the power delivered to the focal plane. For further attenuation of the power, an additional range of neutral density filters were used.

A series of mirrors (silver coated, PF10-03-P01, Thorlabs) directed the laser beam into the back aperture of the microscope objective (10x with 0.25 NA, f = 16.5 mm, Newport). The back aperture of the microscope objective (8mm) was slightly overfilled to minimize alignment errors. The light travelling through the microscope objective is focused onto the sample. A glass slide is placed at 45° before the BA (setup1), to reflect back a small percentage of the incident light to monitor power using a fast photodiode (PDA100A, Thorlabs, 400-1100 nm). A series of ND filters, placed in front of the photodiode, ensures a linear response.

A small percentage of the light is reflected from the sample surface in the backward direction and travels through the microscope objective and exits the BA where it is reflected by the glass plate at 45° and focused (Thorlabs, f = 100 mm, plano-convex lens) onto a CCD camera (MCE-B013-US, Mightex) in order to accurately determine the position of the laser focus relative to the sample's surface. The pulse energy used for determining the sample surface is very low compared to damage threshold of the material. For a parallel beam, this arrangement gives a pair of spots with smallest features. The reason for observing 2 spots on the CCD camera is that, each focused spot on the sample surface (top or bottom) is reflected back from both top and bottom surface of the glass plate at 45° and focused on the CCD camera, resulting in 2 spots. When the microscope objective perfectly collimates the reflected light from the surface, focused by the lens, the spot size will be the smallest. With the light reflected above or below the surface, the spot size varies drastically. As a result, the light reflected above or below the surface will not be properly collimated at the back aperture of the objective with the light coming

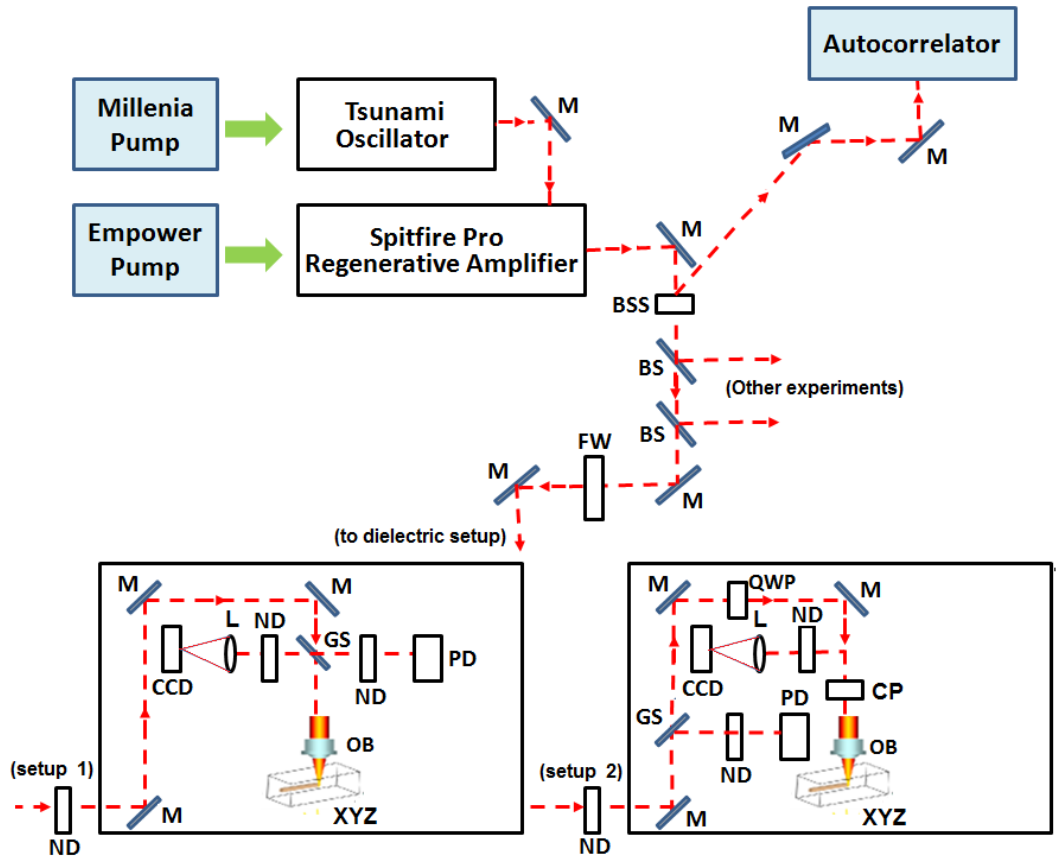

Figure 3.1: In the dielectric ablation/modification setup, the optical elements placed in the beam path on top of optics table. Plane mirrors (M, r = 97.5%), beam sampler (BSS),beam splitters (BS), filter wheel (FW), neutral density filters (ND), glass slide (GS), fast photodiode (PD), plano-convex lens (L) with f = 100 mm, a CCD camera (CCD) and a microscope objective (OB). In setup two, a quarter-wave plate (QWP) and a cube beam polarizer (CP) are added to control the power.

out either convergent or divergent when focused by the lens and the dots appear on the CCD camera becomes larger. To avoid any distortion of the incident polarization, the glass plate at 45° used for directing the back reflected light, was removed after locating the surface of PMMA.

The above setup in Figure(3.1) was used to carry out most of the ablation/internal modification experiments presented in this thesis. But some experiments required a modified setup. For example, when the light polarization required to be changed or, the electric field of the linearly polarized light needed to be reduced (setup 2). In order to change the polarization (or, the electric field) of the light delivered to the focal plane, a quarter-wave plate (WPQ05M-780, 780 nm, Thorlabs) and a cube polarizer (CM1-PBS252, 620-1000 nm, Thorlabs) were introduced in the beam path, as depicted in Figure (3.1). A quarter waveplate was used to produce elliptical or, circular polarizations. To select s or p polarizations, a polarizer was placed after the quarter waveplate. Switching the relative position of the two optics ensured that the pulse duration remained the same while changing the polarization.

In most of the work reported in this thesis, the sample was mounted on three-axis translation stages (UTM 150PE.l, Newport) with a resolution of 50 nm along the lateral dimensions (X, Y) and 100 nm along the axial direction (Z). The stages were controlled by XPS-C8 controller (Newport) via LabVIEW interface. The timing, synchronization and data acquisition were performed by a computer through general purpose data acquisition card (USB-6251, National Instrument). The control software was custom written in LabVIEW to allow full automation of most of the experiments. The laser system and the micro-machining setup are located on separate optical tables. Since distance between the lasers and the micro-machining set up is relatively large, care was taken to minimize all sources of mechanical or, environmental instabilities.

3.3 Characterization of the Laser Beam

It is absolutely crucial to control and optimize different parameters to perform the ablation and modification (micro-machining) experiments of different materials presented in this thesis. Laser processing of materials requires precise knowledge of laser spot size, fluence, pulse duration and beam profile which will be discussed in the following subsections.

3.3.1 Spot Size Determination

The minimum diameter of a focused laser beam, and hence the maximum fluence, occurs at the focus waist. For the laser beam, assuming no aberrations, the diffraction-limited minimum focus spot size may be estimated by [92],

$$D(x,y) = \frac{1.22\lambda}{NA} \tag{3.1}$$

where NA is the numerical aperture of the objective and λ is the wavelength of the laser radiation. For the laser beam and focusing optics used in this work, with a central wavelength of 800 nm and with the use of a 10x objective with a NA of 0.25, the calculated minimum focus spot diameter is 3.904 μm.

However, it is more precise to estimate the focus spot diameter from the experimental data when performing experiments to measure the material ablation threshold. To characterize the ablation/ internal modification process, determining the laser fluence is crucial. The peak fluence of a Gaussian beam is given by

$$\phi_0 = \frac{2E_0}{\pi\omega_0^2} \tag{3.2}$$

where E_0 is the pulse energy and ω_0 is the spot size, i.e., beam radius measured at $1/e^2$ of the intensity profile. The accuracy of fluence determination largely depends on the measurements of the spot size on the sample surface. One way for direct measurement of the spot size is with a CCD beam profiler. But for tightly focused beam this method is not applicable since it is limited to relatively large beams and the typical CCD pixel size is in the range of 20μm .

Another technique to measure the spot size of a tightly focused laser beam is by knife-edge technique. In this technique a knife-edge is scanned through the focus of the beam. Then the total transmitted signal is measured as a function of the lateral coordinate of the knife-edge [93, 94, 95]. However, to ensure good result the plane of the knife-edge scan has to coincide with the sample surface. The principle of this technique is to let a knife blade initially block the beam, and then move the knife with constant velocity to unblock the beam. The optical power that slips past the knife blade is measured by a detector connected to an oscilloscope. As the knife blade is completely removed from the beam path, the detected signal will rise and the rise time will be an indirect measure of spot size ω. If we assume the knife blade moves in the x-direction and has position x_0, then the fraction of the optical power that slips past and hits the detector is given by equation 3.3,

$$R = \frac{P_{detector}}{P} = \int_{x=x_0}^{\infty} \int_{-\infty}^{\infty} \frac{2}{\pi\omega^2} e^{\frac{-2(x^2+y^2)}{\omega^2}} dydx \tag{3.3}$$

There is another method [96] for measuring spot size of a tightly focused beam through the dimensions of the ablation crater. This technique also aids to determine the threshold for ablation/modification of the sample. When short pulses of light interacts at a sample surface, it may result in ablation when the laser fluence, ϕ_0, exceeds a certain fluence threshold, ϕ_{th}. The ablation will occur with the ejection of material from the surface [97, 98]. The ϕ_{th} value is characteristic to the material and on the number of laser shots delivered to the region. The diameter (D) of the modified region, assuming a Gaussian profile of the laser beam is related to the energy of the incident pulse by the following equation [99, 97]),

$$D^2 = 2\omega_0^2 ln\frac{\phi_0}{\phi_{th}} \tag{3.4}$$

where D^2 is the squared diameter of the modified region.

Experimentally to find out the true spot size at the target surface, single pulse ablation spots were produced by scanning the focus spot at a certain separation over the flat surface. Pulse energy was varied over a range of values while the focus spot radius was maintained at a known, fixed value. Since there is a linear relationship between E_{pulse} and ϕ_0, a semi-logarithmic plot of D^2 versus $ln(E_{pulse})$ was plotted. The approximate $1/e^2$ radius value for a Gaussian beam (ω_0) of the laser focus spot needed for subsequent calculations, and can be computed from the slope m of a semi-logarithmic plot of D^2 vs. laser pulse energy (provided that, a linear fit was extrapolated from the graph) by the following relationship [97, 98],

$$\omega_0 = \sqrt{\frac{m}{2}} \tag{3.5}$$

Damage threshold fluence ϕ_d is the minimum fluence at which any visible damage (but not removal) of the target surface appears. As long as the experimental damage diameters can be measured within the range $\phi_d < \phi_0 < \phi_{th}$, ϕ_d can be found by a similar procedure as for ϕ_{th}.

To determine the spot size at the target surface, the dimensions of all the ablation holes were measured with the aid of software **imageJ** in the SEM images for both 2-shots and 5-shots experiments. From these measurements, D^2 versus $ln(E_{pulse})$ graphs were plotted for both the 2-shots and the 5-shots measurements. The spot size for 1-shot was not plotted due to the fact that, for higher fluence the shape of the ablation crater becomes elongated along the direction of polarization for linearly and elliptically

polarized light. Therefore, there were less data points available for the graph. As seen

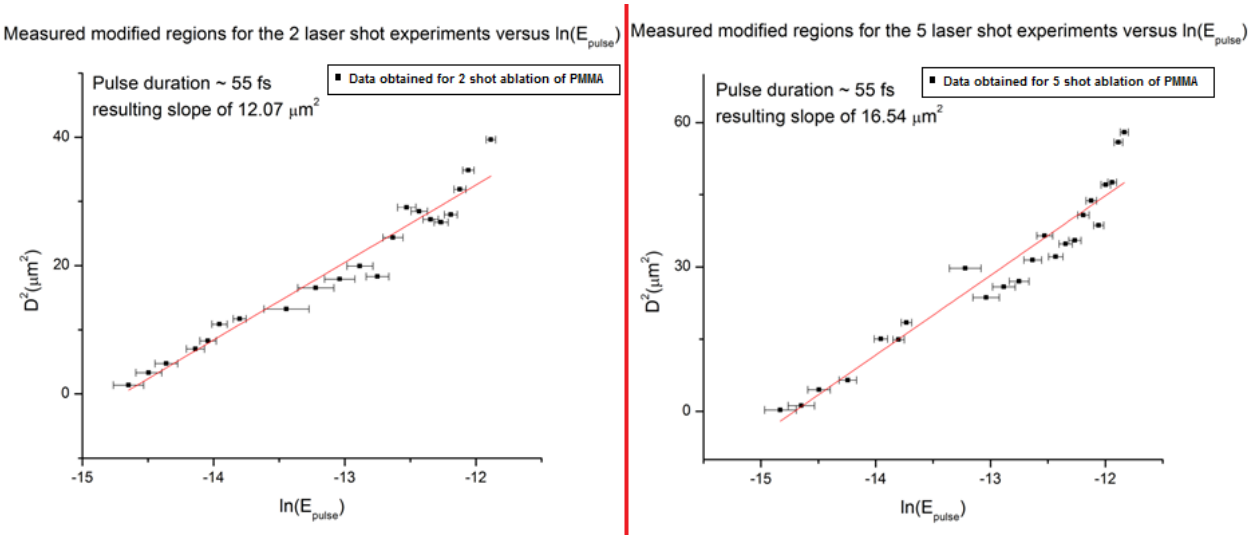

Figure 3.2: Graphs of D^2 versus $ln(E_{pulse})$; (left) for 2-shots and (right) 5-shots. From the slope, the beam radius is obtained: 2.46 μm from the 2-shots and 2.87 μm from the 5-shots graph.

from the graphs in Figure (3.2), the slope of 2-shots graph and 5-shots graph is slightly different; the beam radius is close to 2.46 μm and 2.87 μm respectively. An average was taken to provide an estimated beam radius of 2.67 μm. Therefore, the estimated spot size is 5.34 μm for the light focused at the surface of the PMMA sample. As the size of the ablation crater is dependent on laser fluence, the measurement of the spot size from the dimension of the crater will vary accordingly. The spot size was also obtained from knife-edge measurement for continuous pulses, and the beam radius is 1.64 μm, comparable to the value obtained from D^2 versus $ln(E_{pulse})$ graphs for 2 shots and 5 shots. But the magnification of the microscope objective used for the knife-edge measurement was 16x (NA 0.25) as opposed to the 10x (NA 0.25) objective used for the other method.

It is evident from here that the experimental results of D^2 are nearly twice the value of theoretically achieved value of the limit of diffraction. The theoretical estimation is very much dependent on the beam and objective quality and is provided assuming an ideal illumination. If a Gaussian beam two times larger than the aperture diameter of the objective, there are around 60% of losses. But for efficient machining of materials, it is necessary to have enough energy. To deal with this issue, the objective aperture should be illuminated with a beam comparable or, quite smaller than the aperture. In

our experiment, we slightly overfill the back aperture of the objective to avoid alignment error, giving the beam a flat top-like profile.

3.3.2 Average Power Measurement

For most of the experiments presented in this thesis, it is crucial to determine the threshold fluence/energy density for ablation/modification/damage. Also the analysis of the dependence of different machining parameters on pulse energy reveals important insights on laser-solid interaction. All these characterization requires precise measurements of power.

The power measurements at the wavelength of 800 nm were performed with a continuous wave power meter (407 A, Spectra-Physics), capable of measuring within the power range from a few mW upto 20W. The accuracies of the power meter was quoted in between 1% to 3% respectively in the wavelength ranges of interest. The power meter used to measure the average power and have a response time of $\sim$0.5 second and, hence, cannot directly measure the energy of individual pulses. The pulse energy can be calculated by dividing the average power measured by the repetition rate of the laser (5 kHz).

Initially, with the power meter, the available power was measured at different locations of the set up to find out losses from various optics within the set up. In all the experiments presented in this thesis, the incident pulse energies were measured after the microscope objective, taking into account the transmission and reflection losses of all the optics. To account for the power fluctuations or drifts, a fast photodiode (PDA100A, Thorlabs, 400-1100 nm) was used for calibration of power. The photodiode is calibrated by associating the voltage of the photodiode with the average laser power measured by the power meter. A series of ND filters was placed in front of the photodiode to ensure a linear response. To confirm the accuracy of the neutral density filters provided by the manufacturer, several measurements were taken in the lab. The photodiode is calibrated at the start of each experiment to obtain a linear relation between power and voltage that will be used throughout the experiments to determine the energy delivered to the focal plane.

3.3.3 Determination of Fluence and Focus Properties

To determine the laser fluence with great accuracy is vital for analysis of ablation/modification process. The minimum diameter of a focused laser beam and the maximum fluence oc-

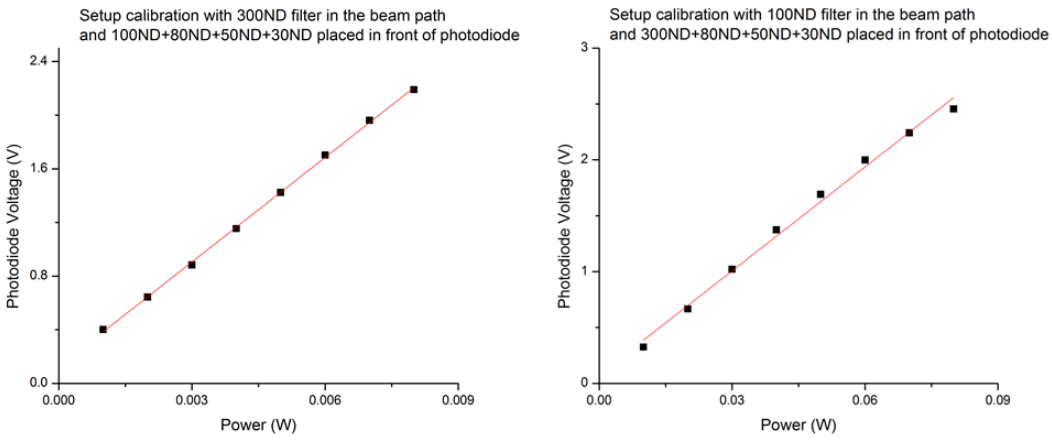

Figure 3.3: Calibration graphs of the photodiode using different combination of the ND filters in the beam path and in front of the photodiode. Both calibrations were taken with the same gain of 10 dB. Multiple points were taken to extrapolate linear relation and verify the linear response of the photodiode. The R^2 value of each graph are nearly 1; indicating a good linear response and accuracy of the measurements.

curs at the focus waist which has a Gaussian shaped intensity profile. The fluence is defined as a quantity of energy per pulse applied on all the surface of the beam (J/cm^2) such as,

$$F = \frac{E}{A} = \frac{P_{ave}}{fA} \tag{3.6}$$

where E is the energy per pulse (J), A the surface area of the beam(cm^2), P_{ave} is the average laser output power (W) of the beam and f is the repetition rate (Hz) of the amplifier. P_{ave} is measured by the power meter and can be given by the expression $P_{ave} = Ef$, as a function of laser source characteristics. Now it is now possible to calculate the value of the fluence with the value of the size of the beam by equation 3.6.

It is vital to find out laser peak power P_{peak} to calculate peak intensity at the focal spot during ablation or, modification of the target material. Peak intensity delivered to the focal plane determines the dominant regimes of the photoionization that occurs during the ablation/modification process.

To calculate peak intensity, we have to calculate peak power at first. The laser peak power P_{peak} is related to average laser power P_{ave} by the following expression,

$$P_{peak} = \frac{E}{\tau} = \frac{P_{ave}}{f\tau} \tag{3.7}$$

where τ is the pulse duration. In terms of fluence, this expression will be

$$P_{peak} = \frac{FA}{\tau} \tag{3.8}$$

Intensity of the focal spot is can be given in terms of laser peak power, which in turn can be correlated to laser fluence as,

$$I = \frac{P_{peak}}{A} = \frac{F}{\tau} \tag{3.9}$$

As mentioned in previous section, the spot size is calculated to be 3.904 μm, assuming no aberrations and the objective's spot size is diffraction limited.

Since the process of photoionization depends on the intensity delivered to the focal plane. In this work, for the energy range of 1 nJ to 10 μJ used in different experiment and pulse duration of 70 fs at the back aperture of the microscope objective, the approximate value for the intensity is $\approx 10^{14}$ W/cm^2.

As discussed in Chapter 2, with intensity nearly 10^{14} W/cm^2, multiphoton ionization is the only possible dominant mechanism (MPI depends on the bandgap of the material as well), more than a factor of 5 higher than avalanche ionization. At high intensities multiphoton ionization (MPI) dominates avalanche because MPI scales nonlinearly with intensity while avalanche ionization scales linearly [100].

The intensity mentioned above is a rough estimate as the pulses are bandwidth limited at the entrance of the lens where the duration is measured to be 70 fs. The pulse duration was not measured after the objective. Throughout the experiments, an aspheric microscope objective was used. As a result, the pulse duration is expected to be no more than 80-90 fs, resulting in an uncertainty in the laser intensity by about 15-20%. Also, the spot size plays a significant role for uncertainty in the intensity calculation since experimentally measured spot size was found to be slightly larger than that of the diffraction limited spot size. However, these should not affect the fluence. In fact, the single shot ablation threshold (experimental results from Chapter 4) agrees well with the published data.

3.3.4 Confocal Parameter

Confocal parameter, b, is another variable that can affect the modified region during the ablation process, which can be expressed by the following expression

$$b = 2.74 \frac{n\lambda}{NA^2} \tag{3.10}$$

where n is the refractive index of the medium, λ is the central wavelength of the laser and NA is the numerical aperture of the objective.

The ablation/modification process significantly depends on the extent of the length of the confocal parameter [51, 101]. The value of the confocal parameter gives the scope of error where the surface of the sample must be located during the ablation experiment in order to have precise data. If the sample surface is outside the range of the confocal parameter, it would affect the measurement of threshold energies. Since threshold energy/fluence is correlated with intensity, photoionization rate would vary considerably due to its n-th order dependence on intensity. Therefore, for precise measurements of the threshold values, all the samples should be located within that range of the confocal parameter.

For the work presented in this thesis, the confocal parameter is $\approx$35 μm (equation3.10) considering a 10x objective with a NA of 0.25 and taking $n = 1$ (air) for a laser with a central wavelength of 800 nm.

3.3.5 Pulse Width Measurement

The pulse width measurement and characterization of ultrashort laser pulses is critical. There are different autocorrelation techniques, for example frequency-resolved optical gating (FROG) and grating-eliminated no-nonsense observation of ultrafast incident laser light e-fields (GRENOUILLE) [101, 102]. The complexity stems from stretching the femtosecond laser pulses as they pass through an optical microscope for laser modification/ablation. Even a few tens of femtosecond increment in the pulse duration can give rise to a rapid decrease in intensity measurement (as discussed in the previous section). For femtosecond laser source with a very low average power, this reduced intensity issue becomes more challenging since transient TW/cm^2 laser intensities are needed to induce multiphoton ionization.

In experiments presented in this thesis, the pulse duration of the laser at the entrance of the dielectric setup has been measured by a single shot autocorrelator. This autocorrelator is sensitive within the range of 30-150 fs. Experimental autocorrelation profiles measured at the laser output and after the objective are given in the Fig. 3.4. The basis of a single shot autocorrelator relies on the splitting of the output beam into two separate beams which are focused into a nonlinear medium (BBO crystal) after a time delay. A second harmonic (SH) signal is generated in the forward direction because of momentum conservation resulting from the non-collinearly frequency-doubling in the

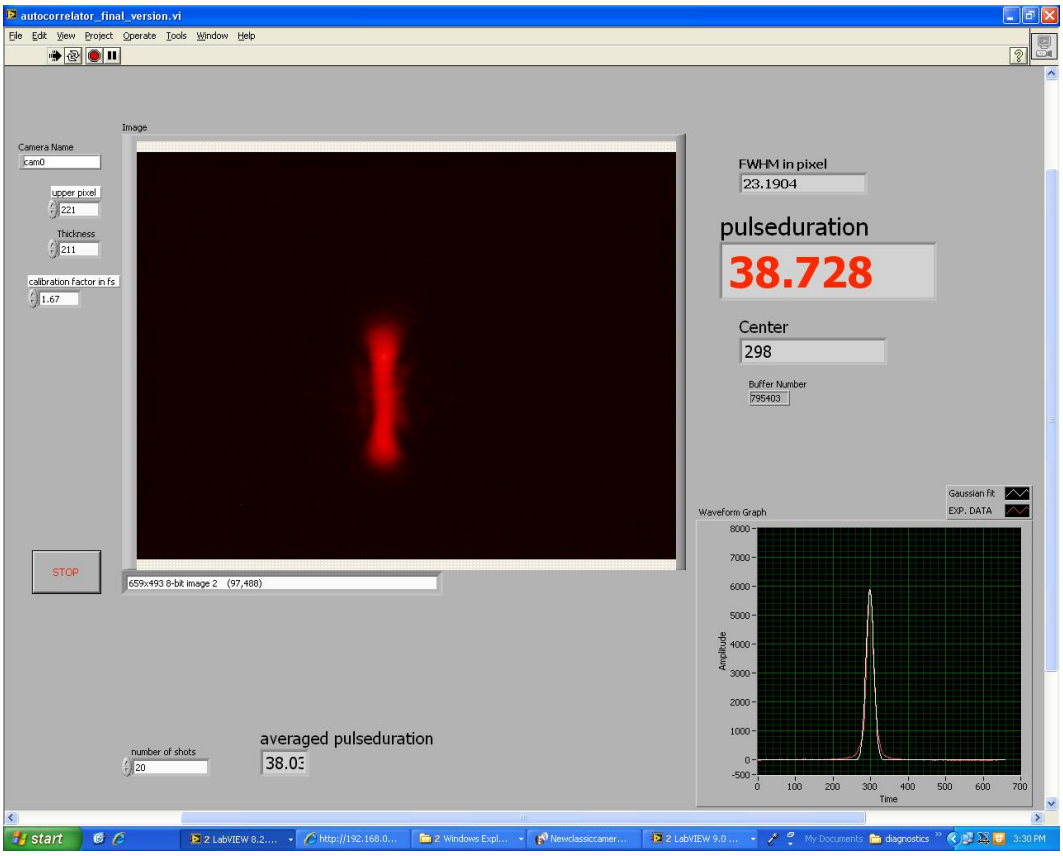

Figure 3.4: Experimental autocorrelator profile of the pulse at the output laser, after a small percentage of the beam from the output of the laser is reflected by a beam sampler and directed into the autocorrolator for measuring the pulse duration.

BBO crystal. The intensity of the SH signal changes depending on the variation of the time delay between the pulses. Signal is maximum when there is a temporal overlap and in opposite cases drops off gradually. In the femtosecond configuration the relative wavefront tilt produces a spatial time delay in the frequency-doubled signal, which results in an autocorrelation of the temporal intensity profile. On the basis of intensity autocorrelation, an autocorrelation in time is being transformed into a spatial intensity distribution. Therefore, the SH signal intensity A can be expressed by the following expression

$$A(\tau) = \int_{-\infty}^{\infty} I_s(t) I_r(t-\tau) dt \tag{3.11}$$

where I_s is the intensity of one of the beams, and $I_r(t-\tau)$ is the intensity of the delayed pulse.

A CCD camera is used to image the SH signal and spatial intensity distribution to convert the resultant signal into an autocorrelation trace of the pulse. Thus the detected autocorrelation signal is available for display as a measurement by a computer. The pulse duration measurement of the Gaussian shape beam profile is achieved by using the following expression,

$$\tau = \frac{\Delta\omega sin(\theta)}{\sqrt{2c}} \tag{3.12}$$

where $\Delta\omega$ is the vertical width of the trace, τ is the pulse duration, and θ is the intersecting angle between the two beams. Using the above equation, the pulse duration from the regenerative amplifier was found to be 46 fs. A small percentage of the beam from the output of the laser is reflected by a beam sampler (BSF10-B1, Thorlabs, 650-1050 nm) and directed into an autocorrelator for measuring the pulse duration.

For ablation/modification studies, it is crucial to evaluate the pulse duration delivered to the focal plane to calculate intensity, or fluence, which helps to understand the femtosecond laser ablation/modification dynamics. The first step is to take into account all the optics in the beam path through which the pulse propagates before entering the back aperture of the objective and place them (except for beam splitter) in the beam path of the autocorrelator to recreate the original experimental condition. Under that circumstances, the pulse duration at the back aperture is measured to be 52 fs.

To take into account the pulse broadening through the two beam splitters (BK7) within the beam path, Sellmeier's equation was used to determine the dispersive effect [101]. The group velocity dispersion (GVD) of BK7 was calculated to be of 50.6 fs^2/mm provided that the refractive index of BK7 is 1.51 for the central wavelength of 800 nm. The pulse duration along with all the optics including two beam splitters was calculated

using the dispersive pulse broadening equation [103, 101].

$$\tau = \tau_0 \sqrt{1 + (\frac{GDD}{\tau_0^2} 4ln2)^2} \tag{3.13}$$

where τ_0 is the pulse duration before entering the dispersive medium. The beamsplitters gives rise to a total group delay dispersion (GDD) of 303.6 fs^2 considering to have a collective thickness of 6 mm. Using the above expression the pulse duration is found to be 55 fs at the back aperture of the objective.

To change the laser polarization, a quarter-wave plate or a half-wave plate was introduced in the beam path along with a cube polarizer. This resulted in further broadening of the pulse which was finally calculated to have a duration of 72 fs at the back aperture of the objective.

Throughout the experiments, an aspheric objective was used instead of a standard microscope objective (that typically have 5-7 optical elements of different materials) to minimize dispersion. As a result, the pulse duration is expected to be no more than 80-90 fs.

3.4 Characterization Methods

The laser-ablated morphology of femtosecond laser induced breakdown was studied with scanning electron microscopy (SEM), atomic force microscopy (AFM), and optical microscopy (OM). In most cases for preliminary characterization images were taken by OM such as, for characterization of surface morphology (qualitative investigation) and for etch length/diameter measurement (quantitative investigation). For more precise analysis, SEM was used. For example, to find out the lowest energy at which ablation/permanent index modification features that were visible under the scanning electron microscope (SEM) gives the accurate threshold value. Quantitative analysis such as the dimension of the modified region as small as nanometer resolution was very accurately measured by SEM. AFM was used for quantitative analysis of the laser-ablated regions such as the height and depth of the ablated region.

3.4.1 Scanning Electron Microscopy

The laser-ablated regions were characterized by scanning electron microscope (SEM) using lab facilities in both Dr. Arnaud Weck's lab in Mechanical Engineering department

and Centre for Catalysis Research and Innovation (CCRI) (JSM-7500F FESEM (JOEL)) at University of Ottawa. To assist imaging, all samples such as PMMA and fiber surface required gold coating with a thin layer (few nanometers) to make them conductive. Special care was taken to maintain steady electron beam conditions such as beam spot size and accelerating voltage during SEM image collection so that proper comparisons could be made between samples. All SEM images were taken with the electron beam perpendicular to the sample (zero tilt).

3.4.2 Atomic Force Microscopy

Laser induced surface topology was investigated at Pelling Lab, University of Ottawa by an AFM (Nanowizard II, JPK Instruments, Germany) to characterize the ablation morphology including the ablation depth and protrusion height as a function of laser pulse energy. Contact mode was employed, where 10 μm x 10 μm of images were initially obtained and then zoomed relatively to 5 μm$\times$5 μm. This particular AFM used a pyramidal PNP-TR-50 cantilever (Nanoworld) having a half-cone angle of 35°, tip height of 3.5 μm and a spring constant of 691 pN/nm tracing the sample with $< 10nN$ in radius of curvature. Images were captured with a relative tip speed of 1 μm/sec. The typical lateral and vertical resolutions were 30 nm and 0.1 nm, respectively.

3.4.3 Optical Microscope

An optical microscope was used for detecting and imaging fs laser induced permanent internal modification and ablation for multiple purposes, such as for measuring damage and ablation threshold, etch depth/diameter and ablation morphology studies of different samples including PMMA, cubed fused silica and fiber samples. Optical microscope images were taken at the Ultrafast Photonics Lab, University of Ottawa using Olympus BX51 microscopes of different magnification (20x, 40x, 60x, 100x) with a CCD camera (Thorlabs-DC210).

3.5 Theoretical Models for Numerical Simulations

High precision material processing resulting from femtosecond laser pulse interaction with solids is greatly dependent on optimization of experimental parameters, as mentioned in last few sections of this chapter. Understanding the fundamental mechanism and correlation between the subsequent processes during the ultrashort laser-material interaction

aids to choose the optimal laser and target parameter. These parameters facilitate to achieve simple scaling relations to predict the ablation/modification condition for any target material, which directly influence the progress of the cutting edge ultrashort laser technologies and its applications.

That is why besides experimental studies, femtosecond laser-material interaction have been studied through analytical and numerical approach. At present, different successful models have been applied by various groups to unravel distinct mechanisms and dynamics involving femtosecond laser ablation/modification phenomena.

The underlying mechanisms of laser-solid interaction in femtosecond timescale gives rise to various physical processes, such as, excitation of free carriers, thermalization of the deposited laser energy, formation of a highly energetic high-temperature and high-pressure region, explosive disintegration and prompt forward ejection of a volume of material, intensive processes in the ejected plume, recondensation or deposition of the ejected particles in pulsed laser deposition, and propagation of a pressure wave into the bulk of the target away from the ablation region [79]. To take into account the complex nature of all these subsequent processes with appropriate resolution is numerically daunting for any single model. Therefore, scientists around the world tend to combine and extend different theoretical and computational approaches.

Based on the work presented in this thesis, a Molecular Dynamics (MD) in 2D approach is used for understanding the general mechanics of thermal processes leading to formation of the dome-like structures, features of ablation craters and nano-pillar like structure on bulk sample surface. For single shot experiments, polarization dependence of the ablation features was numerically simulated by finite difference time domain (FDTD) method and explained the underlying physics. Application of both MD and FDTD methods for the respective experiments agrees well with the experimental data presented in this thesis.

3.5.1 Molecular Dynamics Simulation

The reason for choosing a molecular dynamics (MD) approach over other numerical processes is that it describes the evolution of the irradiated material from the energy deposition to the final state of the material and is naturally capable of describing the non-equilibrium phase transition processes at the atomic level. In other words, it is able to provide a complete microscopic description of the dynamical processes involved in laser ablation. Other models are typically used to describe thermal processes in bulk samples

and shown to encounter serious challenges when extended to ultrafast laser ablation [104], due to fundamental difficulties in describing highly non-equilibrium phase transition processes along with the necessity to resolve microscopic processes. Hydrodynamic models are the example.

MD models can be explained as a n-number of spheres, interacting in a 2 or 3 dimensional lattice with translational and internal degrees of freedom. All atoms interact with each other via a predefined potential function. At every time step the positions, velocities and forces of all atoms are tracked. Afterwards the motions of the interacting atoms are used to evaluate macroscopic parameters such as temperature, pressure and density from statistical data processing [105]. In this thesis, the experimental results show adequate agreement with the predictions achieved from MD simulation. For example, formation of the dome-like structures by single pulse ablation, creation of nano-pillar structure within the ablation crater by two-pulse ablation, and the evolution of the ablation crater on the bulk PMMA surface. The details of the treatment of the MD model appropriate for the surface ablation of PMMA is described in chapter 4.

Unfortunately, MD method has severe limitations in computing the laser ablation on time and length scales such as small cell sizes and full microscopic description of the ablation process. Some specific features of laser ablation are not possible to address with present computation capabilities (e.g., long-term expansion of the ablation plume). Recent advances in computer technology and possibilities for integration of the MD method into a multiscale computational model is soon going to address the underlying physical and chemical processes involved in the laser ablation phenomena.

3.5.2 Finite Difference Time Domain Simulation

Finite difference time domain (FDTD) is a well known numerical analysis method for modelling computational electrodynamics [106, 107]. This method finds approximate solutions to the associated system of differential equations. FDTD is able to cover a wide frequency range with a single simulation run as it is a time domain method which can take into account the nonlinear properties of material. The finite difference time domain method is based on partial differential equations and direct approximation of the differential operators in the Maxwell curl equations, on a grid staggered in time and space. The time dependent Maxwells equations are discretized using central difference approximations to the space and time partial derivatives. This permits a scheme which uses first-order numerical differentiation to provide second-order accuracy. The resulting

finite difference equations are solved in either software or hardware repeatedly until the desired transient or steady-state electromagnetic field behaviour is fully evolved. A detailed description of FDTD simulation tools is given in [106, 107].

In polarization dependent femtosecond laser ablation studies, FDTD code solves the 3D Maxwell equations in a non-magnetic material [108]. Using this method would possibly explain the resulting ablation/modification phenomena by determining energy deposition patterns and assuming that all of the absorbed energy is eventually transferred to the lattice and show that the elongation of ablation craters arises from the local field enhancement during light-plasma interaction.

However, few approximations are made during computation of this FDTD code, such as the effect of avalanche ionization; higher order nonlinearities incase of intense laser interactions are neglected. Therefore, the results from numerical simulations presented in the polarization dependent study of fs laser ablation Chapter 4 only offer qualitative agreement with the experiments.

Chapter 4

Surface Swelling and Polarization Dependence

4.1 Introduction

This chapter is based on two previously published papers, and both manuscripts are accepted for publication. The papers describe the experimental and theoretical results of single pulse ablation of PMMA to gain insights into the fundamental aspects of ablation process. In section 4.2 we investigate whether single pulse ablation in PMMA results in direct material removal (ablation), or surface swelling followed by material removal. We studied single pulse ablation of PMMA as a function of pulse energy. Prior to this investigation, the detailed analysis of the onset of surface ablation and the evolution of the ablation craters with fluence, including comparison between experimental results and numerical simulations were missing. For the first time, we demonstrated that the onset of single pulse ablation on bulk dielectric surface is accompanied by surface swelling. We identified 2 regimes corresponding to the dominance of swelling or ablation. For pulse energies upto 1.5x damage threshold, swelling dominates. Ablation dominates for energy greater than 1.5x damage threshold. To study evolution of swelling and ablation, we used a 2 dimensional (2D) Molecular Dynamics (MD) model to predict ablation characteristics. This model (MD) provided physical insight into swelling dynamics by showing that void formation and material swelling are important mechanisms for temperature equilibration at the surface of the laser-heated sample.

In section 4.3 we studied the role of polarization for single pulse ablation in dielectrics. We found when the laser fluence was increased beyond twice the damage threshold, the

shape of the ablation craters became polarization dependent in the form of elongated craters for linear and elliptical polarization. The polarization dependence was preserved for line ablation within the quasi-periodic structures inside the ablated region. The impact of polarization-dependent ablation can be minimized by using either pulse energies close to ablation threshold, or circularly polarized light. Using optical and scanning electron microscope, we examined the morphology of the material changes induced by tightly-focused femtosecond laser pulses in bulk transparent materials, and identified several mechanisms by which material alterations are produced. Besides, 3 dimensional (3D) Finite Difference Time Domain (FDTD) simulations were performed to predict and understand the polarization dependence of the fs laser-polymer interaction. The simulations revealed that elongation of ablation crater arises from the local field enhancement during light-plasma interaction. The results from numerical simulations agreed well with the experimental results presented in this thesis. The overall results suggest there is a narrow range of fluences that produce clear holes and cuts in dielectrics.

4.2 Femtosecond laser induced surface swelling in poly-methyl methacrylate (Publication 1)

F. Baset, K. Popov, A. B. Villafranca, J-M Guay, Z. Al-Rekabi, A. E. Pelling, L. Ramunno and V. R. Bhardwaj
Femtosecond laser induced surface swelling in poly-methyl methacrylate
Optics Express **21**, 12527 (2013)

4.2.1 Author contribution

The published results come from experiments performed by F. Baset, A. B. Villafranca, J-M Guay and V. R. Bhardwaj at Ultrafast Photonics lab, University of Ottawa, ON. F. Baset and J-M Guay performed preliminary (unpublished data) and final experiments under supervision of V. R. Bhardwaj. F. Baset and A. B. Villafranca conducted the analysis of the results and F. Baset created the figures. AFM was conducted under supervision of Z. Al-Rekabi. Theoretical simulation had been performed by K. Popov and L. Ramunno. F. Baset wrote the first draft of the manuscript. All authors contributed to the final manuscript.

Femtosecond laser induced surface swelling in poly-methyl methacrylate

Farhana Baset, Konstantin Popov, Ana Villafranca, Jean-Michel Guay, Zeinab Al-Rekabi, Andrew E. Pelling, Lora Ramunno and Ravi Bhardwaj*

Department of Physics, University of Ottawa, 150 Louis Pasteur, Ottawa, ON, K1N 6N5, Canada

[redacted]i@uottawa.ca

Abstract: We show that surface swelling is the first step in the interaction of a single femtosecond laser pulse with PMMA. This is followed by perforation of the swollen structure and material ejection. The size of the swelling and the perforated hole increases with pulse energy. After certain energy the swelling disappears and the interaction is dominated by the ablated hole. This behaviour is independent of laser polarization. The threshold energy at which the hole size coincides with size of swelling is 1.5 times that of the threshold for surface swelling. 2D molecular dynamics simulations show surface swelling at low pulse energies along with void formation below the surface within the interaction region. Simulations show that at higher energies, the voids coalesce and grow, and the interaction is dominated by material ejection.

OCIS codes: (140.3390) Laser material processing; (220.4241) Nanostructure fabrication; (320.2250) Femtosecond phenomena.

References and links

1. C. D. Marco, S. M. Eaton, R. Suriano, S. Turri, M. Levi, R. Ramponi, G. Cerullo, and R. Osellame, "Surface properties of femtosecond laser ablated PMMA," Appl. Mater. Interfaces **8**, 2377–2384 (2010)
2. E. Yap, D. G. McCulloch, D. R. McKenzie, M. V. Swain, L. S. Wielunski, and R. A. Clissold, "Modification of the mechanicaland optical properties of polycarbonate by 50-keV Ar^+ and H^+ ion implantation," J. Appl. Phys. **83**, 3404–3412 (1998)
3. S. Nolte, B. N. Chichkov, H. Welling, Y. Shani, K. Liebermann, and H. Terkel, "Nanostructuring with spatially localized femtosecond laser pulses," Opt. Lett. **24**, 914–916 (1999)
4. J. Kruger and W. Kautek, "The femtosecond pulse laser: a new tool for micromaching," Laser Phys. **9**,30–40 (1999).
5. K. M. Davis, K. Miura, N. Suguimoto, and K. Hirao, "Writing waveguides in glass with a femtosecond laser," Opt. Lett. **21**, 1729 (1996)
6. E.N. Glezer, M. Milosavljevic, L. Huang, R. J. Finlay, T-H Her, J. P. Callan, and E. Mazur, "Three-dimensional optical storage inside transparent materials," Opt. Lett. **21** 2023–2025 (1996)
7. V. R. Bhardwaj, E. Simova , P. P. Rajeev, C. Hnatovsky , R. S. Taylor , D. M. Rayner, and P. B. Corkum, "Optically produced arrays of planar nanostructures inside fused silica," Phys. Rev. Lett. **96**, 057404 (2006)
8. Y. Han , X. Zhao, and S. Qu, "Polarization dependent ripples induced by femtosecond laser on dense flint (ZF6) glass," Opt. Express **19** 19150 (2011)
9. S. I. Anisimov, B. L. Kapeliovich, and T. L. Perel'man, "Electron emission from metal surfaces exposed to ultrashort laser pulses," Sov. Phys. JETP **39**, 375–377 (1974)
10. S. S. Wellershoff, J. Hohlfeld, J. Gudde, and E. Matthias, "The role of electron-phonon coupling in femtosecond laser damage of metals," Appl. Phys. A **69**, 99–107 (1999)
11. S. I. Anisimov, B. S. Luk'yanchuk, and A. Luches, "An analytical model for three-dimensional laser plume expansion into vacuum in hydrodynamic regime," Appl. Surf. Sci. **96-98** 24–32(1996)

#187454 - $15.00 USD Received 20 Mar 2013; revised 26 Apr 2013; accepted 6 May 2013; published 14 May 2013

12. M. Aden, E. Beyer, G. Herziger, and H. Kunze, "Laser-induced vaporization of a metal surface," J. Phys. D **25**, 57 (1992)
13. T. E. Itina, J. Hermann, Ph. Delaporte, and M. Sentis, "Laser generated plasma plume expansion: Combined continous-microscopic modelling," Phys. Rev. E **66**, 066406–066412 (2002)
14. P. Lorazo, L. J. Lewis and M. Meunier, "Short-Pulse Laser Ablation of Solids: From Phase Explosion to Fragmentation," Phys. Rev. Lett. **91** 225502 (2003)
15. S. I. Anisimov and B. S. Luk'yanchuk, "Selected problems of laser ablation theory," Physics - Uspekhi, **45**, 293–324 (2002)
16. F. Korte, J. Koch, and B. N. Chichkov, "Formation of microbumps and nanojets on gold targets by femtosecond laser pulses," Appl.Phys. A **79**, 879 (2004)
17. H. Tamura, T. Kohama, K. Kondo, and M. Yoshida, "Femtosecond laser induced spallation in Aliminum," J. Appl. Phys. **89**, 3520 (2001)
18. D. Bauerle, U. M. Himmelbauer, and E. Arenholz, "Pulsed laser ablation of polyimide: fundamental aspects," J. Photochem. Photobiol. A. **106**, 27–30 (1997)
19. S. Baudach, J. Bonse, J. Kruger, and W. Kautek, "Ultrashort pulse laser ablation of polycarbonate and polymethymethacrylate," Appl. Surf. Sci. **154-155**, 555-560 (2000)
20. J. Kruger, S. Martin, H. M'debach, L. Urech, T. Lippert, A. Wokaun, and W. Kautek, "Femto- and nanosecond laser treatment of doped polymethylmethacrylate," Appl. Surf. Sci. **247**, 406–411 (2005)
21. J-M Savolainen, M. S. Christensen, and P. Balling, "Material swelling as the first step in the ablation of metals by ultrashort laser pulses," Phys. Rev. B **84**, 193410 (2011)
22. B. Chimier, O. Uteza, N. Sanner, M. Sentis, T. Itina, P. Lassonde, F. Legare, F. Vidal, and J. C. Kieffer, "Damage and ablation thresholds of fused-silica in femtosecond regime, Phys. Rev. B **84**, 094104 (2011).
23. L. V. Zhigilei, E. Leveugle, B.J . Garisson, Y. G. Yingling, and M. I. Zeifman, "Computer Simulations of Laser Ablation of Molecular Substrates," Chem. Rev. **103**, 321–348 (2003)
24. B. J. Demaske, V. V. Zhakhovsky, N. A. Inogamov, and I. I. Oleynik, "Ablation and spallation of gold films irradiated by ultrashort laser pulses," Phys. Rev. B. **82**, 064113 (2010)
25. L. V. Zhigilei, Z. Lin, and D. S. Ivanov, "Atomistic modelling of short pulse laser ablation of metals: connections between melting, spallation and phase explision," J. Phys. Chem. C **113**, 11892–11906 (2009)
26. R. Herrmann, J. Gerlach, and E. Campbell, "Ultrashort pulse laser ablation of silicon: an MD simulation study," Appl. Phys. A **66**, 35–42 (1998)
27. P. Lorazoa, L. J. Lewisb, and M. Meuniera, "Picosecond pulsed laser ablation of silicon: a molecular-dynamics study," Appl. Surf. Sci. **168**, 276–279 (2000)
28. C. Cheng, A. Q. Wu, and X. Xu, "Molecular dynamics simulation of ultrashort laser ablation of fused silica," J. Phys: Conference Series **59**, 100–104 (2007)
29. C. Chen, P. Depa, J. K. Maranas, and V. G. Sakai, "Comparison of explicit atom, united atom, and coarse-grained simulations of poly(methyl methacrylate)," J. Chem. Phys. **128**, 124906 (2008)
30. B. Rethfeld, A. Kaiser, M. Vicanek, and G. Simon, "Ultrafast dynamics of nonequilibrium electrons in metals under femtosecond laser irradiation," Phys. Rev. B **65**, 214303 (2002)
31. M. Li, S. Menon, J. P. Nibarger, and G.N. Gibson, "Ultrafast Electron Dynamics in Femtosecond Optical Breakdown of Dielectrics," Phys. Rev. Lett. **82**, 2394 (1999)
32. D. S. Ivanov and L. V. Zhigilei, "Combined atomistic-continuum modeling of short-pulse laser melting and disintegration of metal films," Phys. Rev. B **68**, 064114 (2003)
33. J. Hirschfelder, C. F. Curtiss, and R. Bird, *Molecular Theory of Gases and Liquids* (Wiley, 1954 New York).
34. S. Plimpton, "Fast Parallel Algorithms for Short-Range Molecular Dynamics," J. Comp. Phys. **117**, 1 (1995)
35. E. Weinan and Li. Dong, "On the Crystallization of 2D Hexagonal Lattices," Commun. Math. Phys. **286**, 1099 (2009)
36. J-M. Guay, A. Villafranca, F. Baset K. Popov, L. Ramunno, and V. R. Bhardwaj, "Polarization dependent femtosecond laser ablation of PMMA," New. J. Phys. **14**, 085010 (2012)
37. M. E. Povarnitsyn, T. E. Itina, M. Sentis, K. V. Khishchenko, and P. R. Levashov, "Material decomposition mechnaisms in femtosecond laser irradiation with metals," Phys. Rev. B **75** 235414 (2007)
38. E. Leveugle, D. S. Ivanov, and L. V. Zhigilei, "Photomechanical spallation of molecular and metal targets: molecular dynamics study," Appl. Phys.A **79** 1643–1655 (2004)
39. D. S. Ivanov, Z. Lin, B. Rethfeld, G. M. O'Connor, T. J. Glynn, and L. V. Zhigilei, "Nanocrystalline structure of nanobump generated by localized photoexcitation of metal film," J. Appl. Phys. **107**, 013519 (2010)
40. M. B. Agarnat, S. I. Anisimov, S. I. Ashikov, V.V. Zhakhovskii, N. A. Inogamov, K. Nishihara, Yu. V. Petrov, V. E. Fortov, and V. A. Khokhlov, "Dynamics of plume and crater formation after action of femtosecond laser pulse," Appl. Surf. Sci. **253** 6276-6282 (2007)

#187454 - $15.00 USD Received 20 Mar 2013; revised 26 Apr 2013; accepted 6 May 2013; published 14 May 2013

1. Introduction

Laser ablation is often associated with removal of material and is widely used for surface patterning and thin film fabrication. The former is used to dramatically alter wetting [1], mechanical, electrical and optical properties of materials [2]. Laser ablation has been studied in diverse materials using a range of wavelengths (ultraviolet to infrared), pulse durations (nanoseconds to femtoseconds) and repetition rates (kHz to MHz) for micro-fabrication to produce surface features with suitable texture and less contamination compared to other methods. More recently, femtosecond lasers have evolved as an advanced machining tool for material processing with nanometer precision [3,4] enabled by localized energy deposition due to highly nonlinear multiphoton interaction of light with matter. As a result, they provide high intensities needed to ablate material from surface quickly and cleanly, without damaging the surrounding regions. To-date, they have been employed to induce refractive index modification in 3D [5], voids [6], phase transitions and periodic nanostructures on the surface and in the bulk [7,8].

Several studies, both experimental and theoretical, have focused on the underlying physics of femtosecond laser-matter interaction to optimize and develop various applications of laser ablation. Measurement of ablation depth/etch rates, surface swelling, melting and thermal damage combined with investigation of ablation dynamics using pump-probe techniques provided some mechanistic insights into the process. The highly non-equilibrium character of the laser-induced processes are often described by a two-temperature model that couples electron temperature with the lattice temperature [9, 10]. Subsequent expansion of evaporated material plume and the formation of plasma within the plume are studied using hydrodynamic models [11, 12] and Monte Carlo simulations [13, 14].

In spite of these advances, the mechanisms responsible for material removal by ultrashort laser pulses still remain controversial [15]. In addition, the question of whether ablation starts with direct material removal or with surface swelling followed by material ejection has never been clearly addressed in bulk materials. Surface swelling has mostly been observed in thin metal [16, 17] and polymer films and has been attributed to spallation - strong mechanical effects that play a role during laser excitation resulting in physical separation of a thin layer from the substrate. Polyimide foils under nanosecond UV-laser induced surface irradiation [18] have shown three different regimes with increasing fluence such as, (a) real material removal (ablation), (b) swelling of the irradiated area above the level of the untreated surface (hump formation) and (c) lowering of the irradiated area below the level of the untreated surface (dent formation). Polycarbonate and PMMA (both doped and undoped) foils have also been investigated under femtosecond laser irradiation and surface swelling always accompanied ablation [19,20]. Recently, surface swelling has been reported as the first step in ablation of bulk metals [21] and has also been observed in ablation of fused silica glass [22].

Microscopic models based on molecular dynamics (MD) approach [23] were employed to investigate fast dynamic material response to short pulse laser irradiation in metal films [24,25], semiconductors [26,27] and dielectrics [28]. The MD approach is also an important method in polymer studies [29]. In MD simulation, the atoms interact with each other via a predefined potential, and their motion is tracked at every time step. MD simulations in metals suggested spallation is initiated by void nucleation and growth, both in size and numbers, followed by void coarsening and coalescence [25]. Long after the interaction of the incident laser pulse, a thick layer of material re-solidifies in a foamy state with holes and voids, leaving a bump, which extends above the original surface level [21]. However, a complete and coherent picture of how ablation is established in bulk materials especially in polymers is yet to emerge.

In this paper, we report ablation of bulk PMMA with a single femtosecond laser pulse and show that swelling of the material surface always precedes any large scale material ejection. We show that ablation evolves from surface swelling as higher pulse energies puncture a hole at the

#187454 - $15.00 USD Received 20 Mar 2013; revised 26 Apr 2013; accepted 6 May 2013; published 14 May 2013

centre of the swollen structure that gradually increases in size. Concurrently, the height of the swollen structure decreases while the depth of the ablated hole increases. We demonstrate that the pulse energy at which the ablated hole size coincides with size of swelling is $\sim$ 1.5 times that of the threshold for surface swelling and is independent of laser polarization suggesting existence of two energy thresholds corresponding to surface swelling and material removal being dominant. MD simulation of interaction of femtosecond pulses with PMMA in 2D using a computational cell consisting of 40 million particles with dimensions of $\sim 2\mu$m$\times 2\mu$m demonstrate void formation and material swelling are important mechanisms of temperature equilibration at the surface of the laser-heated sample.

2. Experiment

800nm light from a Ti:Sapphire laser system operating at a repetition rate of 5 kHz and producing 45 fs pulses with a peak energy of 0.5 mJ, was focused on the surface of optically polished PMMA samples (12.5$\times$12.5$\times$1.7 mm) by a 0.25NA (10$\times$) microscope objective. The back aperture of the microscope objective (8 mm) was slightly overfilled to minimize alignment errors. The position of the laser focus relative to the sample surface was accurately determined by imaging the back reflected light with a CCD camera at very low pulse energies below the ablation threshold. After locating the surface of PMMA, the glass plate at 45°, used for directing the back reflected light, was removed in order to avoid distortion of the incident polarization. A thin broadband beam sampler at the output of the laser directed a small fraction of the beam into a single-shot autocorrelator to monitor the pulse duration continuously. The pulse duration at the back aperture of the objective was measured to be 70fs after propagating through all the optics. The pulses were not pre-chirped.

Single femtosecond pulses were selected by operating the laser in an external trigger mode. A gradient neutral density filter was used to vary the pulse energy from 200nJ to 5μJ. The pulse energy was varied in steps of 50nJ up to 1μJ and in steps of 100nJ thereafter. A calibrated fast photodiode operating in the linear regime monitored the incident power. The incident pulse energies were measured after the microscope objective taking into account the transmission and reflection losses of all the optics. The polarization of the incident light was varied by a half-waveplate (quarter- waveplate) to obtain linearly (circularly) polarized light.The PMMA sample was mounted on three-axis translation stages with a resolution of 50nm along the lateral dimensions (X, Y) and 100 nm along the axial direction (Z).

The laser-ablated regions were characterized by a scanning electron microscope (SEM) after gold coating the PMMA surface with a thin layer (few nanometers) to make them conductive. All SEM images were taken with the electron beam perpendicular to the sample (zero tilt). The spot size was obtained from the slope of semi-logarithmic plot of the squared diameter of the modified region measured with the SEM as a function of pulse energy. We obtained a Gaussian beam radius of 2.7$\pm$0.2μm for the 0.25NA microscope objective (close to the diffraction-limited beam radius of $\sim 2\mu$m) and used it to calculate the laser fluence values. The lowest energy at which ablation features were visible under SEM was defined as the threshold value.The single shot ablation threshold of PMMA was determined to be 0.6μJ corresponding to a laser fluence of 2.6 J/cm^2, in good agreement with the published data [19].

Laser induced surface topology was investigated by an Atomic Force Microscope operating in contact mode with a pyramidal cantilever having a half-cone angle of 35°, tip height of 3.5μm and a spring constant of 69$\pm$1pN/nm tracing the sample with $<$10nN in radius of curvature. Images were captured with a relative tip speed of 1μm/sec. The typical lateral and vertical resolutions were 30nm and 0.1nm respectively.

#187454 - $15.00 USD Received 20 Mar 2013; revised 26 Apr 2013; accepted 6 May 2013; published 14 May 2013

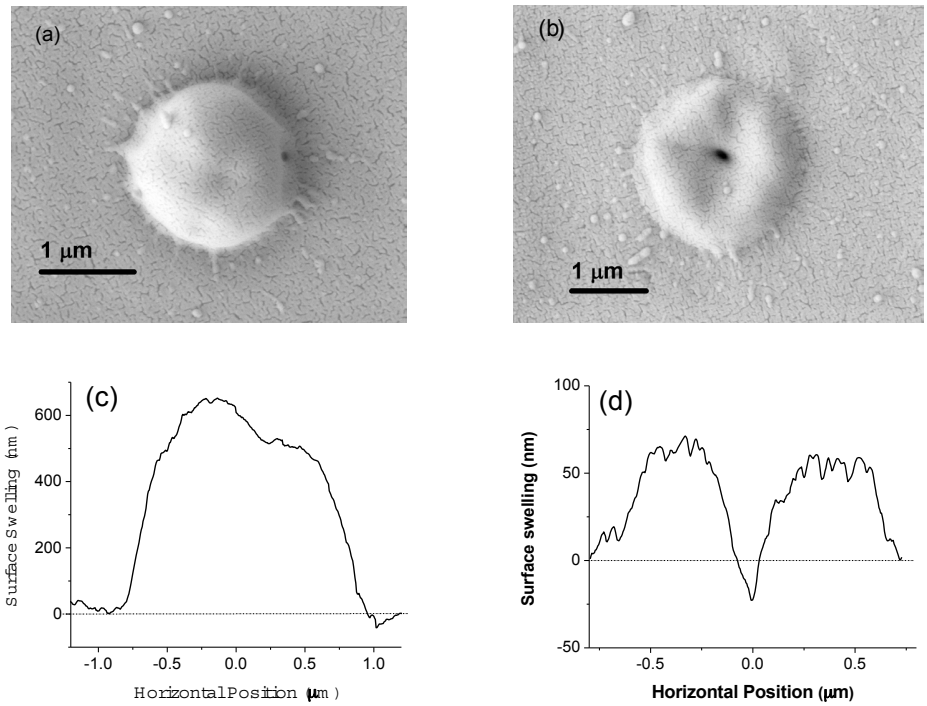

Fig. 1. Surface topography induced by a single femtosecond laser pulse in bulk PMMA. SEM images of material swelling produced by (a) circularly polarized light with a pulse energy of 640 nJ and (b) linearly polarized light with a pulse energy of 650 nJ. Respective AFM cross-sections are shown in (c) and (d) with the dashed line representing the surface before laser-irradiation.

2.1. Results

Figure 1(a) shows SEM image of PMMA surface irradiated by a single, circularly polarized femtosecond pulse of energy 640nJ. This pulse energy is slightly above the damage threshold in PMMA below which no observable surface effects could be discerned in SEM. A smooth, near circular dome like structure is formed that extends to $\sim$1.8μm with a tiny nanopore at the bottom of the dome to the right. The dome height is $\sim$600nm as shown in Fig. 1(c), measured by an AFM. When pulse energy is slightly increased the dome like structure collapses after a hole is formed at the centre as shown in Fig. 1(b). Although the laser polarization is linear in this case similar results are obtained with circular polarization as shown below. AFM measurements (shown in Fig. 1(d)) indicate a height of 75nm with a hole size of $\sim$110nm.

These results suggest that surface swelling is the first step in the ablation of materials with femtosecond lasers and that ablation proceeds with perforation of the dome like swollen surface structure. Figure 1(b) also suggests the region underneath the swollen structure is hollow resulting in the collapse of the dome when punctured at higher pulse energy. Presence of radial ejection patterns at the edges of the dome like structure in both images along with nanodroplets in the adjacent regions indicate that surface swelling arises from molten state of the material that is re-solidified possibly due to rapid cooling during expansion.

Figure 2 shows the evolution of the laser damaged surface of PMMA from surface swelling to ablation crater with increasing pulse energy for a single laser pulse of circular polarization.

#187454 - $15.00 USD Received 20 Mar 2013; revised 26 Apr 2013; accepted 6 May 2013; published 14 May 2013

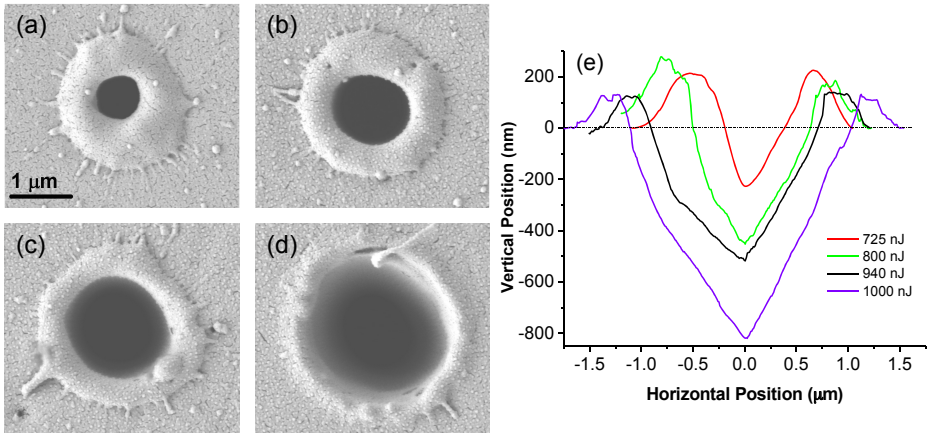

Fig. 2. SEM images showing evolution of the ablated hole within the swollen surface in PMMA induced by a single, circularly polarized femtosecond laser pulse with pulse energies of (a) 725 nJ, (b) 800 nJ, (c) 940 nJ and (d) 1 μJ corresponding to laser fluences of 3.2, 3.5, 4.1 and 4.4 J/cm^2 respectively. (e) Corresponding AFM cross-sections showing dependence of swelling and ablation hole dimensions for same incident pulse energies.

At pulse energies higher than 640 nJ, a pore formed at the centre of the dome like swollen structure renders it a doughnut shape (Fig. 2(a)). As pulse energy increases, the extent of the laser modified region and the overall pore size increases but the width of the doughnut rim decreases (Fig. 2(b) and 2(c)). When pulse energy is one half of the damage threshold the rim like structure surrounding the ablated hole vanishes as the hole size coincides with the size of swelling. Figure 2(e) shows the corresponding AFM cross-sections. Material removal commences at a pulse energy of $\sim$650 nJ (Fig. 1(b)) and at 725 nJ, the depth of the ablated hole is $\sim$225 nm with an annular protrusion of $\sim$225nm and a width of $\sim$ 640 nm. With rising pulse energy, the ablated hole diameter and depth increases while the height of the annular protrusion decreases.

The dependence of ablated hole and swelling width on incident pulse energies is shown in Fig. 3(a) for linear and circular polarizations. For both polarizations, the ablated hole and swelling size increases almost linearly with applied pulse energy up to 1.1 μJ. However, the hole size increases at a much faster rate of $\sim$6.5nm/nJ compared to $\sim$3nm/nJ rate at which the swelling increases. Beyond 1.1μJ, both ablated hole and swelling size grow at a slower rate of $\sim$0.8nm/nJ. Figure 3(b) shows the comparison between AFM cross-sections for circularly and linearly polarized light at similar pulse energies (725 nJ and 690 nJ respectively) suggesting no polarization dependence of surface swelling and subsequent material ejection at higher pulse energies.

3. Numerical simulations

The femtosecond laser ablation process can be characterized by at least three distinct stages separated by their time-scales. (1) Laser-matter interaction stage where plasma is formed and heated due to the collisional absorption processes on a time-scale on the order of several tens of femtosecond, determined primarily by the laser pulse duration. (2) Collisional transfer of energy from the laser-produced electron gas to the molecular structure with a characteristic time on the order of several hundred femtoseconds [30]. This is somewhat longer than the characteristic electron recombination time scale ($\sim$one hundred femtoseconds [31]), which thus

#187454 - $15.00 USD Received 20 Mar 2013; revised 26 Apr 2013; accepted 6 May 2013; published 14 May 2013

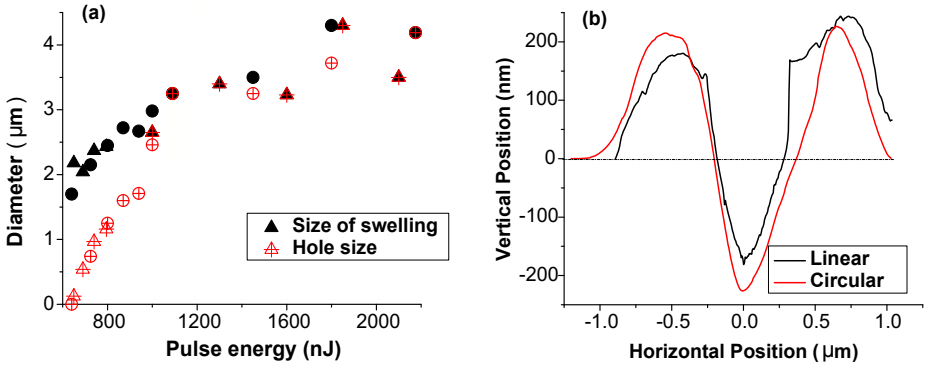

Fig. 3. (a) Dependence of diameter of the ablated hole (open symbols) and swelling (closed symbols) on incident pulse energies for linear (up-triangles) and circular (circles) polarizations. (b) Comparison of AFM cross-sections for circularly and linearly polarized light at pulse energies of 725 nJ and 690 nJ, respectively.

appears to be the dominant mechanism of energy transfer from the laser-produced plasma to the molecular structure. (3) Temperature equilibration process with a characteristic time-scale of picosecond to nanoseconds determined by the speed of sound in PMMA ($\sim 2.7 \times 10^3$ m/s $=$ $2.7\,\mu$m/ns) that can lead to surface swelling, material ablation and formation of mechanical defects.

Below we present phenomenological simulations aimed at understanding the general mechanics of thermal processes leading to formation of the dome-like structures and ablation craters in bulk samples. We consider only the third stage of the interaction, assuming that the first two stages have produced a certain temperature profile in the sample that is taken as initial condition in the simulations. We also assume that the particle density profile is minimally perturbed during the first two fast processes. As a result, the initial particle density distribution is considered to be uniform within the sample.

3.1. Methods

We use molecular dynamics (MD) approach to model interaction of femtosecond laser pulses with PMMA as it is naturally capable of describing the non-equilibrium phase transition processes at atomic level. In contrast, hydrodynamic models that are typically used to describe thermal processes in bulk samples have been shown to encounter serious challenges when extended to ultrafast laser ablation [32] due to fundamental difficulties in describing highly non-equilibrium phase transition processes along with the necessity to resolve microscopic processes.

Several MD models, differing in accuracy and computational requirements, have been developed for microscopic description of polymers and their properties under a wide range of conditions [29]. In principle, MD models can also support polymer chain-break processes with a little overhead. However, a more-or-less realistic description of polymer chains necessarily requires an actual 3D representation. MD simulations in bulk in 3D is a computationally daunting task even for largest supercomputers employing the coarse-gain MD model. To reduce computational requirements, cell dimensions on the order of few 10's to 100's of nm (much smaller than the laser spot size) are typically used in 3D with approximately few hundred thousand particles. As a result plane wave approximation is used for the incident light ignoring the gaussian spatial profile of the laser.

#187454 - $15.00 USD Received 20 Mar 2013; revised 26 Apr 2013; accepted 6 May 2013; published 14 May 2013

In this paper, we use a 2D phenomenological model with computational cell dimensions on the order of the laser spot size that enables us to consider the spatial profile of the laser. The interaction between individual atomic entities is described by the Lennard-Jones potential

$$V(r) = 4\varepsilon_0\Big[\Big(\frac{\sigma}{r}\Big)^6 - \Big(\frac{\sigma}{r}\Big)^{12}\Big], \tag{1}$$

where σ is the characteristic length and ε_0 the characteristic depth of the potential. In this way, we only expect to learn about the qualitative dynamics of ablation process, while the particular details such as elastic properties of polymers due to their chain structure at microscopic level and formation of volatile compounds due to chain breaking will be inevitably lost. Coarse grain techniques are often used where few atoms, monomers or even the whole molecular chain are grouped together to reduce computational requirements. The impact of reduced chemical detail on structural and dynamical properties of PMMA has recently been investigated where different approximations used in the MD simulations have been shown to provide adequate agreement with experimental data [29]. With the use of atomic picture in our simulations we anticipate the loss of details not to be detrimental in extracting qualitatively the thermo-mechanical properties of polymers.

Since simulations are phenomenological, the particular values of ε_0 and σ can vary. For different molecules, ε_0/k_B can be on the order of $10^2 - 10^3$ K, where k_B is Boltzmann constant, and σ can be on the order of $0.25 - 0.6$ nm [33]. The actual simulations were performed using dimensionless units. The dimensionless coordinate, time and temperature are, corrsepondingly, $\tilde{r} = r/r_0$, $\tilde{t} = t/t_0$ and $\tilde{T} = T/T_0$, where $r_0 = \sigma$, $t_0 = \sqrt{m\sigma^2/\varepsilon_0}$ and $T_0 = \varepsilon_0/k_B$. For example, if one uses $\sigma = 0.3$ nm, $\varepsilon_0/k_B = 10^3$ K and $m = 18\,m_p$, where m_p is the proton mass, that is close to parameters of water, one obtains $x_0 = 0.3$ nm, $t_0 = 0.4$ ps and $T_0 = 1000$ K.

In our simulations, we use the freely available LAMMPS code (http://lammps.sandia.gov [34]). We use $\sim 4\times 10^7$ particles on a 2D hexagonal lattice occupying $\sim 6000\times 6000\,\sigma^2$ area ($\sim 2\times 2\,\mu$m for $\sigma = 0.3$ nm). A single simulation run consists of two stages. Initially, the atomic entities are motionless and located at the nodes of the lattice in the equilibrium state. During the first stage of simulations, the sample is annealed in the Nose-Hoover thermostat with a slowly increasing temperature, until the room temperature T_r is reached ($T_r \sim 0.75\,T_m$, where T_m is the melting temperature, equal to $\sim 0.41 T_0$ for the hexagonal 2D lattice [35]). Thus, an initial unperturbed equilibrium state is created.

At the beginning of the second stage of simulation, particle velocities are scaled up by a factor proportional to the square root of temperature profile $T(\vec{r},0)$ corresponding to the non-equilibrium configuration created by the laser pulse (Fig. 4 at $t = 0$). The particles are then propagated self-consistently by the LAMMPS NVE solver, while a thin layer near $y = y_{min}$ and $y = y_{max}$ is kept at constant temperature to mimic a bulk thermal reservoir. In a typical simulation, the second stage takes $\sim 10^7$ time steps to reach a stable equilibrium (completely frozen state) for a single time step $\delta t = t_0/400$.

The temperature profile $T(\vec{r},0)$ is determined by the spatial distribution of the energy transferred from the laser beam to the molecular structure:

$$T(\vec{r},0) \approx T_r + \delta\mathscr{E}_i + \delta\mathscr{E}_{ca}, \tag{2}$$

where $\delta\mathscr{E}_i$ is the laser pulse energy transferred to the electrons in the ionization process and $\delta\mathscr{E}_{ca}$ is the pulse energy absorbed by electrons in the collisional absorption process. T_r is the room temperature.

Assuming that multi-photon ionization is the dominant ionization process in the near-threshold interaction and perturbation of the laser propagation by the resultant plasma is negli-

#187454 - $15.00 USD Received 20 Mar 2013; revised 26 Apr 2013; accepted 6 May 2013; published 14 May 2013

gible, one can write

$$\delta\mathscr{E}_i \propto \left(\frac{I(\vec{r})}{I(\vec{r}_f)}\right)^N, \tag{3}$$

where $I(\vec{r})$ is the spatial profile of the unperturbed laser pulse, $\vec{r}_f$ is the position of the laser best focus and N the order of multi-photon absorption process, $N = 3$ in the case of PMMA. In Eq. (3), a simple rate equation for multi-photon ionization rate is used. In order to estimate the extent of the laser profile perturbation by the plasma that is formed during the interaction one can calculate the energy density required to generate plasma of critical electron density ($n_{cr} = 1.75 \times 10^{21}\,\mathrm{cm}^{-3}$ for the laser wavelength $\lambda = 0.8\,\mu$m in vacuum):

$$W_{ion} n_{cr} \approx 4\,\mathrm{eV} \times 1.75 \times 10^{21}\,\mathrm{cm}^{-3} = 7 \times 10^{21}\,\mathrm{eV/cm}^3, \tag{4}$$

where W_{ion} is the ionization potential. The heat capacity of PMMA at room temperature is $\sim 1\,\mathrm{J/(cm^3K)} \approx 6 \times 10^{18}\mathrm{eV/(cm^3K)}$. Thus, the energy required to produce plasma of critical density can be sufficient to locally heat the sample by more than 1000 K. Our simulations below indicate that significant thermal processes can take place in the sample heated by (1 – 1.5) T_r above the unperturbed temperature, i.e., by ∼300–400 K. Since a part of this energy is produced in the collisional plasma heating process, we conclude that the plasma density in the near-threshold regime is well below critical density that justifies our assumption of negligible perturbation of the laser propagation by the generated plasma.

The collisional absorption of laser energy by plasma is a nonlinear process that is dependent on the distribution function of electrons at each time moment. Thus, $\mathscr{E}_{ca}$ is dependent not only on the produced plasma density n, but also directly on the laser intensity. However, since the inverse Bremmstrahlung absorption is only one of the energy transfer mechanisms from the laser pulse and nonlinearity in $n(I)$ is very strong, the extra dependence on the laser intensity due to the details of the collisional absorption process is expected to result only in perturbation of the overall laser energy deposition profile in the sample. In this way, to keep our parameter space small, we assume, similar to Eq. (3),

$$\delta\mathscr{E}_{ca} \propto \left(\frac{I(\vec{r})}{I(\vec{r}_f)}\right)^N. \tag{5}$$

The overall temperature profile in the sample assumed at the beginning of the thermal stage is thus

$$T(\vec{r},0) \approx T_r \cdot \left[1 + \alpha \cdot \left(\frac{I(\vec{r})}{I(\vec{r}_f)}\right)^N\right], \tag{6}$$

where α is a parameter of simulations. The particle velocities used at the second stage of simulation are therefore scaled up by factor $\sqrt{1 + \alpha \cdot \left(I(\vec{r})/I(\vec{r}_f)\right)^N}$.

3.2. Simulations results

Dynamics of a typical bump formation process is illustrated in Fig. 4 for $\alpha = 1.45$. The laser is incident on the sample surface at x/σ = 0. The temperature distribution follows the energy deposition and spatial profile of the laser and is highest at y/σ = 0 and penetrates deeper into the sample. In a few tens of t_0, corresponding to few picoseconds after the start of simulation (represented by t_w obtained for a particular choice of parameters) , the initial non-equilibrium process gives rise to a strong pressure shock that propagates with a supersonic velocity outwards from the hot area and eventually decays, after several subsequent reflections from the boundaries of the simulation sample. The shockwave traverses the simulation domain in about 150 ps.

#187454 - $15.00 USD Received 20 Mar 2013; revised 26 Apr 2013; accepted 6 May 2013; published 14 May 2013

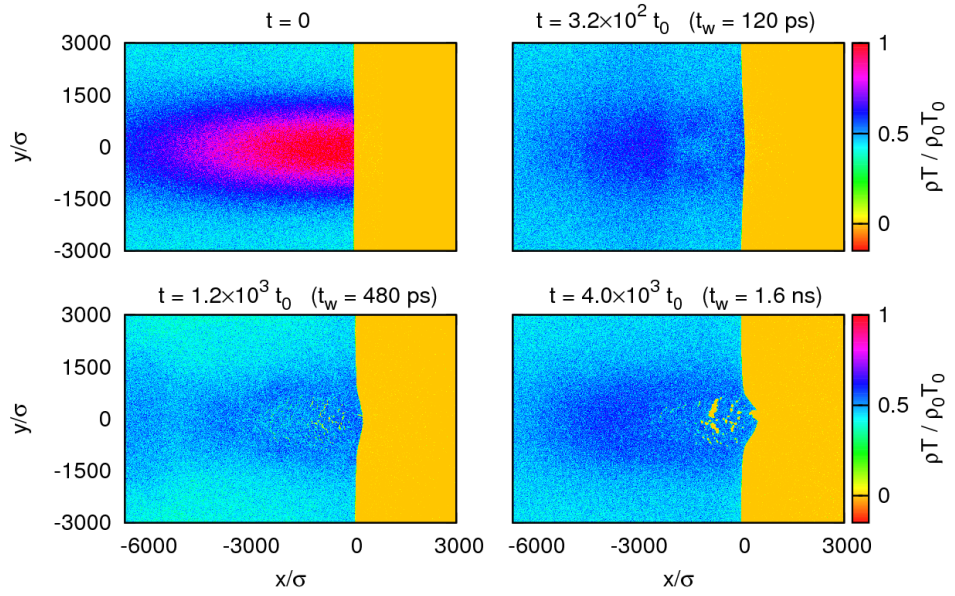

Fig. 4. (Characteristic dynamics of thermal processes and bump formation in the laser-heated sample. Density weighted temperature profiles are shown at different time steps for $\alpha = 1.45$. The laser is incident from the right on the sample surface located at x/σ = 0 and centred at y/σ = 0. Simulation domain size of x/σ = y/σ = 6000 corresponds to sample dimension of $\sim 2\mu$m$\times 2\mu$m. Time t_w is obtained from dimensionless unit for a particular choice of parameters specified in the text.

The next state of equilibration, that can correspond to few tens of picoseconds, is characterized by formation of gaseous nanopores inside the overheated area and its rapid cooling (Fig. 4, $t = 3.2 \times 10^2 t_0$). The temperature profile in Fig. 4 at $t = 3.2 \times 10^2 t_0$ shows formation of nanopores in a region that is initially the hottest with corresponding temperatures that are cooler than the surrounding material. Thus, the nanopores formation is an important mechanism of temperature equilibration. Near the boundary of the sample, pressure gradient leads to expansion of the porous material outwards that leads to formation of a bump at the sample surface (Fig. 4, $t = 1.2 \times 10^3 t_0$). This process is accompanied by the growth of the nanopores, that eventually coalesce to form larger pores (Fig. 4, $t = 4.0 \times 10^3 t_0$). The surface bump at this stage develops large mechanical defects that, depending on the deposited energy, either increases further at later time and result in an open crater or freeze and form the swollen structure with a perforated hole that is seen in the experimental images described in the previous section. The height of the bump/swelling increases at a rate of $\sim$13 nm for every 100 ps up to few ns in time. Beyond 10 ns simulations do not show any changes in the surface topography although thermal processes continue for longer times.

Figure 5 shows the density profiles of the interaction region after $2.5 \times 10^4 t_0$ (corresponding to ten to few tens of ns after the interaction that is long enough for re-solidification to occur) for different values of the simulation parameter α. For $\alpha = 1.1$, only nanopores and irregularities appear to be present under the sample surface that appear as brighter regions in the figure. A small crack visible near the surface can be attributed to the dimensionality of the computation cell (relatively small size of our sample that is comparable to the laser spot size) and the stiffness of the sample surface. The shock produced by the initial temperature gradient could not be

#187454 - $15.00 USD Received 20 Mar 2013; revised 26 Apr 2013; accepted 6 May 2013; published 14 May 2013

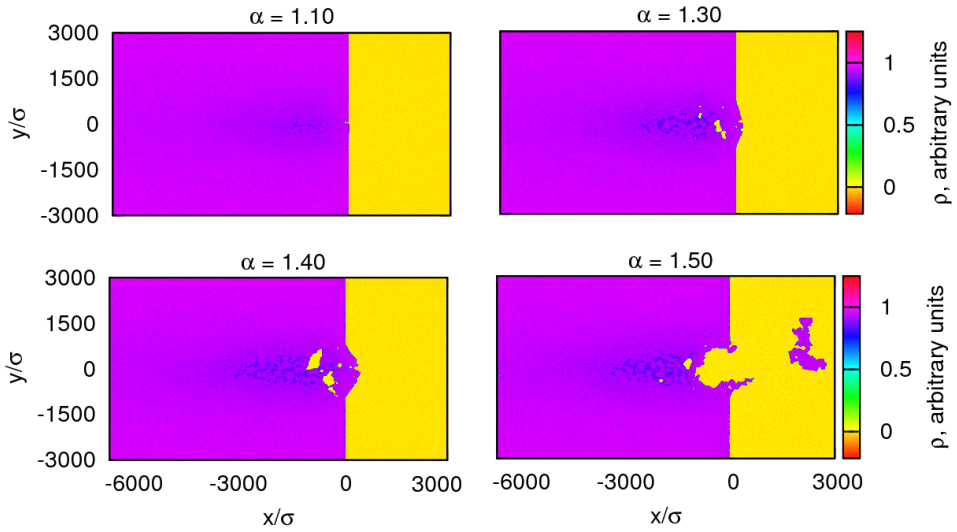

Fig. 5. Particle density profiles $2.5 \times 10^4 t_0$ (~ 10 ns) after the interaction of light with the sample for different values of α corresponding to different pulse energies.The laser is incident from the right on the sample surface located at x/σ = 0 and centred at y/σ = 0. Dimensions of sample used in the simulation are $\sim 2\mu$m$\times 2\mu$m corresponding to x/σ = y/σ = 6000.

completely overcome by the Lennard-Jones walls of the simulation domain. At higher α when the material becomes softer the crack does not appear.

For $\alpha = 1.3$ some of the irregularities in the density coalesce to form sub-surface voids that leads to the formation of a small bump at the sample surface. Mechanical stretching of the thermally softened sample surface leads to formation of micropores on the swollen surface. As α is increased to $\alpha = 1.4$, the sub-surface voids and the surface bump grow in size. A deeper and larger hole is formed on the surface bump that can be interpreted as a central pore observed in the experiment. As the α is increased to $\alpha = 1.5$, the internal pressure in the sample becomes sufficiently large to detach large chunks of material from the sample creating an ablation crater with a porous structure at its bottom that has previously been observed in experiments on PMMA [36].

4. Discussion

Surface swelling induced by ultrashort laser pulses that we observed in bulk PMMA is not the same as that has previously been observed in metal films [16, 17]. There the mechanism is attributed to spallation – a photomechanical process where a reflected pressure wave leads to material ejection typically at the back surface of the sample. MD simulations of small material slabs provided insights into the thermo-mechanical dynamics of irradiated films including coupling-decoupling of ablation and spallation processes [24]. However, the bulk nature of our sample excludes the influence of a substantial reflected pressure wave.

Our simulations demonstrate formation of nanopores in the subsurface region of highly excited material due to the interaction of intense short pulses with the sample. Pressure gradients near the sample boundary causes the porous material to expand outwards forming a bump at the sample surface. This is accompanied by growth and coalescence of voids in the subsurface region. The evolution of voids determined by the competition between the laser-induced stresses

#187454 - $15.00 USD Received 20 Mar 2013; revised 26 Apr 2013; accepted 6 May 2013; published 14 May 2013

20 May 2013 | Vol. 21, No. 10 | DOI:10.1364/OE.21.012527 | OPTICS EXPRESS 12537

and thermal softening of the irradiated surface can lead to spallation, fragmentation and ejection of material. This is similar to front-surface laser spallation predicted by hydrodynamic [37] and MD modelling [25, 38, 39].

Simulations also suggest surface swelling to increase with α (pulse energies) up to a certain value beyond which mechanical stretching of the sample surface leads to formation of a central pore (Fig. 5(c)) as observed in experiments. Further increase in α (not shown) leads to an increase in the hole size. At high α, material removal becomes dominant and surface swelling can no longer be observed. The α at which hole and swelling sizes coincide is 1.3 times the threshold α at which only swelling is observed. Experimentally, this ratio was found to be 1.5. Time-resolved measurements of femtosecond laser induced surface swelling in metal foils have observed a similar threshold fluence that separates the regime where a dome like structure (unbroken shell) is formed from the regime with the dome (shell) having an aperture [40].

Our simulations in bulk material, albeit in 2D, indicate that a two phase expanding liquid-vapour mixture fills the volume between the shell and bottom of the crater consistent with other simulations [25, 40] and experiments [21] carried out in metal foils. However, the collapse of dome like structure in Fig. 1(b) at slightly higher fluence suggests the inside is hollow. This could be specific to PMMA and other polymers. In addition to the laser-induced subsurface liquid-vapour mixture that expands, another potential source of gaseous products can be polymer fractionation by CO-O bond breaking [19]. Irrespective of the relative contributions, localized bursting of the expanding surface results in collapse of the dome structure.

5. Conclusion

We demonstrate that surface swelling is the first step in interaction of intense femtosecond pulses with bulk dielectrics. This is followed by material ejection and ablation only when laser fluence/pulse energy is increased. The threshold fluence at which ablation becomes dominant with no reminiscents of surface swelling is approximately one and half times the threshold for surface swelling and is independent of laser polarization. These results have implications in ultrafast micro-machining applications when combined with previous observations of polarization dependent elongation of ablated holes at fluences greater than twice the ablation threshold [36]. There appears to be a small range of laser fluences where clean holes and cuts are feasible. At low fluences, surface swelling dominates and at high fluences ablation dominates but polarization effects can become prominent. Detailed time-resolved experiments extending to longer times will shed more light on swelling dynamics. Our molecular dynamics simulations provide physical insight into swelling dynamics showing that (a) bump formation is not connected to laser induced shock but to the formation of porous structure below the sample surface, and (b) no significant evaporation occurs from the surface at threshold fluences. Large scale simulations that take into account the molecular structure of PMMA and involves sample sizes comparable to the laser spot size are essential to gain further insight into the nonlinear interaction of light with matter.

Acknowledgments

The authors acknowledge the financial support from Natural Science and Engineering Research Council of Canada, Canada Research Chairs, Canadian Foundation for Innovation and Ontario Ministry of Economic Development and Innovation. Z.A is supported by NSERC-CREATE in Quantitative Biomedicine fellowship. Computations were performed on the Southern Ontario Smart Computing Innovation Platform (SOSCIP) BlueGene/Q supercomputer located at the University of Toronto's SciNet HPC facility.

#187454 - $15.00 USD Received 20 Mar 2013; revised 26 Apr 2013; accepted 6 May 2013; published 14 May 2013

4.3 Polarization-dependent femtosecond laser ablation of poly-methyl methacrylate (Publication 2)

J-M Guay, A. B. Villafranca, **F. Baset**, K. Popov, L. Ramunno, and V. R. Bhardwaj
Polarization-dependent femtosecond laser ablation in poly-methyl methacrylate
New Journal of Physics **14** 085010 (2012)

4.3.1 Author contribution

The published results come from experiments performed by F. Baset, A. B. Villafranca, J-M Guay and V. R. Bhardwaj at Ultrafast Photonics lab, University of Ottawa, ON. F. Baset and J-M Guay performed preliminary experiments (unpublished data) under supervision of V. R. Bhardwaj. F. Baset, A. B. Villafranca and J-M Guay conducted the analysis of the results and F. Baset created the figures. Theoretical simulation had been performed by K. Popov and L. Ramunno. V. R. Bhardwaj wrote the first draft of the manuscript. All authors contributed to the final manuscript.

CE by: SDB UK English NJP423611 on 6 July 2012

New Journal of Physics
The open-access journal for physics

Polarization-dependent femtosecond laser ablation of poly-methyl methacrylate

J-M Guay, A Villafranca, F Baset, K Popov, L Ramunno and V R Bhardwaj[1]

Department of Physics and Center for Research in Photonics,
University of Ottawa, 150 Louis Pasteur, Ottawa, ON, K1N 6N5, Canada
E-mail: [redacted]@uottawa.ca

New Journal of Physics **14** (2012) 000000 (17pp)
Received 17 February 2012
Published xxx
Online at http://www.njp.org/
doi:10.1088/1367-2630/14/7/000000

Abstract. We show that ablation features in poly-methyl methacrylate (PMMA) induced by a single femtosecond laser pulse are imposed by light polarization. The ablation craters are elongated along the major axis of the polarization vector and become increasingly prominent as the pulse energy is increased above the threshold energy. We demonstrate ∼40% elongation for linearly and elliptically polarized light in the fluence range of 4–20 J cm^{-2}, while circularly polarized light produced near circular ablation craters irrespective of pulse energies. We also show that irradiation with multiple pulses erases the polarization-dependent elongation of the ablation craters. However, for line ablation the orientation of the electric field vector is imprinted in the form of quasi-periodic structures inside the ablated region. Theoretically, we show that the polarization dependence of the ablation features arises from a local field enhancement during light–plasma interaction. Simulations also show that in materials with high nonlinearities such as doped PMMA, in addition to conventional explosive boiling, sub-surface multiple filamentation can also give rise to porosity.

[1] Author to whom any correspondence should be addressed.

Contents

1. Introduction

Light–matter interactions are often governed by the intensity, wavelength and polarization of light. When ultrafast lasers are used, pulse duration also affects the energy coupling and dissipation in the system. The role of polarization of light in the interaction of atoms and molecules with intense femtosecond light pulses is well understood and is often exploited to align molecules [1–3] and to control electron dynamics in the laser field with a high degree of spatial and temporal precision [4, 5]. The latter is crucial in attosecond science [6, 7]. However, the role of polarization in the interaction of intense light pulses with solids is subtle and not clear.

The interaction of tightly focused intense femtosecond light pulses with solids often leads to ablation of the material surface or refractive index modification in transparent materials [8, 9]. Several mechanisms are involved in the interaction, some of which depend on the laser polarization that can potentially leave an imprint on the modification/ablation process. For example, both processes (ablation/modification) are initiated by multi-photon ionization that depends on light polarization. In crystalline dielectrics, multi-photon ionization depends on sample orientation due to direction dependence of the effective mass of the electron [10]. This is similar to multi-photon ionization in molecules where the rates differ by more than 50% depending on the alignment of the molecular axis with respect to linearly polarized light [11, 12].

In addition to multi-photon ionization, impact ionization can also occur, rapidly increasing the carrier density and forming a plasma that either expands (as in ablation) or is confined in the bulk (as in internal modification). Subsequent interaction of the incident light with the plasma can lead to polarization-dependent absorption. Experiments on laser-produced plasmas have demonstrated sharp differences (up to 50–60%) in absorption of p- and s-polarized light due to resonance absorption [13, 14]. In addition, the interaction of linearly polarized light with dense plasma can also lead to local field enhancements akin to that observed in metal nanoparticles [15].

To date, signatures of polarization-dependent phenomena have been observed mostly in the multiple pulse regime both on surfaces and inside bulk materials. Polarization-dependent

self-organized three-dimensional (3D) periodic nanostructures have been observed inside fused silica [16, 17] under irradiation with multiple light pulses. For linearly polarized light, bulk grating-like structures were formed orthogonal to the laser polarization and their origin was attributed to local field enhancement arising from light–plasma interaction [17–19]. Such polarization-dependent nanostructures have found applications in rewritable 3D data storage [20], embedded microarray optics and microfluidics [21, 22]. For circularly polarized light, the handedness of the light was imprinted in the form of ordered sub-micron chiral structures [23]. The ability to imprint the electric field in the form of oriented nanostructures has recently been exploited to develop a sub-wavelength resolution diagnostic tool to visualize the complex polarization state of the light in the focal volume [24].

Laser-induced polarization-dependent periodic structures (or surface ripples) have also been observed on surfaces in the ablation crater of a variety of materials including dielectrics, semiconductors and metals under widely different illumination conditions [25–28]. Ripple spacing of the order of wavelength to sub-wavelength [29–34] has been observed and varies with the fluence and the number of laser pulses. Moreover, the structures have been found to be predominantly perpendicular to the laser polarization. The ripple formation is described in terms of interference between the incident light and the surface scattering wave [35] or surface plasmon polaritons [36]. Ripple structures parallel to the laser polarization have also been observed in the ablation crater [37, 38].

Apart from surface ripples within the interaction region the overall features of the ablation region were found to be polarization dependent. Experiments on multiple pulse ablation of thin metal films exhibited elongation of the ablation craters along the major axis of the polarization vector when the pulse energy was close to the ablation threshold [39]. The elongation of ablation features gradually disappeared when the pulse energy was increased beyond the threshold value by $\sim$50%.

In this paper, we present a complete experimental and numerical study of polarization-dependent ablation of poly-methyl methacrylate (PMMA). In section 2, we describe the experimental setup and present the evolution of ablation features as a function of the pulse energy and the number of laser shots. We show that the ablation craters in PMMA are elongated along the major axis of the polarization vector whenever pulse energies exceeded the threshold value. Only circularly polarized light produces near circular ablation craters irrespective of pulse energies. We also show that the polarization-dependent elongation of the ablation craters vanishes for multiple laser pulses. However, for line ablation the polarization dependence is preserved in the form of quasi-periodic structures which are oriented along the laser polarization.

In section 3, we describe the 3D finite-difference time domain (FDTD) simulation of the interaction of intense light pulses with PMMA and compare it with the experimental results. This approach determines energy deposition patterns and assumes that all of the absorbed energy is eventually transferred to the lattice, resulting in ablation/modification. We show that elongation of ablation craters arises from the local field enhancement during light–plasma interaction. When the initial plasma density is above the critical density (where the light frequency is equal to the plasma frequency), field enhancement occurs parallel to the laser polarization. Faster plasma growth in the regions with enhanced fields results in an asymmetric plasma density profile, which when transferred to the lattice leads to elongation of the ablation crater. We conclude by showing that in doped PMMA with very high third-order susceptibility

sub-surface multiple filamentation can give rise to induced porosity in addition to conventional explosive boiling.

2. Polarization dependence of ablation

2.1. Experimental methods

In our experiments, 800 nm light from a Ti:sapphire laser system operating at a repetition rate of 5 kHz and producing 45 fs pulses with a peak energy of 0.5 mJ was focused on the surface of PMMA by a 0.25 NA (10×) microscope objective. The back aperture of the microscope objective (8 mm) was slightly overfilled to minimize alignment errors. The position of the laser focus relative to the surface of optically polished bulk PMMA samples ($12.5 \times 12.5 \times 1.7\,\mathrm{mm}^3$) was accurately determined by imaging the back reflected light with a CCD camera at very low pulse energies below the ablation threshold. After locating the surface of PMMA, the glass plate at 45° used for directing the back reflected light was removed in order to avoid distortion of the incident polarization.

A gradient neutral density filter was used to vary the pulse energy from 50 nJ to 5 μJ. The step size of 100 nJ was used to determine the single and multiple shot ablation thresholds. For this the laser was operated either in a single shot or in continuous mode. In the latter, the sample speed was selected such that a specific number of pulses was incident within the focal region. The PMMA sample was mounted on three-axis translation stages with a resolution of 50 nm along the lateral dimensions (X, Y) and 100 nm along the axial direction (Z). The lowest energy at which ablation features were visible under the scanning electron microscope (SEM) was defined as the threshold value. A calibrated fast photodiode operating in the linear regime monitored the incident power. The spot size was obtained from the slope of a semi-logarithmic plot of the squared diameter of the modified region measured with an SEM image as a function of pulse energy [40]. We obtained a Gaussian beam radius of $2.6 \pm 0.2\,\mu$m for the 0.25 NA microscope objective (close to the diffraction-limited beam radius of $\sim 2\,\mu$m) and used it to calculate the laser fluence values.

To study the polarization dependence, the pulse energy was varied from the threshold value in steps of 0.5 μJ. A quarter waveplate was used to produce elliptical or circular polarizations. To select s or p polarizations a polarizer was placed after the quarter waveplate. Switching the relative position of the two optics ensured that the pulse duration remained the same while changing the polarization. A thin broadband beam sampler at the output of the laser directed a small fraction of the beam into a single-shot autocorrelator to monitor the pulse duration continuously. The pulse duration at the back aperture of the objective was measured to be 70 fs after propagating through all the optics. The pulses were not pre-chirped. The incident pulse energies were measured after the microscope objective taking into account the transmission and reflection losses of all the optics.

2.2. Single-shot ablation of poly-methyl methacrylate (PMMA)

Figure 1 shows the polarization dependence of single-shot laser ablation of PMMA obtained with a pulse energy of 3.2 μJ that is ~5 times higher than the threshold value. The SEM images reveal two interesting aspects of the interaction. Firstly, the ablation craters are elongated along the major axis of the polarization vector for both linear (figures 1(a) and (b)) and elliptically

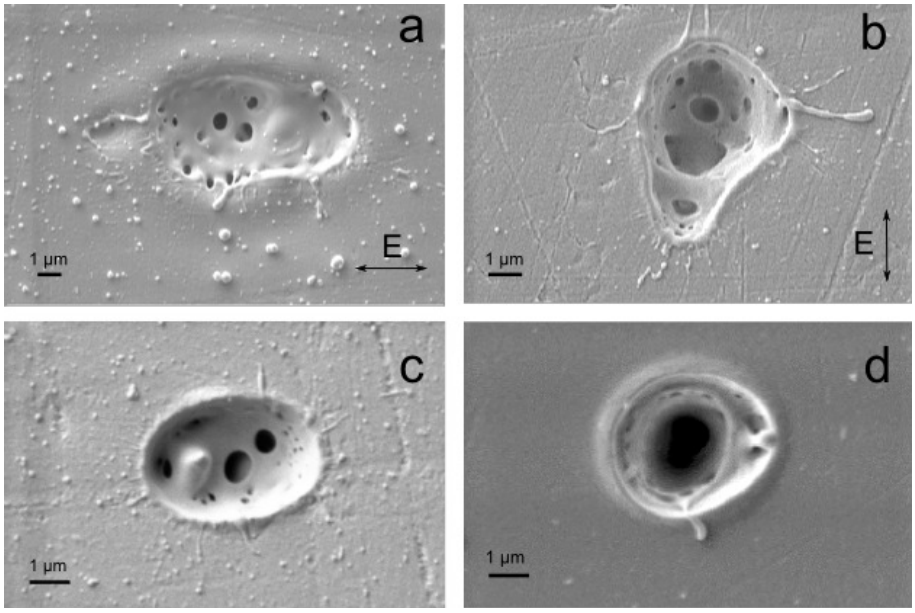

Figure 1. SEM images of single-shot ablation craters in PMMA produced by different polarizations of incident light: (a) p polarization, (b) s polarization, (c) elliptical polarization (ϵ = 0.5) and (d) circular polarization (ϵ = 0.9). $\epsilon = E_y/E_x$ is the ellipticity of light defined as the ratio of the electric fields in the two orthogonal directions. The pulse energy was 3.2 μJ, measured after the microscope objective corresponding to a laser fluence of 14.3 J cm^{-2}.

(figure 1(c)) polarized light. The ellipticity $\epsilon = E_y/E_x$, defined as the ratio of the electric fields along the two orthogonal axes, is 0.5 for the latter. Only circularly polarized light was produced near circular ablation craters (figure 1(d)), suggesting that the mechanism responsible for elongation can be turned on or off by laser polarization. The small asymmetry that can be seen in figure 1(d) is due to the fact that polarization is not perfectly circular ($\epsilon = 0.9$ instead of 1).

Secondly, the ablation of PMMA is not homogeneous; instead nanostructures are formed within the interaction region. Associated with this is the observation of nanodroplets in adjacent regions, suggesting localized melting and nano-explosions that render the material porous (see also figure 4). This process, called explosive boiling, is specific to ultrashort pulse laser irradiation where near isochoric heating and rapid adiabatic expansion result in material ejection [41–46]. While most experiments to date have studied this effect by post-mortem analysis of the laser-induced damage, only a few time-resolved experiments have investigated the fundamental physical mechanisms of the ablation process [47]. There is general consensus that after thermalization of the laser energy in the material (on the ps time scale) a two-phase liquid–gas mixture develops, which then undergoes hydrodynamic expansion, resulting in material ejection and subsequent resolidification on the ns time scale [48, 49]. It is interesting to note that both elongation of the ablation crater and formation of nanostructures within do not occur at energies close to the ablation threshold.

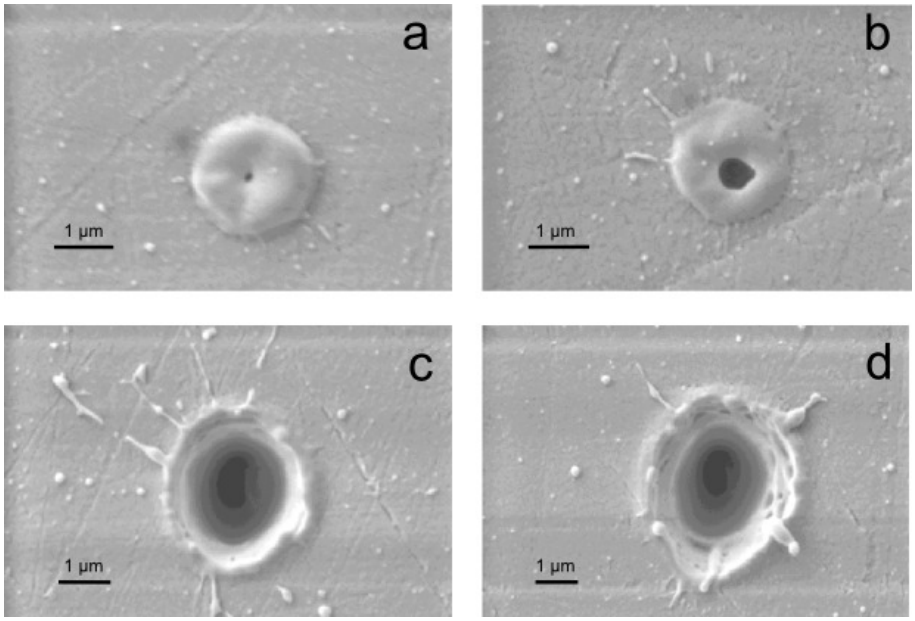

Figure 2. SEM images of single-shot ablation craters produced by s-polarized light with different pulse energies incident on PMMA. (a) 640 nJ, (b) 690 nJ, (c) 1 μJ and (d) 2.1 μJ correspond to laser fluences of 2.9, 3.1, 4.5 and 9.4 J cm^{-2}, respectively.

Figure 2 shows the evolution of single-shot ablation of PMMA as a function of pulse energies. At threshold energies, ablation occurs in a circular region starting with a swelling of the material followed by material ejection (figures 2(a) and (b)). This eliminates beam distortions as a potential contributor to elongation of ablation craters. When the pulse energy is increased, the ablation crater starts elongating along the polarization direction (figures 2(c) and (d)). Also, nanostructures start appearing along the edges (figure 2(d)) and grow into the middle as well (figure 1(a)). Figures 2(a) and (b) are reminiscent of pronounced surface swelling due to a two-phase expanding mixture that fills the volume between the shell and the bottom of the crater, followed by material expulsion [50, 51].

The polarization dependence of ablation as a function of fluence can be summarized for different polarizations in terms of an asymmetry parameter defined as the ratio of the crater dimensions along the two orthogonal axes as shown in figure 3. Near the threshold fluences, all three polarizations produce nearly identical circular ablation features (the asymmetry value is unity). At approximately twice the threshold fluence, linear and elliptical polarizations produce asymmetric ablation craters, while the circular polarization still gives rise to an asymmetry of unity. This trend continues as the fluence increases by a factor of 5. Linear and elliptical polarizations introduce an up to 40% change in the asymmetry value. The 5% change in the asymmetry associated with circular polarization could be due the value of ϵ being 0.9 instead of 1.

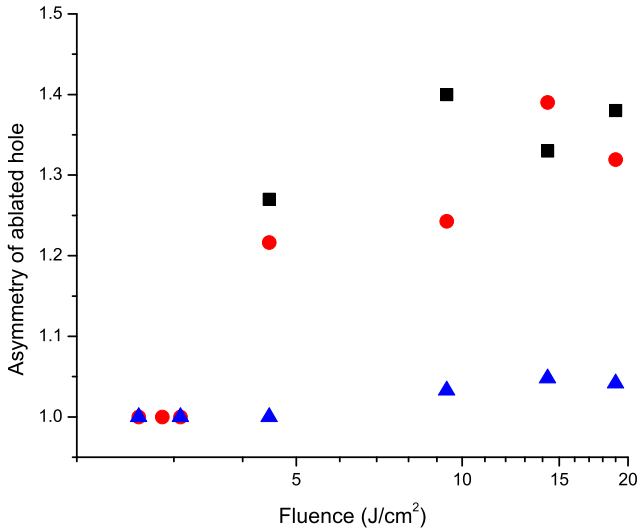

Figure 3. Asymmetry of the ablation crater as a function of laser fluence for different polarizations: linear polarization (●), elliptical polarization (■) and circular polarization (▲). The asymmetry of the ablation crater is the ratio of the dimensions along two orthogonal directions. The size of the symbols represents the errors bars.

2.3. Shot-to-shot evolution of ablation

The shot-to-shot evolution of the ablation of PMMA is shown in figure 4. Firstly, the asymmetry of the ablation crater observed with a single laser pulse disappears when multiple laser pulses are used. This effect is contrary to the observation of periodic structures inside fused silica [16, 17] and the elongation of ablation features on thin metal films [39] where multiple pulses were essential for their formation. A combination of induced porosity and modification of the material by successive laser pulses that alter the coupling of light into PMMA leads to disappearance of the polarization-dependent elongation. Secondly, the porosity evolves from being a 2D to a 3D effect as the hole gets deeper, leading to a quasi-honeycomb-like structure on the side walls (figure 4(c)).

To investigate multi-shot effects on ablation, we studied the threshold fluence as a function of the number of laser shots as shown in figure 4(d). The number of laser shots is selected by triggering the laser externally (red circles) or by moving the laser focus at speeds such that the chosen number of laser pulses were incident within the focal region (black squares). The single-shot ablation threshold of $2.6\,\mathrm{J\,cm^{-2}}$ for PMMA is in good agreement with the published data [40, 52]. However, we observe that the two- and three-shot ablation thresholds decrease faster than the reported values. As the number of laser shots increases further, the threshold fluence decreases rapidly and then saturates. This behaviour corresponds to shot-to-shot memory in the ionization of PMMA, the first step in the ablation process. This is also called the incubation effect [40]. In fused silica, memory has been associated with the change in band gap of the material where successive laser shots alter the material properties, making it easier to ionize [53].

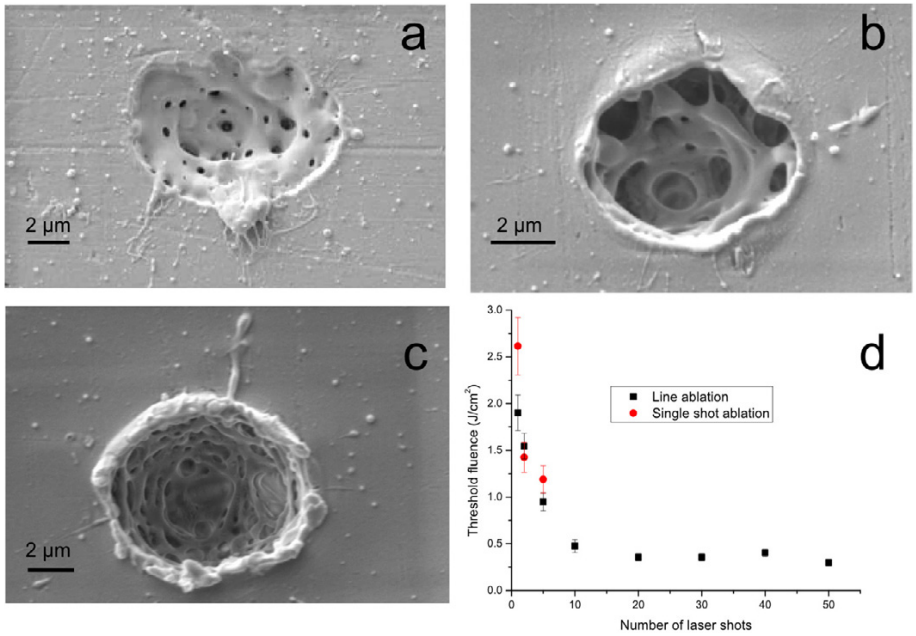

Figure 4. Shot-to-shot evolution of ablation in PMMA. SEM images of ablated regions with (a) one, (b) two and (c) five laser pulses of energy 4 μJ corresponding to a laser fluence of 19 J cm^{-2}. (d) The ablation threshold as a function of the number of laser shots. Solid circles (solid squares) are obtained by operating the laser in a single-shot mode (continuous shot mode). In the continuous shot mode, the sample speed determined the number of laser shots incident within the focal region.

2.4. Line ablation

When the laser focus is stationary, polarization-dependent elongation of the ablation crater disappears with multiple laser pulses (figures 4(a)–(c)). However, signatures of polarization dependence of the ablation features persist even when the laser focus is moved continuously at different speeds such that the number of pulses incident within the focal area varies. Figure 5 shows the SEM images of ablation lines for different orientations of linearly polarized light. The pulse energy and sample speed were 0.5 μJ and 0.5 mm s^{-1} ($\sim$10 pulses μm^{-1}), respectively. Firstly, the width of the ablation line varies with the angle, θ, between the polarization direction and the direction of motion of the sample. It is maximum when $\theta = 90^{\circ}$(2.2 μm) and decreases to 2.0 μm for $\theta = 45^{\circ}$ and is minimum at $\theta = 0^{\circ}$(1.85 μm). This is consistent with the previous observation of the Kerf width on thin metal films [39].

Secondly, quasi-periodic structures are formed inside the ablated region whose orientation is parallel to the laser polarization. In contrast, internal modification of fused silica resulted in periodic structures formed perpendicular to the laser polarization [17]. In both the cases the structure is preserved even when the laser focus is moved continuously. As we will show below, the elongation of ablated regions and the orientation of the sub-structures inside arise from local field enhancements during light–plasma interaction. Differences in the orientation of the

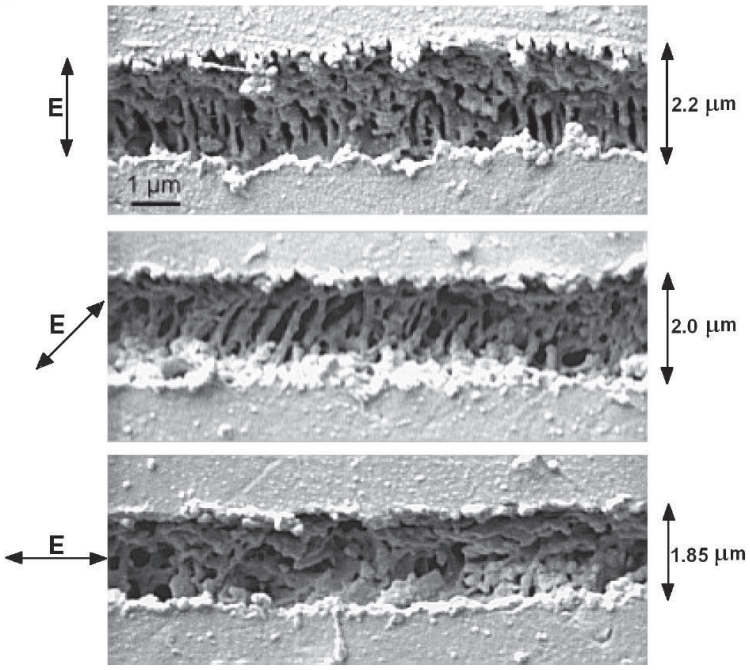

Figure 5. SEM images of ablated lines in PMMA. Arrows on the left indicate the orientation of the laser polarization with respect to the direction of motion of the sample. The width of the ablation lines is shown on the right. The pulse energy was 0.5 μJ and the sample speed was 0.5 mm s^{-1}.

quasi-periodic structures during ablation (internal modification) are associated with an overcritical (undercritical) plasma density.

3. Numerical simulation of PMMA ablation

3.1. Theoretical methods

During the laser interaction with materials, the laser energy is initially coupled to the electrons. On a time scale longer than the incident pulse duration, electron–electron and electron–ion collisions lead to thermalization, establishing a Fermi distribution within the excited electron population in the conduction band. On a much longer time scale, electrons transfer their energy to the lattice through electron–phonon coupling. Theoretically, it is challenging to develop a self-consistent hybrid model that considers both the dynamics of free electrons induced by multi-photon, tunnelling and electron impact ionizations as well as electron–electron thermalization and electron–phonon coupling that ultimately transfers energy from the electronic subsystem to the lattice. Q3

To overcome this difficulty, two different approaches are widely employed for studying laser ablation. In the first approach, the initial energy deposition patterns are assumed, and the internal distribution of the deposited energy is followed to study ablation dynamics. Hydrodynamic and molecular dynamic models that take into account atom kinetics belong

to this category. In the second approach, energy deposition patterns are determined, and it is assumed that all the absorbed energy is finally transferred to the lattice, resulting in ablation/modification that takes the shape of the plasma. It is a good approximation due to the large difference in heat capacity of the free-electron gas and phonons. Modelling the dynamics of free electrons in the conduction band by solving electrodynamic, nonlinear Schrodinger and multiple rate equations fall under this category. We use this approach to study polarization-dependent ablation of PMMA.

We have performed FDTD simulations of the fs-scale interaction process between the intense laser pulse and the PMMA sample. A detailed description of our simulation tools is given in [19]. In short, our FDTD code solves the 3D Maxwell equations in a non-magnetic material,

$$\nabla \times \vec{E} = -\frac{1}{c}\frac{\partial \vec{B}}{\partial t}, \quad \nabla \times \vec{B} = \frac{1}{c}\frac{\partial \vec{D}}{\partial t} + \frac{4\pi}{c}\vec{J}, \tag{1}$$

where $\vec{E}$ is the electric field, $\vec{D}$ the electric displacement field and $\vec{J}$ the current density. The displacement field represents the linear and third-order responses of the unmodified dielectric medium, $\vec{D} = \left[1 + 4\pi(\chi^{(1)} + \chi^{(3)}E^2)\right]\vec{E}$, where $\chi^{(1)}$ and $\chi^{(3)}$ are (frequency-independent) first- and third-order susceptibilities of the medium, respectively. The current density $\vec{J}$ is composed of two components: $\vec{J} = \vec{J}_{\mathrm{P}} + \vec{J}_{\mathrm{MPA}}$, where $\vec{J}_{\mathrm{P}}$ represents the free plasma electron motion and $\vec{J}_{\mathrm{MPA}}$ is the effective current accounting for the laser energy loss due to multi-photon absorption (or ionization process) [19, 54, 55]. The free-electron current density is evaluated in our model from the cold plasma hydrodynamics equations

$$\vec{J}_{\mathrm{P}} = -en\vec{u}, \quad \frac{\partial n}{\partial t} = \frac{\partial n_{\mathrm{MPI}}}{\partial t}, \quad \frac{\partial \vec{u}}{\partial t} = -\frac{e}{m}\vec{E} - \Gamma\vec{u}, \tag{2}$$

where n and $\vec{u}$ are plasma particle density and fluid velocity, respectively, $\partial n_{\mathrm{MPI}}/\partial t$ is the rate of change of density due to multiphoton ionization, e and m the electron charge and mass, respectively, and Γ (a constant) is the damping factor due to collisional laser energy absorption in plasma, estimated below using the Spitzer formula [56]. Equation (2) can be identified also with the equation of motion for free particles in the Drude model [57]. We assume in the simulations that the leading ionization process in PMMA is three-photon absorption, resulting in

$$\frac{\partial n_{\mathrm{MPI}}}{\partial t} = \sigma_3 I^3 \frac{n_{\mathrm{s}} - n}{n_{\mathrm{s}}}, \tag{3}$$

where σ_3 is the three-photon absorption cross-section, $I = \frac{c}{4\pi}\langle E^2\rangle$ is the laser intensity and n_{s} is the saturation density, which is estimated for PMMA as $n_{\mathrm{s}} \approx 5\,n_{\mathrm{cr}}$, where $n_{\mathrm{cr}} \approx 1.75 \times 10^{21}\,\mathrm{cm}^{-3}$ is the critical electron density for the free-space laser wavelength $\lambda_{\mathrm{fs}} = 0.8\,\mu\mathrm{m}$. The saturation density n_{s} is the maximum density that can be reached when every molecule is ionized. The laser pulse length was assumed to be equal to 70 fs in our simulations. At the entrance of the simulation domain the pulse was represented by a Gaussian beam that would focus into a spot of radius $r_{\mathrm{spot}} = 2\,\mu\mathrm{m}$ in free space.

The FDTD code solves equations (1)–(3) numerically and thus simulates linear and nonlinear laser propagation in the medium, plasma generation, ionizational and collisional energy losses as well as laser interaction with the plasma free particles. The accuracy of the simulations is limited by the uncertainties in some of the parameters involved. The third-order susceptibility, $\chi^{(3)}$, of pure PMMA is relatively well known and is estimated to be

3×10^{-14} esu [58]. However, σ_3 in PMMA is not well known. We assume that it is comparable to other materials with three-photon resonance and therefore replaces the value of σ_3 in PMMA with that of borosilicate glass (the bandgap of borosilicate glass is ~4 eV, while that of PMMA is ~3.7 eV), $\sigma_3 \approx 7 \times 10^{17}$ cm^3 ps^{-1} (cm^2 TW^{-1})^3 [40]. However, it is important to note that an order of magnitude change in σ_3 does not significantly affect the results.

Another source of uncertainty is the damping factor Γ in equation (2). This factor, which represents the laser energy deposition in the collisional plasma caused by the inverse bremmstrahlung heating, is of the order of collision frequency ν_e of the plasma electrons and can be estimated using the Spitzer formula [56]

$$\nu_e\,[\mathrm{s}^{-1}] = 2.9 \times 10^{-6} n\,[\mathrm{cm}^{-3}] \lambda\,[\mathrm{cm}]\, T_e^{-3/2}\,[\mathrm{eV}]. \tag{4}$$

Since the interaction process is non-equilibrium, the electron temperature T_e can be estimated to only an order of magnitude. The electrons excited into the conduction band after absorbing three photons (~4.6 eV) will have a kinetic energy of the order of ~1 eV. This energy is much larger than the Fermi energy, estimated to be ~0.15 eV for a plasma with $n = n_{cr}$. Therefore, one can use a classical approach to estimating the temperature, which thus will be of the order of the quiver energy of the free electron in the oscillating laser field (~10 eV at an intensity of ~10^{14} W cm^{-2}). $n = n_{cr}$ is used to evaluate equation (4), resulting in the collision frequency $\nu_e \approx 0.1$ fs^{-1}, which is used in our simulations. A similar value for collision frequency can be obtained using models for strongly coupled plasmas [59]. The rationale for choosing $n = n_{cr}$ is as follows. When the plasma density is overcritical the laser is reflected back without depositing much energy in the plasma irrespective of the collision frequency. For undercritical plasma the modification patterns were found to be insensitive to Γ [19]. Therefore it is anticipated that the interaction physics is most sensitive to the particular value of electron collision frequency when the plasma density is near-critical or slightly overcritical.

The electron temperature T_e can also be estimated using a quantum mechanical approach, instead of classical. A similar value of $T_e = 12$ eV was obtained for dielectric breakdown in fused silica [60]. The choice of T_e was found in our calculations to not have any substantial influence on the shape of the ablation spot in the range of 3–30 eV. However, if T_e is too small (<1 eV) the asymmetry in the spot disappears, whereas for higher temperatures the asymmetry becomes more prominent.

The accuracy of the simulation is also limited by the fact that we use a fixed value for $\chi^{(1)}$ of the sample while in reality it varies during the entire interaction process. The refractive index of the sample is time dependent due to depletion of bound electrons and can decrease as more electrons are removed into the conduction band by the ultrashort laser pulse. It is therefore reasonable to choose a linear index of refraction that is slightly smaller ($n_0 = 1.3$) than the actual unperturbed value of ~1.5. However, the refractive index modification due to the presence of free electrons is fully taken into account by the plasma current $\vec{J}_P$ that contributes to $\vec{J}$ in equation (1).

We also assume that the energy transfer from electrons to the lattice, which occurs on a much longer time scale compared to the duration of the laser pulse, is localized and coincides with the shape of the plasma. This is justified by the fact that (i) recent calculations [57] demonstrate that there is no difference between damage criteria when either the free electron density or the internal lattice energy is considered. (ii) Even energetic electrons (10 eV) travel a distance of only a fraction of the spot size within the recombination time or even longer.

For this reason, an asymmetry in the plasma profile, if any, will translate into an asymmetry in the ablated spot.

In addition, there are other approximations made in the model given by equations (1)–(3). Firstly, we neglect the higher-order nonlinearities that can be important for intense laser interactions. Secondly, we consider susceptibilities $\chi^{(1)}$ and $\chi^{(3)}$ and the ionization cross-section σ_3 to be frequency independent. We also neglect processes such as avalanche ionization. Furthermore, we assume that the damping factor Γ in equation (2) is a constant, whereas it actually depends on the plasma density and temperature, which in turn depends on the overall interaction dynamics. Therefore, the results presented below are expected to only provide qualitative agreement with the experiments.

3.2. Characterization of the ablation crater

We now demonstrate that polarization-dependent ablation of PMMA arises due to the interaction of the laser pulse with the plasma produced by the leading edge of the pulse. Such a light–plasma interaction leads to local field enhancements either parallel or perpendicular to the laser polarization depending on the plasma density.

Figure 6(a) shows the maximum plasma particle density in units of critical density as a function of the position of the laser focus in the PMMA sample. The plasma density is maximum and is overcritical on the surface and decreases rapidly to below the critical value as the laser focus is moved inside the sample by more than a Rayleigh length ($\sim$16 μm for a focal spot radius of 2 μm used in the calculation). When the laser is focused deep inside the bulk PMMA, the incident pulse undergoes defocusing by the plasma generated by the leading edge of the pulse [19]. As a result, the intensity of the laser pulse at the focus is clamped that results in the generation of undercritical plasma [19, 61]. As the laser focus is shifted closer to the surface, the volume of the undercritical plasma generated by the pulse leading edge is decreased, thus decreasing the plasma negative lens effect.

A typical plasma particle density profile of the laser-generated plasma in the polarization plane is shown in figure 6(b). When the laser is focused right at the sample surface, there is a very thin shell of overcritical plasma at the sample surface that is surrounded by undercritical plasma of a relatively large volume with a diverging shape. This diverging shape is the result of a laser defocusing by the negative plasma lens that surrounds the overcritical disc. The undercritical plasma right behind the disc is created by the leading edge of the laser pulse. When the plasma is undercritical ($n \sim 0.5 n_{cr}$), it leads to refractive index modification [62]. So the actual plasma density value that is required for the ablation must lie somewhere in the critical range.

The plasma particle density profile at the sample surface perpendicular to the direction of laser propagation is shown in figure 6(c). One can clearly see elongation of the overcritical plasma along the polarization direction in the central region of the laser focus. The overcritical plasma electrons oscillate in phase with the laser field, leading to field enhancement at the edges of the plasma in the direction of laser polarization, akin to metal nanoparticles. Faster plasma growth in regions with enhanced fields results in elongation along the polarization direction. In the undercritical plasma regions, elongation is, in contrast, in the direction perpendicular to laser polarization. Electrons in the undercritical plasma oscillate out of phase with the laser, resulting in suppression of the field at the plasma edge in the direction of polarization. In this case, the fields are enhanced all along the plane perpendicular to the laser polarization. Signatures

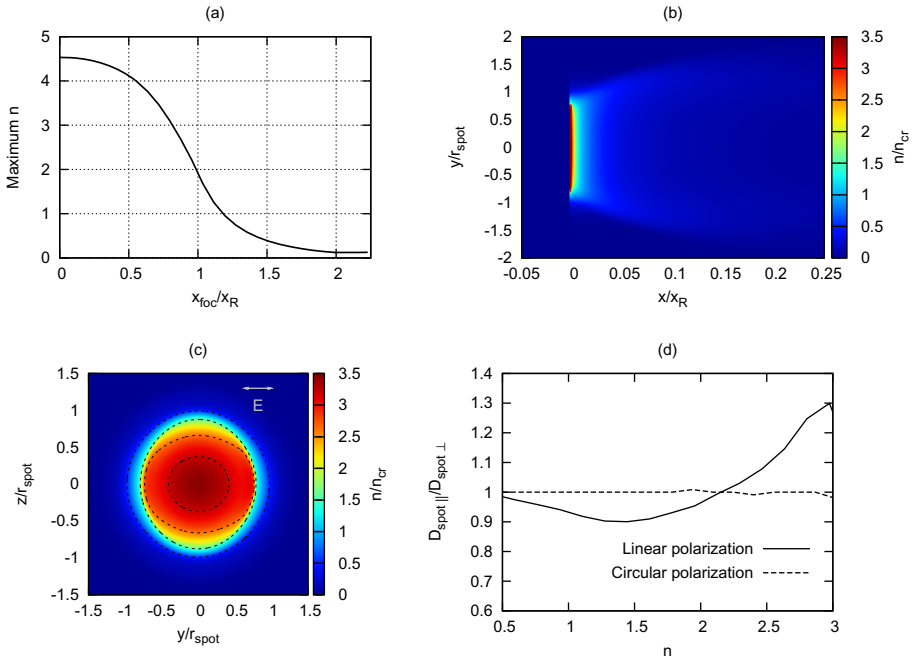

Figure 6. Results of numerical simulations for an incident pulse of intensity $10^{14}\,\mathrm{W\,cm^{-2}}$ interacting with a PMMA sample. (a) Maximum plasma electron particle density on the laser axis (in units of critical density) as a function of geometrical position of the laser focus in units of the Rayleigh length ($\sim$16 μm). (b) Plasma density profile in the polarization plane passing through the laser axis. The surface is located at $x = 0$. The abscissa is in units of Rayleigh length and the ordinate is in units of spot radius. (c) Plasma density profile at the surface of the sample. The distances are in units of spot radius. (d) Quantitative characterization of the spot elongation along the polarization versus plasma density in units of critical density for linear (solid line) and circular (dashed line) laser polarizations.

of such polarization dependence have been observed in the laser interaction inside bulk fused silica where the plasma is undercritical [17–19].

The plasma edge (transition from overcritical to undercritical plasma) is smooth since the transverse shape of the ablation spot is approximately Gaussian (with a size $\sim\sqrt{3}$ times smaller than the laser beam size, for the three-photon ionization process). For this reason, the ablation process is characterized by the two competing effects: (i) field suppression in the polarization direction at locations where the plasma is undercritical, i.e. at distances far from the centre of the laser focus (figure 6(c)); and (ii) field enhancement in the polarization direction at positions where the plasma is overcritical, i.e. close to the centre of the laser focus. The exact shape of the ablation crater is determined by these competing effects, as well as the minimum plasma density that is required for the onset of the actual ablation process.

Quantitative characterization of the elongation of the ablation spot can be made by determining the boundary of the spot for a specified plasma density. Figure 6(d) shows the

ratio of the ablation spot along two orthogonal directions as a function of the plasma density for linear (solid line) and circular polarizations (dashed line). A ratio of unity corresponds to a circular ablation spot with no elongation. For linearly polarized light, the elongation is parallel (perpendicular) to the laser polarization when plasma density $n \gtrsim 2\,n_{cr}$ (or otherwise). Since in a collision-dominated, plasma, reflectivity approaches unity only when its density is well above the critical density, this value seems reasonable. When plasma density is very low ($n \lesssim 0.5 n_{cr}$), field enhancement is negligible and one does not expect any elongation.

Comparing figure 6(d) with figure 3, one can conclude that the plasma density corresponding to the ablation threshold is of the order of $n \sim 2\,n_{cr}$. The dependence of elongation on plasma density is then in agreement with experimental observations (figure 3): (i) no elongation close to threshold pulse energies and (ii) larger asymmetry of the ablation craters for higher pulse energies (corresponding to a plasma density well above the critical density). Moreover, there is no elongation of the ablation spot for circularly polarized light irrespective of the plasma density, as observed in the experiments. Given the approximate nature of our model, a maximum of $\sim$30% elongation for linearly polarized light is in good agreement with the experimental value of $\sim$40%.

The simulations also indicate that the energy deposited in the region with an undercritical plasma (figure 6(b)) is of the order of ten to a few tens of per cent of pulse energy. The energy deposition mechanisms include multiphoton absorption and collisional energy absorption inside the plasma. As the plasma recombines (which happens on the ps time scale compared to the ns time scale of hydrodynamic processes [63]), this energy is converted into heat. Considering that the heat capacity of PMMA is in the range of $\sim 1\,\mathrm{J\,(g\,K)^{-1}}$ [64], an order-of-magnitude estimation shows that deposition of $\sim 1\,\mu$J of laser energy in $\sim 10^3\,\mu\mathrm{m}^3$ (estimated from figure 6(b)) is sufficient to heat up the PMMA inside this volume by $\sim 10^3$ K, i.e. above its boiling point ($\sim$200 °C). We conclude that it is this localized boiling that has resulted in the porous structures observed in the experiment.

Another possible mechanism that can give rise to porosity could be multiple filamentation of the incident pulse while propagating through the medium that leads to severe localization of the pulse energy. Although our simulations rule out this possibility for pure PMMA, we found that this mechanism can occur in highly nonlinear media. For example, the third-order susceptibility $\chi^{(3)}$ in PMMA can be enhanced significantly by doping [58]. When a high value of $\chi^{(3)}$ ($= 3 \times 10^{-12}$ esu) is used in the simulation sub-surface, multiple filamentation is observed for laser intensities above the ablation threshold, as shown in figure 7, where the plasma density profiles (in units of n_{cr}) at time moments well after the laser passage are plotted.

Figure 7(b) shows the plasma density inside doped PMMA in the plane perpendicular to the laser polarization for the peak laser intensity $I = 10^{13}\,\mathrm{W\,cm^{-2}}$. Upon entering the medium, the pulse is immediately self-focused. Due to the very large nonlinearity, the self-focused pulse eventually experiences filamentation. The laser intensity inside the individual filaments reaches considerably high values leading to the material ionization along the filaments. However, the maximum surface plasma density in this simulation is $n_{max} \approx 0.07 n_{cr}$, which is not expected to appreciably damage the surface of the material [62]. At later time scales, hydrodynamic expansion of the hot material under the surface will lead to swelling of the surface similarly to that observed in figures 2(a) and (b).

As the incident laser intensity is increased, the plasma density at the surface grows and reaches values of several n_{cr} for intensities $I \sim 10^{14}\,\mathrm{W\,cm^{-2}}$. For this high plasma density, the material ablates directly from the surface. However, the leading part of the laser pulse that

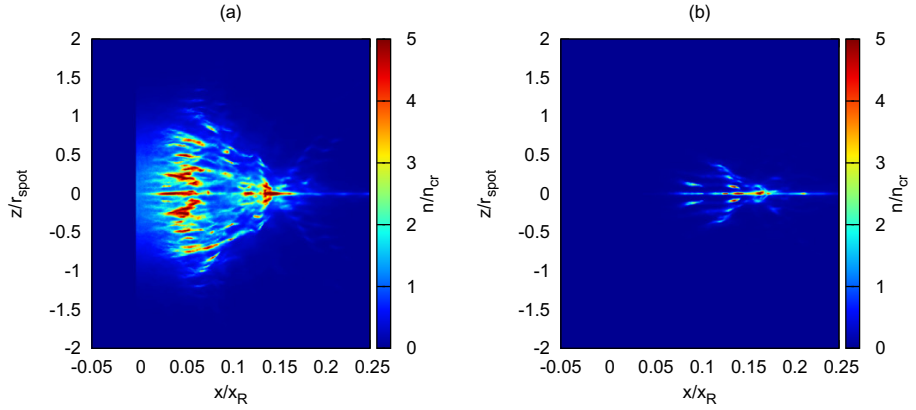

Figure 7. Simulation of the ablation process in doped PMMA. Plasma density generated inside the material when the laser pulse that is focused on the surface of PMMA located at origin propagates in the $+\hat{x}$-direction and is polarized along the $\hat{y}$-direction. The abscissa is in units of Rayleigh length, while the ordinate is in units of spot radius. (a) The laser intensity is above the ablation threshold ($10^{14}\,\mathrm{W\,cm^{-2}}$); (b) the laser intensity is below the ablation threshold ($10^{13}\,\mathrm{W\,cm^{-2}}$). The material surface is located at $x = 0$. The plasma density is measured in units of n_{cr}.

has not been reflected by the surface plasma propagates inside the material and experiences filamentation in the same way as described above. This produces a rich internal structure of the under-surface plasma (figure 7(a)) that can lead to induced porosity. The intensity within the filaments can be high enough that the plasma density can be overcritical. This severe localization of laser energy within the focal volume leads to nano-explosions ejecting out of the material. At the same time, material is removed from the surface, resulting in the material becoming porous. Whereas explosive boiling is the origin of porosity in pure PMMA, in doped PMMA a sub-surface localization of pulse energy in the form of multiple filaments could also give rise to porosity in addition to the causative factor of hydrodynamic expansion that leads to explosive boiling. Since filamentation is a propagation effect, the pores would originate deep Q4 inside the sample as compared to the hydrodynamics process that is restricted to the sub-surface. Analyzing the ablated region along the propagation direction may allow one to distinguish the two mechanisms.

4. Conclusions

In this paper, we show that femtosecond laser ablation of PMMA is polarization dependent in the form of elongated craters (for a stationary focus) and quasi-periodic structures (for line ablation) parallel to laser polarization. Simulations show that elongation of ablation craters can be attributed to a field enhancement during the interaction of an intense light pulse with the overcritical transient plasma produced by the pulse's leading edge. The present work on polarization-dependent ablation (single pulse regime) combined with our previous work on laser-induced periodic structures in fused silica [17] (in the multiple pulse regime) provides

insights into the crucial role played by transient plasmas in the interaction of intense ultrashort light pulses with dielectric materials. Light–plasma interaction influences the energy coupling to the solid by redistributing the local fields in the focal region with respect to the direction of polarization of the incident laser field. Local field enhancement is determined by the plasma density and its signatures are embedded in the interaction region. This effect is not unique to a specific material and would occur whenever there is sufficient nonlinearity in the intensity dependence of the ionization process in order for the field enhancements to produce a noticeable effect in the dielectric. We therefore expect that light–plasma effects will play a less significant role for longer pulse durations, where collisional ionization becomes the dominant process [21]. Polarization-dependent ablation will have an impact on micro-machining, and its effects can be minimized by using either pulse energies close to ablation threshold or circularly polarized light.

Acknowledgments

The authors acknowledge Robert Boyd, Paul Corkum and Thomas Brabec for fruitful discussions and the Natural Science and Engineering Research Council, Canadian Foundation for Innovation and the Ontario Ministry of Economic Development and Innovation for financial support.

References

Q5

[1] Seideman T 1995 *J. Chem. Phys.* **103** 7887
Staplefeldt H and Seideman T 2003 *Rev. Mod. Phys.* **75** 543
[2] Friedrich B and Herschbach D 1995 *Phys. Rev. Lett.* **74** 4623
[3] Larsen J J *et al* 2000 *Phys. Rev. Lett.* **85** 2470
Bisgaard C Z *et al* 2004 *Phys. Rev. Lett.* **92** 173004
[4] Niikura H *et al* 2002 *Nature* **417** 917–22
[5] Baker S *et al* 2006 *Science* **312** 424–7
[6] Corkum P B and Krausz F 2007 *Nature Phys.* **3** 381
[7] Krüger M, Schenk M and Hommelhoff P 2011 *Nature* **475** 78
[8] Davis K M *et al* 1996 *Opt. Lett.* **21** 1729
[9] Chan J W, Huser T, Risbud S and Krol D M 2001 *Opt. Lett.* **26** 1726
[10] Gertsvolf M *et al* 2008 *Phys. Rev. Lett.* **101** 243001
[11] Litvinyuk I V *et al* 2003 *Phys. Rev. Lett.* **90** 233003
[12] Pavicic D *et al* 2007 *Phys. Rev. Lett.* **98** 243001
[13] Pearlman J S, Thomson J J and Max C E 1977 *Phys. Rev. Lett.* **38** 1397
[14] Dinger R, Rohr K and Weber H 1987 *Laser Part. Beams* **5** 691
[15] Tanabe K 2008 *J. Phys. Chem.* C **112** 15721
[16] Shimotsuma Y *et al* 2003 *Phys. Rev. Lett.* **91** 247405
[17] Bhardwaj V R, Simova E, Rajeev P P, Hnatovsky C, Taylor R S, Rayner D M and Corkum P B 2006 *Phys. Rev. Lett.* **96** 057404
[18] Rajeev P P *et al* 2007 *J. Phys. B: At. Mol. Opt. Phys.* **40** S273
[19] Popov K I, McElcheran C, Briggs K, Mack S and Ramunno L 2011 *Opt. Express* **19** 271
[20] Taylor R S *et al* 2007 *Opt. Lett.* **32** 2888
[21] Hnatovsky C *et al* 2005 *Appl. Phys. Lett.* **87** 014104
[22] Hnatovsky C *et al* 2006 *Appl. Phys.* A **84** 47
[23] Taylor R S, Simova E and Hnatovsky C 2008 *Opt. Lett.* **33** 1312

[24] Hnatovsky C, Shvedov V, Krolikowski W and Rode A 2011 *Phys. Rev. Lett.* **106** 123901
[25] Birnbaum M 1965 *J. Appl. Phys.* **36** 3688
[26] Young J F, Sipe J E and van Driel H M 1984 *Phys. Rev.* B **30** 2001
Young J F, Sipe J E and van Driel H M 1983 *Opt. Lett.* **8** 431
[27] Guosheng Z, Fauchet P M and Siegman A E 1982 *Phys. Rev.* B **26** 5366
[28] Preston J S, Van Driel H M and Sipe J E 1989 *Phys. Rev.* B **40** 3942
[29] Varel H, Wahmer M, Rosenfeld A, Ashkenasi D and Campbell E E B 1998 *Appl. Surf. Sci.* **127–129** 128
[30] Ozkan A M, Malshe A P, Railkar T A, Brown W D, Shirk M D and Molian P A 1999 *Appl. Phys. Lett.* **75** 3716
[31] Yasumaru N, Miyazaki K and Kiuchi J 2002 *Appl. Phys.* A **76** 983
[32] Bonse J, Baudach S, Krüger J, Kautek W and Lenzner M 2002 *Appl. Phys.* A **74** 19
[33] Borowiec A and Haugen H K 2003 *Appl. Phys. Lett.* **82** 4462
[34] Bolle M and Lazare S 1993 *Appl. Surf. Sci.* **65/66** 349
[35] Young J, Preston J, van Driel H and Sipe J 1983 *Phys. Rev.* B **27** 1155
[36] Huang M, Zhao F L, Cheng Y, Xu N S and Xu Z Z 2009 *ACS Nano* **3** 4062
[37] Han Y, Zhao X and Qu S 2011 *Opt. Express* **19** 19150
[38] Baudach S, Bonse J and Kautek W 1999 *Appl. Phys.* A **69** S395
[39] Venkatakrishnan K, Tan B, Stanley P and Sivakumar N R 2002 *J. Appl. Phys.* **92** 1604
[40] Kruger J and Kautek W 2004 *Adv. Polym. Sci.* **168** 247
[41] Miotello A and Kelly R 1995 *Appl. Phys. Lett.* **67** 3535
Miotello A and Kelly R 1999 *Phys. Rev.* E **60** 2616
[42] Zhigilei L V *et al* 2003 *Chem. Rev.* **103** 321
[43] Craciun V *et al* 2002 *Appl. Surf. Sci.* **186** 288
[44] Haglund R F Jr and Ermer D R 2000 *Appl. Surf. Sci.* **168** 258
[45] Perez D and Lewis L J 2002 *Phys. Rev. Lett.* **89** 255504
Perez D and Lewis L J 2003 *Phys. Rev.* B **67** 184102
[46] Lorazo P, Lewis L J and Meunier M 2003 *Phys. Rev. Lett.* **91** 225502
[47] Sokolowski-Tinten K *et al* 1998 *Phys. Rev. Lett.* **81** 224
[48] Anisimov S I *et al* 1999 *Appl. Phys.* A **69** 617
[49] Zhakhovski V V, Nishihara K, Anisimov S I and Inogamov N A 2000 *JETP Lett.* **71** 167
[50] Agranat M B *et al* 2007 *Appl. Surf. Sci.* **253** 6276
[51] Savolainen J-M, Christensen M S and Balling P 2011 *Phys. Rev.* B **84** 193410
[52] Baudach S, Bonse J, Kruger J and Kautek W 2000 *Appl. Surf. Sci* **154–155** 555
[53] Rajeev P P *et al* 2006 *Phys. Rev. Lett.* **97** 253001
[54] Mulser P, Cornolti F and Bauer D 1998 *Phys. Plasmas* **5** 4466
[55] Peñano J R, Sprangle P, Hafizi B, Manheimer W and Zigler A 2005 *Phys. Rev.* E **72** 036412
[56] NRL Plasma Formulary (Revised 2004) p 34 Q6
[57] Rethfeld B *et al* 2010 *Appl. Phys.* A **101** 19
[58] D'Amore F, Lanata M, Pietralunga S M, Gallazzi M C and Zerbi G 2004 *Opt. Mater.* **24** 661–5
[59] Cauble R and Rozmus W 1985 *Phys. Fluids* **28** 3387
[60] Kaiser A, Rethfeld B, Vicanek M and Simon G 2000 *Phys. Rev.* B **61** 11437
[61] Rayner D M, Naumov A and Corkum P 2005 *Opt. Express* **13** 3208
[62] Sudrie L *et al* 2002 *Phys. Rev. Lett.* **89** 186601
[63] Mézel C, Hallo L, Bourgeade A, Hébert D, Tikhonchuk V T, Chimier B, Nkonga B, Schurtz G and Travaillé G 2008 *Phys. Plasmas* **15** 093504
[64] Soldera A, Metatla N, Beaudoin A, Said S and Grohens Y 2010 *Polymer* **51** 2106–11

Chapter 5

Multiple pulse studies in PMMA

5.1 Introduction

This chapter is based on a previously published paper, and another manuscript is in process of publication. The work reported addresses some fundamental aspects of the ablation process due to multiple pulse effect. In section 5.2 we investigated morphological changes to the surface of bulk dielectric irradiated by two femtosecond pulses at a certain delay. We studied this as a function of pulse energy. Our experimental results demonstrated the first ever experimental evidence of nano-pillar formation within the ablation crater. With increasing fluence, the nano-pillar vanished and the structure within the ablation crater resembled with the splash of object in liquid. A 2 dimensional (2D) Molecular Dynamics (MD) model was used to predict the mechanism for nano-pillar formation by double pulse irradiation. This model (MD) rendered the fact that, the presence of the first laser pulse is compulsory since it defines the boundaries from which the shock wave induced by second laser pulse reflects and causes density pinching in the middle of the interaction region that rapidly pushes out the molten material towards the surface. The results from numerical simulations agreed well with experimental results presented in this thesis.

In section 5.3 we carried out the systematic study of the evolution of porosity within the ablation craters as a function of laser fluence and number of laser shots. Multiple pulse irradiations of femtosecond pulses on bulk PMMA surface erased the polarization-dependent elongation of the ablation craters and yielded micro- and nano-scale porosity within the ablation crater. Analysis of SEM images revealed the dependence of porous area fraction and the pore size distribution as a function of pulse energy when the laser

focus is stationary. Using imaging technique, we demonstrated that the porous area fraction decreases with pulse energy while the pore size distribution peaks at a pore area of 0.037 μm^2 at higher energies. Also, the dependence of porous area fraction as a function of scanning speed and laser pulse energy was investigated when the laser focus was moved with a specific speed (in line ablation regime). These micro- and nanoscale porous structures hold significant prospect to promote cell adhesion and proliferation at the polymer-tissue interface for better implant union.

5.2 Nano-pillar formation by two-pulse femtosecond laser ablation in poly-methyl methacrylate (Publication 3)

F. Baset, K. Popov, A. B. Villafranca, A. M. Alshehri, J-M Guay,
L. Ramunno and V. R. Bhardwaj
Nano-pillar formation by two-pulse femtosecond laser ablation in poly-methyl methacrylate
In preparation (2014)

5.2.1 Author contribution

The section demonstrates results from experiments performed by F. Baset, J-M Guay and V. R. Bhardwaj at Ultrafast Photonics lab, University of Ottawa, ON. F. Baset and J-M Guay performed preliminary (unpublished data) and final experiments under supervision of V. R. Bhardwaj. F. Baset and A. B. Villafranca conducted the analysis of the results and F. Baset created the figures. Theoretical simulation had been performed by K. Popov and L. Ramunno. At present, this manuscript is in process of publication. F. Baset wrote the first draft of the manuscript. All authors contributed to the final manuscript.

Nano-pillar formation by two-pulse femtosecond laser ablation of poly-methyl methacrylate

F. Baset,[1] K. Popov,[1] A. B. Villafranca,[1] A. M. Alshehri,[1] J-M. Guay,[1] L. Ramunno,[1] and V. R. Bhardwaj[1, a)]
Department of Physics, University of Ottawa, 150 Louis-Pasteur, Ottawa, Ontario, K1N 6N5, Canada

(Dated: 15 November 2013)

A nano-pillar is formed within the ablation crater in bulk poly-methyl methacrylate when irradiated with a pair of femtosecond light pulses. For pulse energies below single-shot ablation threshold the nano-pillar is ∼400nm long and protrudes ∼150nm above the surface. At higher energies, the nano-pillar is replaced by a volcanic eruption like structure. Molecular dynamics simulations reveal that the nano-pillar is formed when the shockwave induced by the second laser pulse is reflected from the cold boundaries defined by the first laser pulse. Reflection causes density pinching in the interaction region that rapidly pushes out the molten material towards the surface.

PACS numbers: 79.20.Eb, 02.70.Ns, 79.20.Ds, 81.16.Rf

Behaviour of condensed matter under extreme conditions has significant interest in astrophysics, geophysics and material science as it enables to explore new phases and forms of electronic and ionic order[1,2]. Shock compression studies involving diamond anvil cells, explosives and high-speed projectiles have been employed to evaluate the shocked state of matter using different spectroscopic methods[3]. Irradiation of matter with intense light pulses is another technique that not only produces extreme conditions, albeit on micron scale, but also provides access to time scales shorter than characteristic durations. A high-pressure and high-temperature plasma is generated instantaneously when laser pulses are focused on the surface (inside the bulk) resulting in material ablation (modification). The expanding plasma can induce shockwaves that propagate through the material[4].

For the past two decades, ultrafast laser ablation of materials has been investigated to gain mechanistic insights into the interaction of light with dense media and for its wide ranging applications. Several studies have focused on propagation of shockwaves in different materials[4–6] and on morphological changes to the surface irradiated with single and multiple pulses. In laser processing of materials with multiple pulses, changes induced by the first pulse affects the material response to subsequent pulses. As a result, ablation thresholds have been found to decrease with the number of laser pulses due to the incubation effects[7,8]. The material response and hence the ablation process is also influenced by the delay between the pulses. Double pulse ablation of metals and fused silica have shown a decrease in the ablation depth with increasing delay between the pulses[9,10].

The morphology of laser ablated regions also reveal rich structure formation on micro- and nanoscale. Multi-pulse irradiation resulted in formation of nanogratings/ripples[11–17] and nanocones/spikes within the ablated region[18–22] of different materials. Nanobumps and nanojets that have undergone resolidificiation were produced on thin metal films by single femtosecond laser pulse[23–25] and were attributed to relaxation of laser-induced stresses inside the molten target followed by fast resolidification[26,27]. Nanojet formation and subsequent ejection of nanodroplets is also widely seen to be the mechanism behind laser-induced forward transfer (LIFT) technique used for nano-patterning[28,29].

Re-solidified nanojet structure in the form of a nanopillar has never been observed in bulk materials. In this letter, we report nano-pillar formation adjacent to a nanopore within the ablation crater in bulk polymethyl methacrylate(PMMA) irradiated by two femtosecond pulses . The two pulses are separated in time by 100's of ms, long enough for any changes induced by the first laser pulse to resolidify. We show that the nanopillar is formed only for specific pulse energies beyond which it disappears and a larger nanopore appears in the middle of the ablation crater encircled by a volcanic eruption like structure. We model the interaction of femtosecond pulses with PMMA using molecular dynamics approach and show that a resolidified nanopillar is formed when a shockwave, induced by the second laser pulse in the molten material, undergoes a reflection at the cold boundaries and pinches the material density in the middle and pushes it out rapidly towards the surface.

800nm light from a Ti:Sapphire laser system operating at a repetition rate of 5 kHz and producing 45 fs pulses with a peak energy of 0.5 mJ, was focused on the surface of optically polished PMMA samples (12×12×2 mm) by a 0.25 NA microscope objective. The PMMA sample was irradiated with a pair of femtosecond pulses selected by operating the laser in an external trigger mode. The delay between the pulses varied from 100's of ms to few seconds.The incident pulse energies were measured after the microscope objective and monitored by a calibrated fast photodiode. The position of the laser focus relative to the sample surface was accurately determined by imaging the back reflected light with a CCD camera at pulse energies much below the ablation threshold. A single-shot au-

a)Corresponding author: [redacted]@uottawa.ca

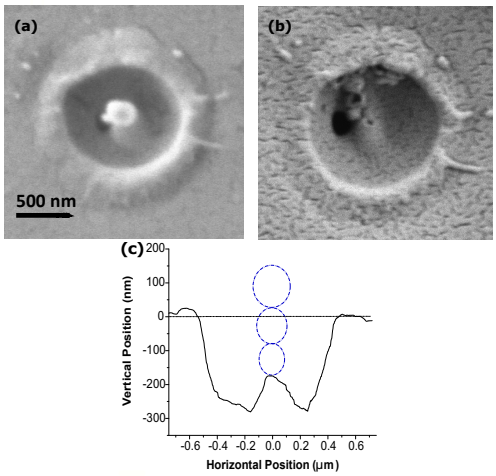

FIG. 1. SEM image of the 2-pulse ablation crater formed by a 580 nJ femtosecond pulse (a) before, and (b) after breaking the nano-pillar in the middle with an AFM tip. (c) AFM line scan of the crater along with the reconstructed nano-pillar.

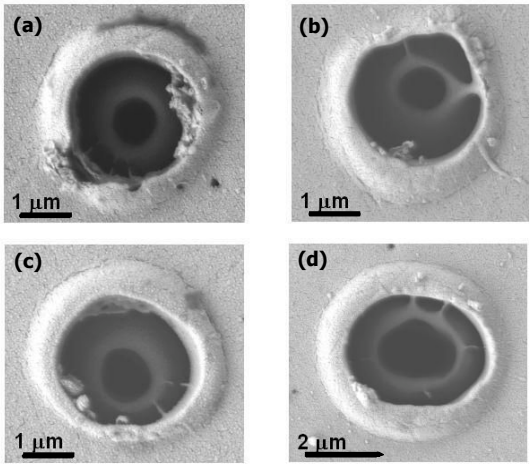

FIG. 2. SEM images of 2-pulse ablation craters in PMMA irradiated with pulse energies of (a) 800 nJ, (b) 870 nJ, (c) 940 nJ and (d) 1100 nJ.

tocorrelator continuously monitored the pulse duration. The pulses were not pre-chirped and the duration was measured to be 70 fs at the back aperture of the objective. The laser-ablated regions were characterized by an atomic force microscope operating in contact mode with a pyramidal cantilever (lateral resolution of ∼30nm) and by a scanning electron microscope (SEM) after gold coating the PMMA surface with a thin layer (few nanometers) to make them conductive. All SEM images were taken with the electron beam perpendicular to the sample (zero tilt). The laser focal spot radius of $2.7\pm0.2\mu$m was obtained from the slope of semi-logarithmic plot of the squared diameter of the modified region measured with the SEM as a function of pulse energy.

Figure 1(a) shows SEM image of an ablation crater produced by 2 laser pulses with a delay of milliseconds. Pulse energy was 580 nJ, lower than the single-shot ablation threshold of 600 nJ (laser fluence of 2.6J/cm^2)[7] but higher than the double-shot ablation threshold of 350 nJ[7]. The ablated region has an annular rim with a nanopillar like structure in the middle adjacent to a nanopore. Radial ejection pattern at the edges suggests melting and resolidification. The nanopillar is brighter in the image suggesting it protrudes above the surface. Figure 1(b) shows SEM image of the same crater after the pillar like structure is broken by an AFM pyramidical cantilever tip (spring constant of 69 ± 1 pN/nm). The image reveals that the pillar like structure is composed of three ellipsoids stacked on top of each other. Presence of a 165 nm pore suggests ejection of molten material in the form of a nanojet that has resolidifed upon rapid expansion. Figure 1(c) shows line scan of the ablation crater with reconstructed nano-pillar that is ∼400nm long and protrudes ∼150nm above the sample surface. Time delays greater than ms between the two pulses did not effect nanopillar formation.

Figure 2 shows evolution of structure within the ablated region for different pulse energies. When pulse energy is above the single-shot ablation threshold the nanopillar disappears and only a central pore is formed. The pore size increases with pulse energy until 700 nJ. Beyond this energy the ablation crater begins to display a volcanic eruption like structure in the middle as shown in Fig. 2. The size of the ablation crater and the central pore increases with energy. Also, the central structure resembling a splash of molten material becomes prominent. Nanostructures shown in Fig. 1 and 2 appear only in 2-pulse laser ablation. Single-shot ablation of PMMA only leads to surface swelling and crater formation[30].

To understand the origin of nano-pillar formation, interaction of femtosecond laser pulses with PMMA is modelled using molecular dynamics (MD) approach. Since this approach is computationally intensive simulations are often restricted to small volumes on the order of few 100's of nm and few hundred thousand particles[31], effectively ignoring the spatial profile of the laser. We overcome this by conducting the computation in 2D with simulation dimensions on the order of the laser spot size. We use $\sim 4\times10^7$ particles on a 2D hexagonal lattice occupying an area of $\sim 2\times2\,\mu$m.

The interaction between individual atoms is described by Lennard-Jones potential with characteristic length and depth represented by σ and ε_0 respectively. For a wide range of molecules, $\varepsilon_0 \approx 10$ - 100meV and $\sigma \approx 0.25$ - 0.6 nm[32]. The parameters we chose were $\sigma = 0.3$ nm, $\varepsilon_0 = 0.0862$ eV and time normalization factor $t_0 = 0.4$ ps[33]. These values are close to that of water and provide an estimate of physical quantities such as temperature, particle velocities and densities. Their magnitudes depend

weakly on a particular choice of parameters but not the dynamics. As a result, we can only learn qualitative dynamics of the ablation process. Particular details such as elastic properties of polymers due to their chain structure and formation of volatile compounds due to chain breaking are ignored.

First stage of the simulation involves creating an unperturbed equilibrium state at room temperature T_r. The sample, initially at zero temperature, is annealed slowly in the Nose-Hoover thermostat until T_r is reached. In the second stage of simulation, the first laser pulse induces a non-equilibrium configuration, modelled by scaling particle velocities consistent with a temperature profile $T(\vec{r}, 0)$. The particles are then propagated self-consistently by the LAMMPS NVE solver[34]. A thin layer around the edges is maintained at constant temperature to mimic bulk thermal reservoir. When the second laser pulse is incident, the particle velocities are rescaled again according to $T(\vec{r}, 0)$. For computational feasibility we use a delay of 10 ns between the two laser pulses, much smaller than experiments. However, this is long enough for the simulated system to reach a completely frozen state. In our simulations, the second stage dynamics was probed in 1 fs intervals.

$T(\vec{r}, 0)$ is determined by the spatial distribution of energy transferred from the laser beam to the electrons via ionization, $\delta\mathcal{E}_i$, and collisional absorption, $\delta\mathcal{E}_{ca}$. Assuming multi-photon ionization to be the dominant ionization process in the near-threshold region[35] one can write

$$\delta\mathcal{E}_i \propto \left(\frac{I(\vec{r})}{I(\vec{r}_f)}\right)^N, \tag{1}$$

where $I(\vec{r})$ is the spatial profile of the unperturbed laser pulse, $\vec{r}_f$ is the position of the laser best focus and the order of multi-photon absorption, $N = 3$ for PMMA.

The collisional absorption of laser energy by plasma depends not only on the generated plasma density n, but also on the laser intensity. The latter dependence of $\delta\mathcal{E}_{ca}$ is expected to result only in perturbation of the overall laser energy deposition profile in the sample. So, we assume $\delta\mathcal{E}_{ca}$ is similar to Eq. (1) to keep our parameter space small. Therefore the overall temperature profile at the beginning of simulation is assumed to be

$$T(\vec{r}, 0) \approx T_r \cdot \left[1 + \alpha \cdot \left(\frac{I(\vec{r})}{I(\vec{r}_f)}\right)^N\right], \tag{2}$$

where α is a parameter of simulations. Numerically we find $\alpha = 1.2$ corresponds to the single shot ablation threshold. The two-shot ablation threshold is lower by 35-40% compared to 42%, measured experimentally.

Figure 3 shows the dynamics in PMMA after the second laser pulse is incident. Density-weighted particle velocity in y (top panel) and x directions (bottom panel) are shown at two different time steps for α=0.95; this corresponds to a fluence below the single-pulse ablation threshold. Along y-direction, the particle velocities are initially away from the centre of the interaction region.

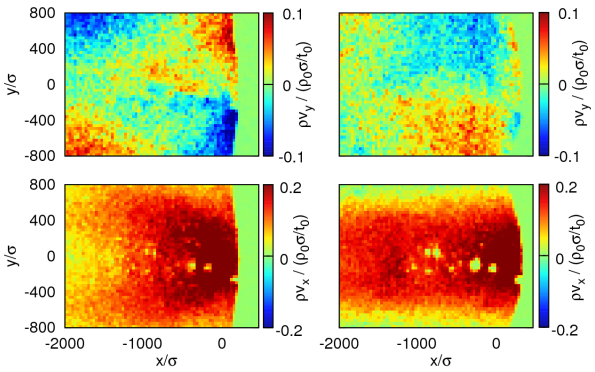

FIG. 3. (Color online) Calculated density weighted particle velocities along y-direction (top panel) and x-direction (bottom panel) at two different times $6\times10^2 t_0 \approx 240$ ps (left column) and $1.1\times10^3 t_0 \approx 440$ ps (right column) for $\alpha = 0.95$. Laser is incident on the sample surface at $x/\sigma = y/\sigma = 0$. $x/\sigma = y/\sigma = 6000$ corresponds to a sample thickness of 2μm. Only the relevant portion of the simulation domain is shown.

Then at a later time, they have changed their direction after reflecting from the boundaries of the interaction region and are moving towards the centre (top right panel). This behaviour is not observed in the absence of the first laser pulse.

Along x-direction, particle velocities are initially very high at the surface (bottom left panel). Small regions of very low particle velocities are formed corresponding to voids. At a later time, high particle velocity leads to surface swelling and more voids are formed (bottom right panel). Also, particle velocities are high in a confined region inside the sample at $x/\sigma \approx 1350$ ($\sim$450nm). This is due to reflection of shockwave from the boundaries (top panel) and ultimately leads to density pinching in the centre. At later times, particles are pushed out towards the surface forming a nanojet. The shock velocity is ≈ 6 km/s, comparable to that measured in PMMA[36].

For higher α, reflection of shockwave from the boundaries and the resultant density pinching becomes stronger. However, due to the 2D nature of our simulations the nanojet formation is not accurately captured at lower α but becomes apparent at higher values as shown in figure 4 for α=1.6. In this case the laser fluence is higher than the single-pulse ablation threshold. As a result the first laser pulse itself leads to significant ablation and the second pulse interacts with the ablated sample.

The top panels of Fig. 4 show density weighted particle velocities in x and y directions at a time step of $50t_o$. Similar to the case for $\alpha = 0.95$, a shockwave propagates away from the interaction region. At the same time, particles close to the surface move inwards due to temperature and pressure gradients. This is a consequence of material removal by the first laser pulse. Along the x-direction particle velocities are high close to the surface.

Middle and bottom left panels of Fig. 4 show evolution

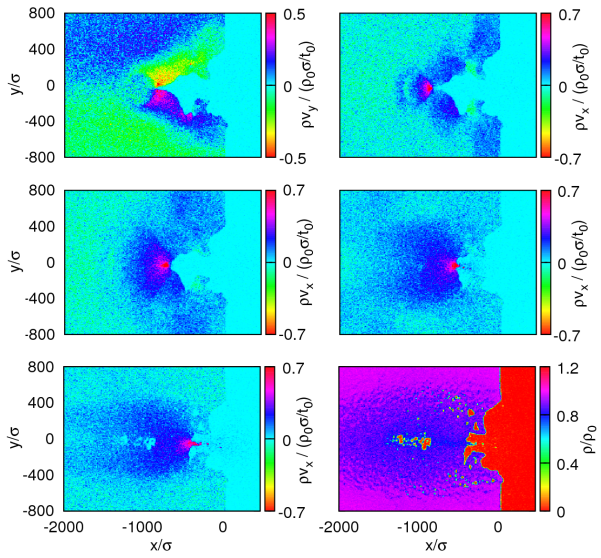

FIG. 4. (Color online) Calculated density weighted particle velocities and normalized particle density for $\alpha = 1.6$. Top panels show particle velocities along y- (left) and x- (right) directions at $50t_0 \approx 20$ ps. Middle panels show evolution of particle velocities along x-direction at two different times $100t_0 \approx 40$ ps (left) and $250t_0 \approx 100$ ps (right). Bottom panels shows particle velocities along x-direction (left) and particle density (right) at $500t_0 \approx 200$ ps. Laser is incident on the sample surface at x/σ= y/σ = 0. x/σ = y/σ = 6000 corresponds to a sample thickness of 2μm. Only the relevant portion of the simulation domain is shown.

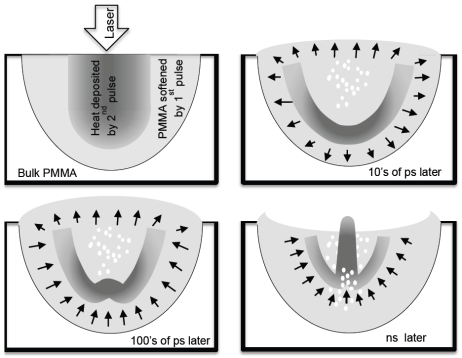

FIG. 5. (Color online) Schematic describing the physics of nano-pillar formation. Arrows indicate the direction of propagation of a pressure wave. See text for details.

of particle velocities along x-direction at different times. They are confined in the middle and move out towards the surface at later times due to collision with particles moving inwards along y-direction. As a result, density is pinched in the middle forming a nanojet as shown in bottom right panel for t = $500t_o$. For $\alpha = 1.6$ the nanojet is not frozen, instead it propagates at later times resulting in formation and ejection of nanodroplets. The resultant structure resembles those shown in Fig.2. However, at lower α we anticipate the nanojet to resolidify due to rapid expansion directed towards the surface. At intensities where there is appreciable ablation by the first laser pulse itself, shape of the ablated region seems to play a dominant role compared to the reflection of shockwave from the boundary defined by the first laser pulse.

The following picture then emerges about nanopillar formation in bulk media, depicted by the schematic in Fig. 5. Interaction of the first pulse, whose energy is below the ablation threshold, with PMMA softens the material with which the second laser pulse interacts. Tens of ps later a shockwave is induced that propagates radially in the sample leading to swelling of unbounded surface and nanopore formation[30]. Hundreds of ps later the shockwave is reflected (part of it dissipates into the sample) from the cold boundaries of the interaction region. Also, nanopores coalesce into voids. Nanoseconds later, the reflected shockwaves collide pinching the softened material and pushes it towards the surface as a nanojet. The ever expanding surface swelling ruptures and large chunks of material and nanodroplets are ejected. Rapid expansion of the nanojet leads to resolidification under appropriate condition. At higher energies, localized eruption of softened material leads to formation of volcanic like structures in the middle encircled by the ruptured dome like structure. The structure formation that we observe is analogous to an object falling into liquids creating a splash (called crown) followed by a jet of liquid ejecting outwards[37,38]. In laser irradiation of bulk polymer, the nanopillar is formed first and is replaced by volcanic eruption like structure (similar to crown) at higher pulse energies.

In conclusion, a nano-pillar is formed in the ablation crater when bulk PMMA is irradiated by two femtosecond pulses. Presence of the first laser pulse is crucial as it defines the boundaries from which the shockwave induced by the second laser pulse reflects. In the absence of the first laser pulse simulations do not show any reflection of the shock wave. This is the key difference between the nano-pillar formation in bulk and in thin metal films. In the latter, a single laser pulse leads to spallation and the subsequent collapse of the bubble underneath results in movement of molten material to the apex of the bump and formation of jets directed in opposite directions. Although the 2D nature of our simulations do not quantitatively reproduce experimental observations they provide an insight into the possible mechanism. Results suggest under appropriate experimental conditions bulk materials can be used, besides thin films, in nano-patterning of substrates with LIFT technique.

ACKNOWLEDGMENTS

The authors gratefully acknowledge financial support from Natural Science and Engineering Research Council of Canada, Canadian Foundation for Innovation and Canada Research Chairs. Computations were performed on Southern Ontario Smart Computing Innovation Platform (SOSCIP) BlueGene/Q supercomputer located at the University of Toronto's SciNet HPC facility.

[1]M.I. Eremets and I.A. Troyan, *Nature Materials* **10**, 927 (2011).
[2]K. Kadau, T. C. Germann, P.S. Lomdahl and B.L. Holian, *Science* **296**, 1681 (2002).
[3]M. Eremets, *High pressure experimental methods*, Oxford University Press, 1996
[4]L. Huang, Y. Yang, Y. Wang, Z Zheng and W. Su, *J. Phys. D: Appl. Phys* **42**, 045502 (2009).
[5]H. Hu, Z. Wang, Nan Zhang, H. Zhai and P. Wang, *Proc. SPIE* **7843**, 78430U-1 (2010).
[6]X. Zeng, X.L. Mao, R. Greif and R.E. Russo, *Appl. Phys. A* **80**, 237(2005).
[7]J-M. Guay, A. B. Villafranca, F. Baset, K. Popov, L. Ramunno and V.R. Bhardwaj, *New J. Phys.* **14**, 085010 (2012).
[8]J. Kruger and W. Kautek, Adv. Polym. Sci. **168**, 247 (2004).
[9]M.E. Povarnitsyn, T.E. Itina, K.V. Khishchenko and P.R. Levashov, Phys. Rev. lett. **103**, 195002 (2009).
[10]T. Donnelly, J.G. Lunney, S. Amoruso, R. Bruzzese, X. Wang and X. Ni, J. Appl. Phys, **106**, 013304 (2009).
[11]A.Y. Vorobyev, V.S. Makin and C. Guo, J. Appl. Phys, **101**, 034903 (2007).
[12]M. Okamuro, M. Hashida, Y. Miyasaka, Y. Ikuta, S. Tokita and S. Sakabe, Phys. Rev. B **82**, 165417 (2010).
[13]J. Bonse, J. Kruger, S. Hohm and A. Rosenfeld, J. Laser App.**24**, 042006 (2012).
[14]A. Borowiec and H.H. Haugen, Appl. Phys.Lett. **82**, 4462 (2003).
[15]J. Bonse A. Rosenfeld and J. Kruger, J. Appl. Phys. **106**, 104910 (2009).
[16]V.R. Bhardwaj, E. Simova, P.P. Rajeev,C. Hnatovsky, R.S. Taylor, D.M. Rayner and P.B. Corkum, Phys. Rev. Lett. **96**, 057404 (2006)
[17]Y. Han , X. Zhao and S. Qu, Opt. Express **19**, 19150 (2011)
[18]M. Shen, C. Crouch, J. Carey, R. Younkin, E. Mazur, Appl. Phys. Lett. **82**, 1715 (2003).
[19]M. Shen, J. Carey, C. Crouch, M. Kandyla, H. Stone and E. Mazur *Nano Letters* **8**, 2087 (2008).
[20]Q.Z. Zhao. F. Ciabanu and L.J. Wang, J. Appl. Phys. **105**, 083103 (2009).
[21]Q.Z. Zhao. S. Malzer and L.J. Wang, Opt. Exp. **15**, 15741 (2007).
[22]B.K. Nayak, M.C. Gupta and K.W. Kolasinski, Nanotechnology **18**, 195302 (2007).
[23]J. Koch, F. Korte, T. Bauer, C. Fallnich, A. Ostendorf and B.N. Chichkov, Appl. Phys. A **81**, 325 (2005).
[24]A. I. Kuznetsov, C. Unger, J. Koch and B.N. Chichkov, Appl. Phys. A **106**, 479 (2012).
[25]J.P. Moening, S.S. Thanawala and D.G. Georgiev, Appl. Phys. A **95**, 635 (2009).
[26]D. Wortmann, J. Koch, M. Reininghaus, C. Unger, C. Hulverscheidt, D. Ivanov and B.N. Chichkov, J. Laser. Appl. **24**, 042017 (2012).
[27]Y.P. Meshcheryakov and N.M. Bulgakova, Appl. phys. A **82**, 363 (2006).
[28]D. Banks, C. Grivas, J. Mills, I. Zergioti and R. Eason, Appl. Phys. Lett. **89**, 193107 (2006).
[29]S. Bera, A. Sabbah, J. Yarbrough, C. Allen, B. Winters C. Durfee and J. Squier, Appl. Opt. **46**, 4650 (2007).
[30]F. Baset, K. Popov, A.B. Villafranca, J-M. Guay, Z. Al-Rekabi, A. Pelling, L. Ramunno and V.R. Bhardwaj, Opt. Exp. **21** 12527 (2013)
[31]D. S. Ivanov, B. Rethfeld, G. M. OConnor, T. J. Glynn, A. N. Volkov, L. V. Zhigilei, Appl Phys A **92**, 791 (2008).
[32]J. Hirschfelder, C.F. Curtiss and R. Bird, *Molecular theory of gases and liquids*, Wiley, New York, (1954).
[33]Time normalization factor $t_0 = \sqrt{m\sigma^2/\varepsilon_0}$, where m is mass of the molecule.
[34]http://lammps.sandia.gov; S. Plimpton, J. Comp. Phys. **117**, 1 (1995).
[35]Perturbation of laser propagation by the generated plasma is assumed to be negligible since the plasma density is well below critical density in the near threshold regime.
[36]S.D. Mcgrane, D.S. Moore and D.J. Funk, J. Appl. Phys. **93**, 5063 (2003).
[37]A. Yarin *Annu. Rev. Fluid Mech.* **38** 159 (2006).
[38]S. Thoroddsen, T. Etoh, K. Takehara *Annu. Rev. Fluid Mech.* **40**, 257 (2008).

5.3 Femtosecond laser induced porosity in poly-methyl methacrylate (Publication 4)

F. Baset, A. B. Villafranca, J-M Guay and V. R. Bhardwaj
Femtosecond laser induced porosity in poly-methyl methacrylate
Applied Surface Science **282**, 729-734 (2013)

5.3.1 Author contribution

The published results come from experiments performed by F. Baset, A. B. Villafranca, J-M Guay and V. R. Bhardwaj at Ultrafast Photonics lab, University of Ottawa, ON. F. Baset and J-M Guay performed preliminary experiments (unpublished data) and F. Baset with A. B. Villafranca conducted the analysis of the results and created the figures. F. Baset wrote the first draft of the manuscript. All authors contributed to the final manuscript.

Applied Surface Science 282 (2013) 729–734

Contents lists available at SciVerse ScienceDirect

Applied Surface Science

journal homepage: www.elsevier.com/locate/apsusc

Femtosecond laser induced porosity in poly-methyl methacrylate

Farhana Baset, Ana Villafranca, Jean-Michel Guay, Ravi Bhardwaj*

Department of Physics, University of Ottawa, 150 Louis Pasteur, Ottawa, ON K1N 6N5, Canada

ARTICLE INFO

Article history:
Received 30 January 2013
Received in revised form 4 June 2013
Accepted 6 June 2013
Available online 18 June 2013

Keywords:
Laser material processing
Surface structuring
Femtosecond phenomena
Nanostructure fabrication

ABSTRACT

We show that femtosecond laser ablation of poly-methyl methacrylate (PMMA) induces porosity within the ablation crater that increases with pulse energy/fluence and number of laser shots. For deeper craters the porosity evolves into 3D honeycomb like structure on the sidewalls. Using imaging technique, we show that the porous area fraction decreases with pulse energy while the pore size distribution peaks at a pore area of 0.037 μm^2 at higher energies. In line ablation, the pore size increases with the speed at which the laser focus is moved.

1. Introduction

Structuring of biocompatible materials through surface modification is of great interest since it enables better implant union in human body by reduced toxicity [1], enhanced binding and integration of tissues and nerves [2]. Surface topography of biomaterials influences biological response. Micro/nano-patterned surfaces can be used to control and manipulate spatial localization of cells and their shape [3] by altering their adhesion to the substrate and thereby regulating the complex cell dynamics [4]. Studies have shown that both disordered (roughness) and ordered (periodic grooves or array of holes) surface structures influence cell growth [5]. Apart from adhesion, surface structuring also drastically alters wetting [6,7], mechanical, electrical and optical properties of materials [8]. For example, control of porosity in TiO_2 enhances its photovoltaic behavior [9].

Surface structuring of biomaterials with nanosecond and picosecond lasers have demonstrated formation of suitable surface texture with less surface contamination compared to other methods [10,11]. More recently, ultrafast femtosecond lasers have become an advanced tool for material processing as it enables precision machining of localized spatial patterns down to nanometer dimensions [12]. Such a precision was possible due to highly nonlinear multiphoton interaction of light with matter resulting in rapid energy deposition with reduced heat affected zone and minimal debris around the work area. As a result, ultrafast lasers have evolved as a fast and economical tool for micro/nano machining of various materials [13].

One of the key outcomes of the interaction of intense light with materials is laser-induced porosity. While femtosecond laser induced porosity has been well studied using contact angle measurement technique on millimeter dimensions [6], very little information is available on micron dimensions. Other techniques to measure porosity have similar drawbacks. Since cell dynamics is very sensitive to the changes in the microenvironment [4], knowledge of laser induced topographical and morphological changes to the material on micro/nano dimensions is essential.

Femtosecond laser ablation of PMMA has been widely studied due to its biocompatibility [14,15]. However, porosity of the resulting ablated features on micron scale has not been investigated in detail. Recently it has been shown that protein binding on PMMA can be enhanced through femtosecond surface ablation [16]. Also changes in wettability of PMMA surfaces have been correlated to laser-induced surface porosity at the micro-scale [6].

In this paper, we study femtosecond laser-induced porosity in PMMA for shot-to-shot and line ablation regimes. We use imaging technique to quantify laser-induced porosity. In the shot-to-shot regime, we show the evolution of porosity within the ablated crater from a single laser pulse to multiple pulses. An increase in porosity is found with increasing number of pulses. For multiple laser pulses, we show the porous area fraction (defined as ratio of total area covered by the pores to the total area of the ablated crater) to decrease with increasing pulse energies while the pore size distribution peaks at smaller pore areas. In the line ablation regime, the porous area fraction is found to increase with scanning speeds regardless of the pulse energy used. Two different regimes were

* Corresponding author. [redacted]
E-mail addresses: [redacted]F. Baset), [redacted] Villafranca), [redacted] (J.-M. Guay), [redacted]j@uottawa.ca (R. Bhardwaj).

0169-4332/$ – see front matter © 2013 Elsevier B.V. All rights reserved.
http://dx.doi.org/10.1016/j.apsusc.2013.06.043

observed for the formation of quasi-periodic porous structures at low and high scanning speeds originating from different physical effects.

2. Materials and methods

Femtosecond pulses from a Ti:Sapphire laser system (Spectra-Physics) operating at a central wavelength of 800 nm and a repetition rate of 5 kHz were focused onto an optically polished bulk PMMA samples (12.5 mm × 12.5 mm × 1.7 mm) using a 0.25 NA (10×) microscope objective. The laser was operated either in an external trigger mode (for single and multi-shot experiments) or continuous mode (for line ablation). A thin broadband beam sampler at the output of the laser directed a small fraction of the beam into a single-shot autocorrelator to continuously monitor the pulse duration. The pulse duration before the microscope objective was measured to be ~70 fs, obtained by propagating the pulse through all the dispersive optics used in the experiment positioned in front of the autocorrelator. Pulses were not pre-chirped. The incident pulse energies were measured after the microscope objective taking into account losses of all the optics. The incident power was varied and monitored with neutral density filters and a calibrated fast photodiode, respectively. The polarization of the incident light was varied by a half-waveplate (quarter-waveplate) to obtain linear (circular) polarized light. The back aperture of the microscope objective (8 mm) was slightly overfilled to minimize alignment errors. The position of the laser focus relative to the surface of the sample was accurately determined by imaging the back-reflected light with a CCD camera at very low pulse energies below the ablation threshold. Samples were mounted on three-axis translation stages with a resolution of 50 nm (100 nm) in lateral (axial) dimensions and a maximum translation speed of 20 mm/s.

The laser-ablated regions were characterized by a scanning electron microscope (SEM) after coating the PMMA surface with a thin layer (few nanometers) of gold to make them conductive. The spot size was obtained from the slope of semi-logarithmic plot of the squared diameter of the modified region measured with the SEM as a function of pulse energy. We obtained a Gaussian beam radius of $2.7 \pm 0.2\,\mu m$ for a 0.25 NA microscope objective (close to the diffraction limited beam radius of ~2 μm). The single shot ablation threshold of PMMA, defined as the lowest energy at which ablation features were visible under the SEM, was determined to be 0.6 μJ corresponding to a laser fluence of $2.6\,J/cm^2$, which is in good agreement with the published data [17]. Laser induced porosity was quantified by analyzing the SEM images of ablated craters and lines with the aid of ImageJ software [18]. After matching the scale of the software with that of the SEM, the images were inverted and adjusted for brightness and contrast to reveal only the pores. Analyzing the number of pixels in a given pore provided the area of the pore. The minimum pore area that was accounted for was $0.003\,\mu m^2$. For the purpose of analyzing the pore area, all SEM images were taken with the electron beam perpendicular to the sample (zero tilt).

3. Results and discussion

3.1. Shot-to-shot evolution of laser induced porosity

Fig. 1 shows evolution of femtosecond laser-induced porosity within the ablation craters on PMMA for different number of laser pulses and pulse energies above the ablation threshold for PMMA. The laser polarization was circular. A single laser pulse induces a pore in the middle of the crater whose area is approximately $0.6\,\mu m^2$, independent of pulse energy. As the pulse energy

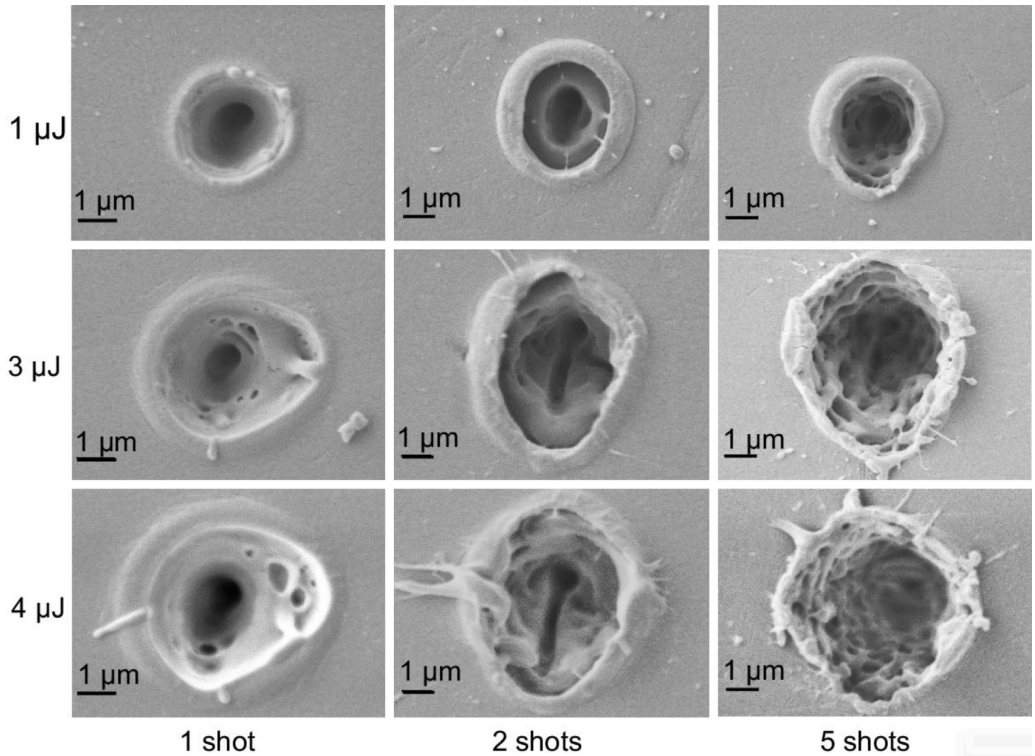

Fig. 1. SEM images of femtosecond laser ablated structures in PMMA showing the evolution of porosity for 1, 2 and 5 laser shots (from left to right column, respectively) at pulse energies of 1, 3 and 4 μJ (from top to bottom row, respectively). Laser polarization was circularly polarized with an ellipticity of ~0.9.

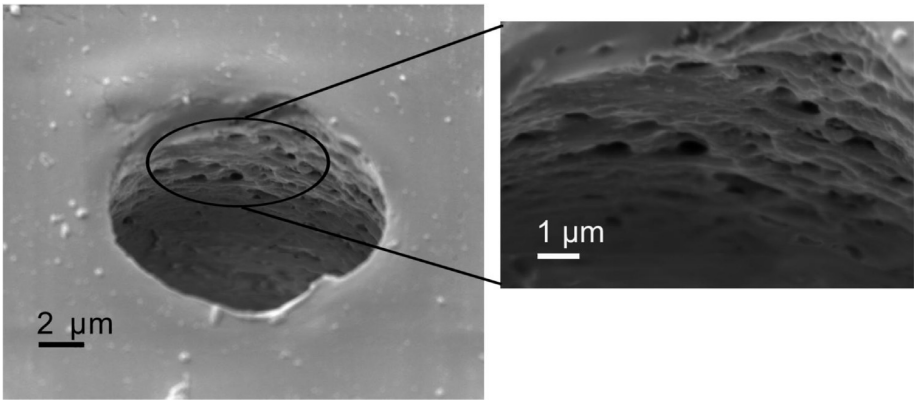

Fig. 2. SEM image of the side view of an ablation crater produced by linearly polarized light with pulse energy of 5 μJ and 5 laser shots delivered to the region.

is increased from 1 to 4 μJ, few small pores surround the central pore with area ranging from 0.005 to 0.14 μm^2.

When two laser pulses are incident on PMMA, at low pulse energies (for example 1 μJ in Fig. 1) the ablation crater consists of 3 regions. A pore in the middle surrounded by a volcanic crater like structure (area ~ 15 μm^2) that is encircled by a ruptured dome-like structure. At higher pulse energies, the central pore is elongated and the surrounding region becomes porous while ruptured dome-like structure persists.

Increasing the number of laser pulses increases the porosity and at the same time the ablation craters become deeper. As a result the porosity evolves from being predominantly a 2D effect for a single laser shot to being a 3D effect for 5 laser pulses. The porous area fraction increases from 6% for a single shot to 9% for 2 shots and 12% for 5 shots for a 3 μJ pulse. These are only approximate values, as the estimated area of the pores with ImageJ software in deeper craters will be affected by the 3D effect.

For higher pulse energies, the ablated hole gets much deeper and the walls become porous as shown in Fig. 2 obtained with 5 laser shots and pulse energy of 5 μJ. A closer inspection of the ablated hole reveals a quasi-honeycomb like structure on the sidewalls. This is interesting because in PMMA porosity mainly arises due to localized melting and explosive boiling. Ultrashort pulse laser irradiation leads to near isochoric heating and rapid adiabatic expansion. A two-phase liquid–gas mixture develops after thermalization of the laser energy in the material (on the ps time scale) which then undergoes hydrodynamic expansion, resulting in material ejection and subsequent resolidification on the ns time scale [19,20]. As a result, ablation of PMMA is inhomogeneous with formation of nanostructures at the bottom of the crater (Fig. 1). However, for multiple laser pulses and higher energies nanostructures start to develop along the sidewalls as well (Fig. 2). Considering the Gaussian profile of laser intensity nanostructures on the sidewalls is not anticipated.

We now study the effect of pulse energy on laser-induced porosity in PMMA for a fixed number of laser pulses. Fig. 3 shows the ablation craters obtained with linearly polarized light for 5 laser pulses with energies ranging from 1 to 5 μJ. Ablation craters are all elongated along the laser polarization. Such an elongation was recently shown to arise from local field enhancement during light-plasma interaction [21]. The elongation disappears for multiple pulses. At low energy, few big pores were formed compared to the size of the crater but as the energy was increased, the number of pores also increased with smaller pores being more predominant.

These observations are quantified in Fig. 4 which shows for different pulse energies (a) porous area fraction, defined as the ratio of total area of the pores to that of the ablation crater and (b) the distribution of pore area size. As the pulse energy increases the

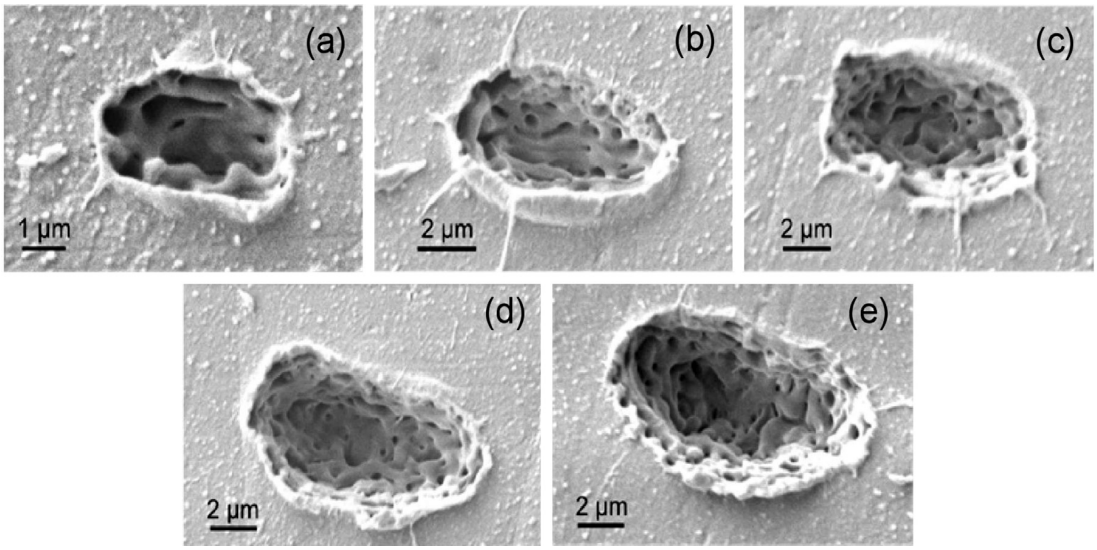

Fig. 3. SEM images of laser induced porosity inside the ablation crates of PMMA produced with 5 laser shots of linearly polarized light and pulse energies of (a) 1, (b) 2, (c) 3, (d) 4 and (e) 5 μJ.

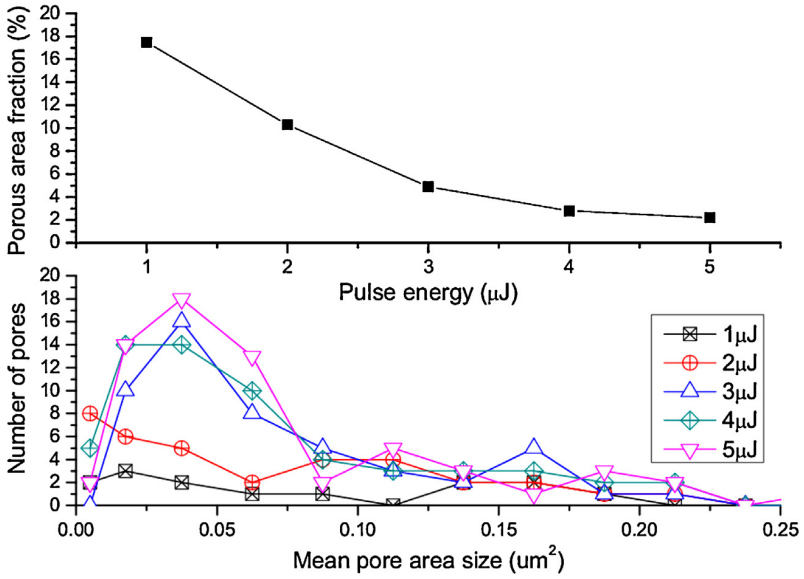

Fig. 4. Analysis of porosity inside ablated craters shown in Fig. 3. (a) Porous area fraction [the total area covered by the pores over the total area of the ablated crater] as a function of laser average energy. (b) Distribution of pore area size for different pulse energies.

porous area fraction decreases as shown in Fig. 4(a) due to two factors, (i) the overall crater area increases and (ii) the pore size decreases although their number increases. Fig. 4(b) shows the pore area size distribution for different pulse energies starting from 1 μJ to 5 μJ. A bin width of 0.025 μm^2 was chosen and the distribution was obtained by counting the number of the pores within the bin plotted against the mean pore area size. For the lowest energy, the pore area size distribution is nearly flat. This remains same as the pulse energy is increased to 2 μJ except that the number of smaller pores increases. However, at higher energies smaller pores are produced predominantly and the distribution peaks at a pore area size of 0.037 μm^2. The total number of pores increases by 4-fold from the lowest to the highest energy.

3.2. Porosity in line ablation

In line ablation, laser induced porosity depends on pulse energy and the scanning speed with which the laser focus is moved. Fig. 5(a)–(d) shows SEM images of ablated lines with pulse energy of 700 nJ for different scanning speeds of 5, 2.5, 1 and 0.5 mm/s which correspond to 1, 2, 5 and 10 shots/μm, respectively. The polarization of light was linear making an angle of 45° with respect to the scanning direction. Very distinct microstructures are observed within the ablation lines for different scanning speeds. At the highest speed (5 mm/s), quasi-periodic porous structures are observed with a period of ~1 μm oriented perpendicular to the scanning direction (Fig. 5(a)).

This periodicity was independent of pulse energy. At the intermediate speeds (2.5 and 1 mm/s), a more random distribution of pores is found (Fig. 5(b) and (c)). Interestingly, at the lowest speed (Fig. 5(d)) quasi-periodic porous structures parallel to the direction of the laser polarization are formed with a period of ~350 nm. In our previous study we have shown the orientation of such quasi-periodic porous structures to change with the laser polarization [21].

Laser-induced periodic surface structures (or surface ripples) have been observed in ablation of several materials under widely different illumination conditions. In metals [22,23],

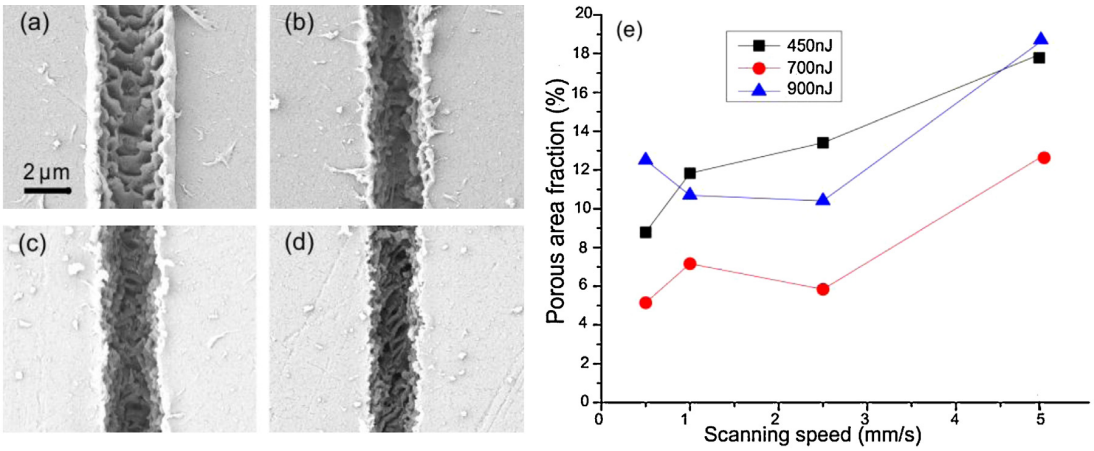

Fig. 5. SEM images of line ablation with pulse energy of 700 nJ and linearly polarized light (45°) using a scanning speed of (a) 5, (b) 2.5, (c) 1 and (d) 0.5 mm/s. (e) Porous area fraction (%) as a function of scanning speed for different pulse energies.

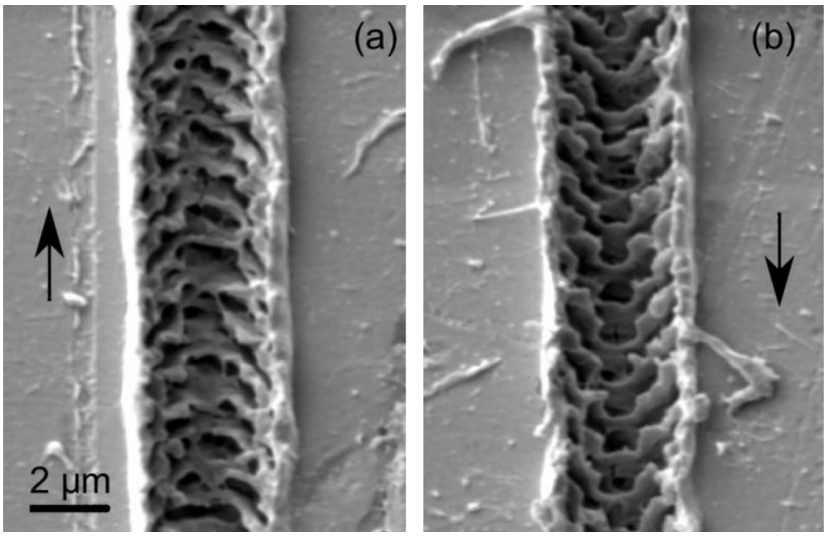

Fig. 6. SEM images of line ablation with linearly polarized light (45°) using a scanning speed of 5 mm/s. Arrows indicate the direction of the laser focus with respect to the smaple. The pulse energy was 1 μJ.

semiconductors [24,25] and dielectrics [26,27], the structures have been found to be mostly perpendicular to the laser polarization whereas in polymers they are mostly parallel [28–30]. However, periodic structures perpendicular to the laser polarization in polymers [31] and parallel in dielectrics [32,33] have also been observed. The ripple formation is described in terms of interference between the incident light and the surface scattering wave [34,35] or surface plasmon polaritons [36]. Polarization-dependent self-organized three-dimensional (3D) periodic nanostructures have been observed inside fused silica [37] under irradiation with multiple light pulses. For linearly polarized light, bulk grating-like structures were formed orthogonal to the laser polarization and their origin was attributed to local field enhancement arising from interaction of light with under-dense plasma [37]. In contrast, during laser ablation the plasma is over-dense, subsequent interaction of light with plasma can lead to structures that are parallel to the laser polarization.

Fig. 5(e) exhibits an overall trend of an increase in porous area fraction with increasing scanning speed. However, no clear trend was observed for different energies in the 450–900 nJ range. The porous structures shown in Fig. 5(a) with a quasi-periodicity of ~1 μm is imposed by a combination of the spot size and scanning speed. At 5 mm/s only one laser pulse is incident per micron of the sample. This discrete nature of irradiating the sample leads to successive micro-explosions followed by ejection of the material resulting in formation of periodic structures perpendicular to the scan direction. Their orientation changes with the direction in which the laser focus is moved as shown in Fig. 6. At lower scanning speeds (1 mm/s and 2.5 mm/s), multiple pulses are incident on the sample at a given spot. As a result, the quasi-periodic structures disappear and porosity becomes random. In contrast at 0.5 mm/s, the quasi-periodicity of the porous structures that are parallel to the laser polarization arises due to the interaction of light with plasma that is over the critical density. Moreover, their orientation is independent on the direction in which the laser focus is moved.

4. Conclusion

In this paper, we carried out parametric studies on laser-induced porosity on PMMA surface and have shown that it depends on pulse energy, number of laser shots and scan speeds. We find the porosity, quantified by pore size distribution and porous area fraction, to increase with multiple laser pulses incident on PMMA. Molecular dynamic simulations have shown that nanopore formation is an important mechanism for temperature equilibration during the interaction of intense femtosecond pulses with PMMA. The number of pores and their size increases with pulse energy [38]. For line ablation, the porosity is predominantly determined by the speed with which the laser focus is moved on the sample and leads to two different types of quasi-periodic structures; sub-wavelength structure parallel to the laser polarization in multi-pulse regime and microstructures perpendicular to scan direction in single shot regime. Induced porosity in PMMA will have interesting consequences in bio-medical applications. Since PMMA mimics soft-matter and is biocompatible and stable in physiological environment it has been used in several areas such as cosmetic surgery [39], dentistry [40] and ophthalmology [15]. Surface structuring on micro- and nanoscale will promote cell adhesion and proliferation at the polymer–tissue interface leading to enhanced tissue integration resulting in better implant union.

Acknowledgements

The authors would like to thank Natural Science and Engineering Research Council, Canadian Foundation for Innovation and the Ontario Ministry of Economic Development and Innovation for financial support.

References

[1] S. Singh, H.S. Nalwa, Journal of Nanoscience and Nanotechnology 7 (2007) 3048–3070.
[2] N. Sykaras, A.M. Iacopino, V.A. Marker, R.G. Triplett, R.D. Woody, International Journal of Oral & Maxillofacial Implants 15 (2000) 675–690.
[3] T. Vignaud, R. Galland, Q. Tseng, L. Blanchoin, J. Colombelli, M. Théry, Journal of Cell Science 125 (2012) 2134–2140.
[4] A.D. Doyle, F.W. Wang, K. Matsumoto, K.M. Yamada, Journal of Cell Biology 184 (2009) 481–490.
[5] D.M. Brunette, P. Tengvall, M. Textor, M. Thomsen, in: D.M. Brunette (Ed.), Titanium in Medicine: Material Science, Surface Science, Engineering, Biological Responses and Medical Applications, Springer-Verlag, Berlin Heidelberg, New York, 2001.
[6] C. De Marco, S.M. Eaton, R. Suriano, S. Turri, M. Levi, R. Ramponi, G. Cerullo, R. Osellame, Applied Materials & Interfaces 2 (8) (2010) 2377–2384.
[7] L. Hao, J. Lawrence, L. Li, Applied Surface Science 247 (2005) 453–457.
[8] E. Yap, D.G. McCulloch, D.R. McKenzie, M.V. Swain, L.S. Wielunski, R.A. Clissold, Journal of Applied Physics 83 (1998) 3404–3412.
[9] J. Yoon, M. Jin, M. Lee, Advanced Materials 23 (2011) 3974–3978.

[10] M. Bereznai, I. Pelsöczi, Z. Tóth, K. Turzó, M. Radnai, Z. Bor, A. Fazekas, Biomaterials 24 (2003) 4197–4203.
[11] A. Gaggl, G. Schultes, W.D. Müller, H. Kärcher, Biomaterials 21 (2000) 1067–1073.
[12] S. Nolte, B.N. Chichkov, H. Welling, Y. Shani, K. Liebermann, H. Terkel, Optics Letters 24 (1999) 914–916.
[13] A.Y. Vorobyev, C. Guo, Applied Surface Science 253 (2007) 7272–7280.
[14] S. Baudach, J. Bonse, J. Kruger, W. Kautek, Applied Surface Science 154–155 (2000) 555–560.
[15] A.A. Serafetinides, M. Makropoulou, E. Fabrikesi, E. Spyratou, C. Bacharis, R.R. Thomson, A.K. Kar, Applied Physics A 93 (2008) 111–116.
[16] X. Ma, H. Huo, M. Wei, L. Wang, M. Shen, C. Barry, J. Mead, Applied Physics Letters 98 (2011) 171101.
[17] J. Kruger, W. Kautek, Advances in Polymer Science 168 (2004) 247–289.
[18] L. Reinking, Examples of Image Analysis Using ImageJ, 2007, Available at: http://rsbweb.nih.gov/ij/docs/pdfs/examples.pdf
[19] V.V. Zhakhovski, K. Nishihara, S.I. Anisimov, N.A. Inogamov, JETP Letters 71 (2000) 167–171.
[20] S.I. Anisimov, N.A. Inogamov, A.M. Oparin, B. Rethfeld, T. Yabe, M. Ogawa, V.E. Fortov, Applied Physics A 69 (6) (1999) 617–620.
[21] J.M. Guay, A. Villafranca, F. Baset, K. Popov, L. Ramunno, V.R. Bhardwaj, New Journal of Physics 14 (2012) 085010.
[22] B. Huis in't Veld, H. van der Veer, Journal of Laser Micro/Nanoengineering 5 (1) (2010) 28–34.
[23] S. Sakabe, M. Hashida, S. Tokita, S. Namba, K. Okamuro, Physical Review B 79 (2009) 033409.
[24] A. Borowiec, H.K. Haugen, Applied Physics Letters 82 (25) (2003) 4462–4464.
[25] D. Dufft, A. Rosenfeld, S.K. Das, R. Grunwald, J. Bonse, Journal of Applied Physics 105 (2009) 034908.
[26] J. Reif, F. Costache, M. Henyk, S.V. Pandelov, Applied Surface Science 197–198 (2002) 891–895.
[27] F. Costache, M. Henyk, J. Reif, Applied Surface Science 208–209 (2003) 486–491.
[28] S. Baudach, J. Bonse, W. Kautek, Applied Physics A 69 (1) (1999) S395–S398.
[29] M. Forster, W. Kautek, N. Faure, E. Audouard, R. Stoian, Physical Chemistry Chemical Physics 13 (9) (2011) 4155–4158.
[30] J. Krüger, W. Kautek, Advances in Polymer Science 168 (2004) 247–289.
[31] J. Heitz, E. Arenholz, D. Bäuerle, R. Sauerbrey, H.M. Phillips, Applied Physics A 59 (1994) 289–293.
[32] Y. Han, X. Zhao, S. Qu, Optics Express 19 (2011) 19150.
[33] Q. Wu, Y. Ma, R. Fang, Y. Liao, Q. Yu, Applied Physics Letters 82 (11) (2003) 1703–1705.
[34] J.F. Young, J.E. Sipe, H.M. van Driel, Physical Review B 30 (1984) 2001.
[35] J.S. Preston, H.M. Van Driel, J.E. Sipe, Physical Review B 40 (1989) 3942–3954.
[36] M. Huang, F.L. Zhao, Y. Cheng, N.S. Xu, Z.Z. Xu, ACS Nano 3 (2009) 4062.
[37] V.R. Bhardwaj, E. Simova, P.P. Rajeev, C. Hnatovsky, R.S. Taylor, D.M. Rayner, P.B. Corkum, Physical Review Letters 96 (2006) 057404.
[38] F. Baset, K. Popov, A. Villafranca, J.M. Guay, Z. Al-Rekabi, A. Pelling, L. Ramunno, V.R. Bhardwaj, Optics Express 21 (10) (2013) 12527.
[39] M.J. Groth, A. Bhatnagar, W.J. Clearihue, R.A. Goldberg, R.S. Douglas, Archives of Facial Plastic Surgery 8 (6) (2006) 381–389.
[40] R.Q. Frazer, R.T. Byron, P.B. Osborne, K.P. West, Journal of Long-Term Effects of Medical Implants 15 (6) (2005) 629–639.

Chapter 6

Applications

6.1 Introduction

Laser micro/nano structuring has several applications. In this chapter, section 6.2.1 briefly describes an ultralong complex 3D microfluidic channel inside bulk dielectric material fabricated by femtoetch technique, that can have potential applications in biomedical sensing. Section 6.2.2 demonstrates the similar technique (femtoetch technique) to fabricate a fiber-based microcantilever sensor. The next topic in section 6.2.3 describes a fiber-based microcantilever vibration sensor, capable of providing in-line measurement of frequency and amplitude of vibration. Section 6.2.4 shows preliminary result of the same fiber-based microcantilever, that has potential to be used as chemical or, bio-chemical sensor. Finally, section 6.3 describes refractive index modification in the bulk of transparent materials. This refractive index modulation within the bulk of dielectric material was utilized to fabricate photonics devices or, within the single mode fiber core at random spacing to fabricate a quasi-random micro-cavities fiber laser.

6.2 Femto-etch technique

Today, one of the most common procedure to fabricate microfluidic channel inside dielectrics is femto-etch technique. This femto-etch technique uses a combination of femtosecond laser pulses and highly anisotropic etching with an etchant. In femto-etch technique, the first step is to locally modify the refractive index of a dielectric material along the laser-illuminated path by focusing the femtosecond laser at the surface, or inside the sample and scanning the laser focus with a specific speed. In a subsequent

step, the modified region is made to react with an etchant that attacks the modified material along the laser illuminated path since the etching rate of the laser modified region is enhanced by several orders of magnitude compared to the untreated material. As opposed to laser ablation, this method (femto-etch) has no heat effect as the material etches away. Also, by confining the laser focus inside the sample together with etching, complex 3D microfeatures can be achieved. The following subsections will present some of the applications using femto-etch technique.

6.2.1 Microfluidic channel in fused silica by femto-etch technique

As mentioned in the previous section 6.2, localized changes in refractive index of dielectrics induced by femtosecond laser together with selective chemical etching leads to fabricate these complex 3D microfluidic networks. These structures have potential applications in biomedical sensing, quantum optics and optical communications.

The same laser set up has been used as in section 6.3.2. The femtosecond laser fabrication process employs a regeneratively amplified Ti:sapphire laser generating 45 fs, 500 μJ, 800 nm pulses at 1 kHz. A fraction of the beam is focused, by a NA = 0.55 objective, at a depth ranging from 150 μm to 250 μm below the surface of the fused silica sample (0.5 cm $\times$ 0.5 cm $\times$ 0.5 cm), which is moved perpendicular to the beam propagation direction by a precision translation stage at a specific speed. For our experiment, we used two different set of speeds, 20 μm/s and 50 μm/s and the laser focus was scanned across the sample from one end to another (y direction) at a horizontal plane (xy), 150 μm below the cube fused silica surface with pulse energies ranging from 300 nJ to 2 μJ. Another waveguide was scanned at vertical direction (z direction) from the middle of the horizontal waveguide, toward the top surface of the sample. Therefore, after modification (and etching), the modified waveguide will take the shape of a T-channel. The reason for adding a vertical channel in the middle is to ease the flow of etchant and speed up the fabrication process. The laser parameters should be carefully chosen to introduce uniform index modification to support the best etching conditions [80].

In a subsequent step, the modified region of the silica sample is etched by reacting with an etchant that attacks the modified material along the laser-illuminated path. In our case, we have used 2.5 % volume aqueous hydrofluoric (HF) acid in an ultrasonic bath. The resultant dangling oxygen bonds due to reconfiguration of ring structure (resulting

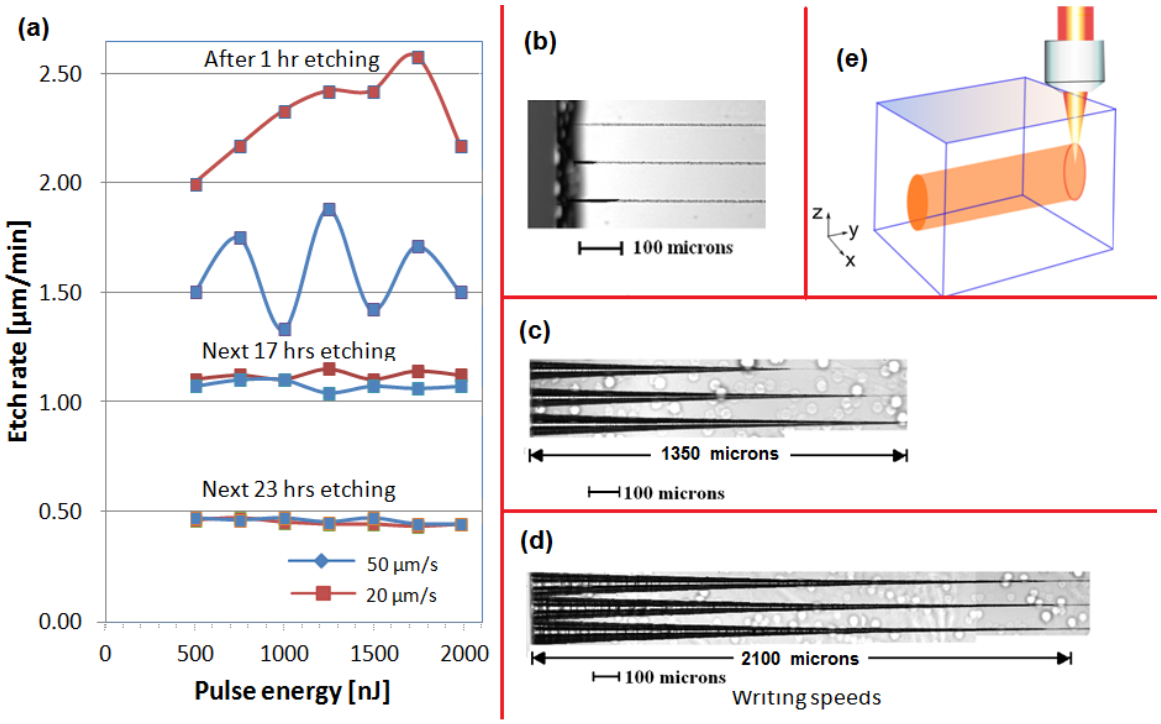

Figure 6.1: (a)Etch rates of modified fused silica channels as a function of pulse energy in 2.5 % volume aqueous hydrofluoric (HF) acid for two different speeds, 50 μm/s (diamond symbol) and 20 μm/s (square symbol). (b)–(d) Optical microscope images of the longitudinal cross-sectional images of the etched channel after 1 hour, next 17 hours and the last 23 hours. (e)A schematic illustration of the laser writing set up for refractive index modification inside fused silica sample.

from fs laser-silica interaction) are highly reactive to HF acid. Etching is proportional to the degree of index change. Therefore, depending on the degree of index modification and the etching time, it is possible to control the height, width and length of the channel.

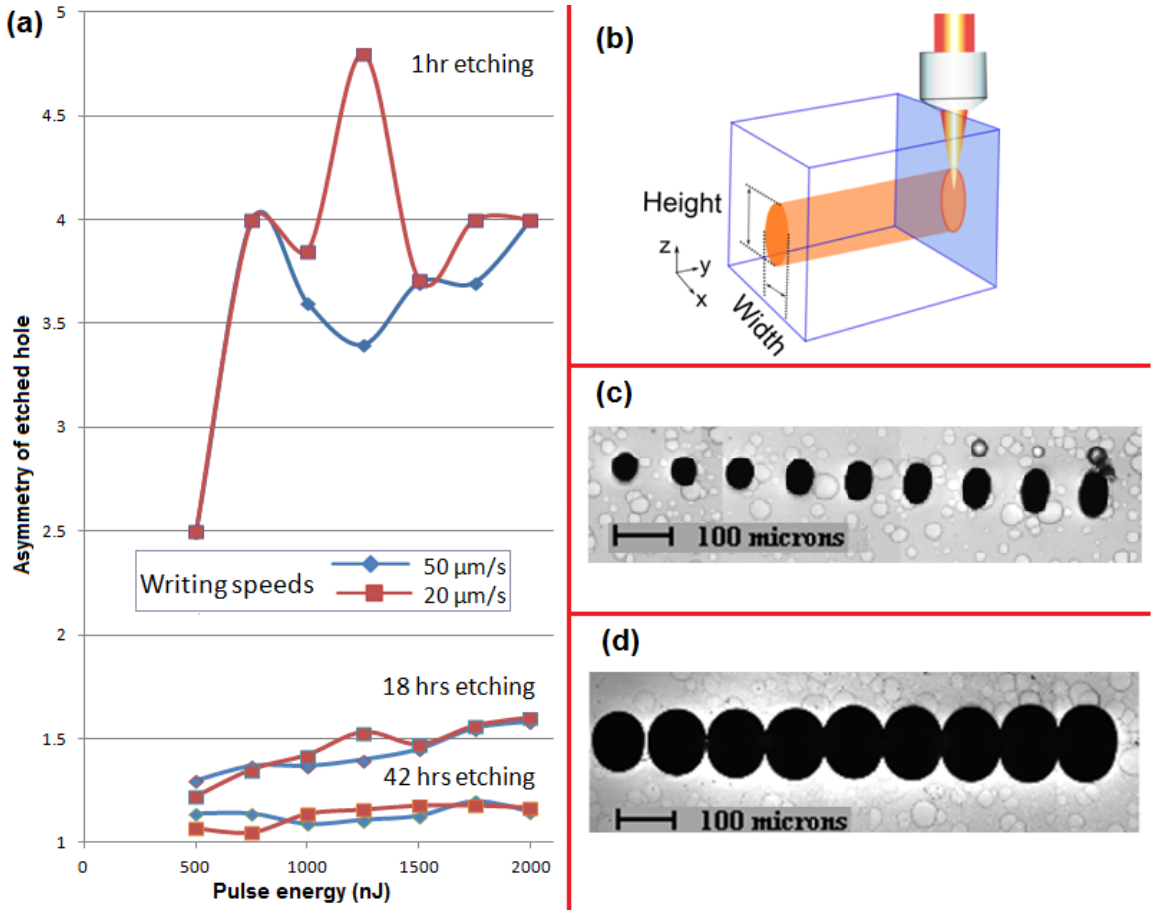

Figure 6.2: (a)Asymmetry of the transversal cross-section of the modified fused silica channels with increasing etching time as a function of pulse energy in 2.5 % volume aqueous hydrofluoric (HF) acid for two different speeds, 50 μm/s (diamond symbol) and 20 μm/s (square symbol), respectively.(b)A schematic illustration of the laser writing set up for refractive index modification inside fused silica sample. (c),(d) Optical microscope images of the transversal cross-sectional images of the etched channel after 18 hours and 42 hours.

Figure 6.1(a) shows the etch rates of the lengths of modified fused silica channels for different pulse energies. Two different writing speeds (50 μm/s and 20 μm/s) were used to compare the etching rates. Figure 6.1(a)exhibits an overall trend of an increase of

etch rates with increasing pulse energy and the etch rate is higher for lower scanning speed (20 μm/s). Figure 6.1(b)– Figure 6.1(d) show the optical microscope image of the longitudinal cross-section (xy views) of the microfluidic channels after 1 hr, 18 hours and 41 hours etching in the 2.5 % hydrofluoric (HF) acid. Figure 6.1(e) shows the schematic illustration of femtosecond laser writing set up inside fused silica sample for horizontal channel at a certain depth from top surface.

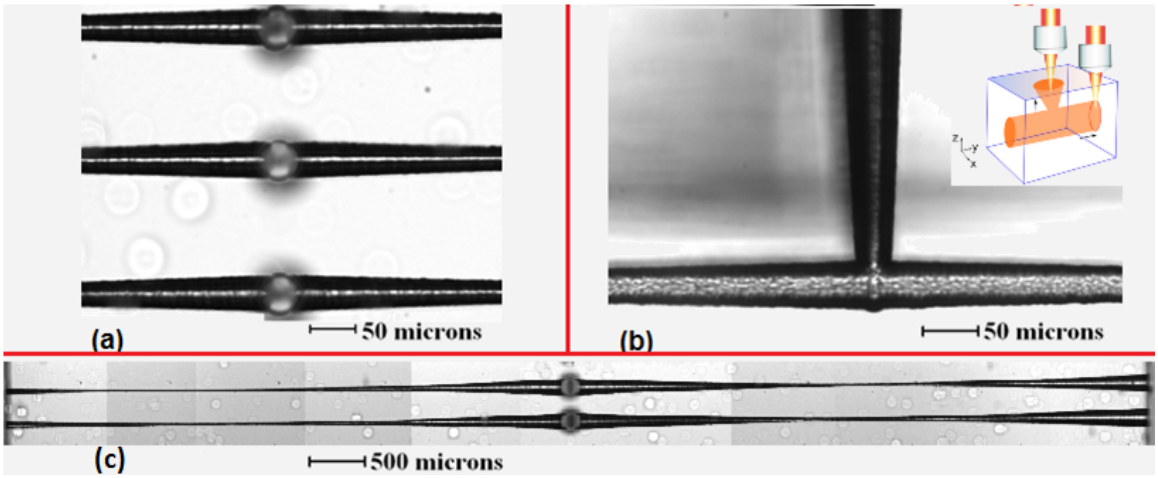

Figure 6.3: (a) Top view of the 3D microfluidic channel fabricated by femto-etch technique. (b) Side view of the T-channel fabricated by femto-etch technique. Inset shows the schematic illustration of the femtosecond laser writing set up for fabricating T-channels inside fused silica sample. (c) Top view of the stitched image of 5 mm long channel.

Figure 6.2(a) shows the evolution of the asymmetry of the transversal cross-section of the modified fused silica channels for different pulse energies respectively after etching for different time period. Here, asymmetry parameter defined as the ratio of the etched hole dimensions along the two orthogonal axes as shown in Figure 6.2(c) and (d). Again, two different writing speeds (50 μm/s and 20 μm/s) were used to compare the etching rates. The graph exhibits an overall trend of an increase of etch rates with increasing pulse energy and the etch rates are comparable for both speeds. Figure 6.2(c) and Figure 6.2(d) show the optical microscope image of the transversal cross-section (xz views) of the microfluidic channels after 18 hours and 42 hours etching in the 2.5 % hydrofluoric (HF) acid. Figure 6.1(b) shows the schematic illustration of femtosecond laser writing set up inside fused silica sample for horizontal channel at a certain depth from top surface.

Figure 6.3(a) shows the optical microscope image of the top view (xy view) after the

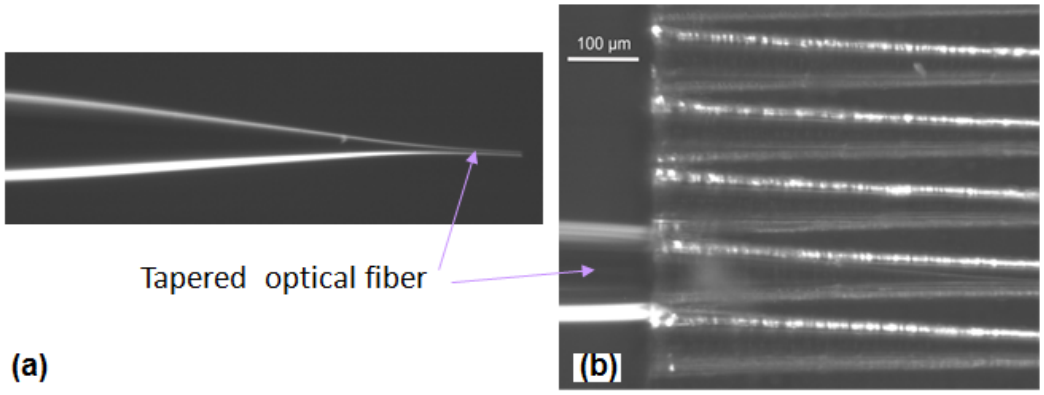

Figure 6.4: (a) Optical microscope image of a tapered optical fiber. (b) Optical microscope image of a tapered optical fiber inserted inside the microfluidic channel for fiber sensing application.

modified region of the fused silica waveguide being completely etched and formed a 3D microfluidic channel. With etching from both sides, after 41 hours the channel lengths up to 5 mm with 80 μm cross section are obtained. Figure 6.3(b) shows the optical microscope image of the side view (yz view)of the fabricated T-channel by femto-etch technique. Inset shows the schematic illustration of the femtosecond laser writing set up inside fused silica sample for T-channel. Figure 6.3(c) shows the optical microscope image (stitched) of the top view (xy view)of the 0.5 cm long microfluidic channel fabricated by femto-etch technique.

These microfluidic channels in conjunction with a tapered optical fiber can be used to detect biological or chemical species. Figure 6.4(a) shows a tapered optical fiber and Figure 6.4(b) shows the tapered optical fiber inserted inside the fabricated microfluidic channel. These have potential applications in biomedical sensing and monitoring of chemical reactions. Further experiments should be carried out to test these microfluidic channels for fiber sensing applications and speed up the over all fabrication process and improve the quality of these complex 3D channels.

6.2.2 Fiber microcantilever by femto-etch technique

In recent years, all-optical fiber sensors based on Fabry-Perot interferometer (FPI) and Mach-Zehnder interferometer (MZI) have attracted significant research attentions for their unique advantages of high fringe visibility, high refractive index (RI) sensitivity,

long temperature sensing range, versatile assemble element, electromagnetic immunity, compact size, and low cost [109, 110, 111]. With its advantages of small size, light weight, electromagnetic interference immunity, wide bandwidth, and low transmission loss, an optical fiber is a preferred platform for micro-sensors. Femtosecond lasers have been successfully used to fabricate all-optical fiber sensors based on FPI and MZI in various structures [110, 111, 112]. To avoid the bulky optical read-out system while maintaining a high sensitivity, the fabrication technique for these micro-sensors usually involve complicated and time-consuming steps, which may limit practical applications of these approaches. In this paper, we propose techniques to design and fabricate micro-cantilevers onto the end of standard single mode fibres using femto-etch technique, combining the capability of the fs lasers to induce localized change in refractive index of dielectrics with selective etching. Broad band source and optical spectrum analyzer are employed to interrogate the final cavity with a reflection spectrum based on its Fabry-Perot configuration . The proposed cantilever sensor shows huge possibility to be used in diverse sensing applications, for example in refractive index measurement, axial strain test, and acoustic sensor.

800 nm light from a Ti:Sapphire laser system operating at a repetition rate of 1 kHz and producing 45 fs pulses with a peak energy of 0.5 mJ, was focused at the surface of a single mode optical fibre (Corning, SMF-28) by a 0.4 NA microscope objective. The incident pulse energies were measured after the microscope objective and monitored by a calibrated fast photodiode. The position of the laser focus relative to the top and bottom of the fiber surface was accurately determined by imaging the back reflected light with a CCD camera at pulse energies much below the ablation threshold. Then the laser focus was precisely moved to the fiber core for index modification. A single-shot autocorrelator continuously monitored the pulse duration. The pulses were not prechirped and the duration was measured to be 70 fs at the back aperture of the objective. The laser-modified regions were characterized by an optical microscope. The laser focal spot radius of $2.7\pm0.2\mu$m was obtained from the slope of semi-logarithmic plot of the squared diameter of the modified region measured with the SEM as a function of pulse energy. The sample fibres (Corning, SMF-28) are 1.5 meter long, cleaved and mounted in a V-grooves holder for index modification. The diameters of the single-mode fiber core and cladding are 8.2 μm and 125 μm, respectively.

The first step of the femtoetch technique is to modify the refractive index of the SMF (jacket removed) by the femtosecond laser direct writing method. SiO_2 forms 5 membered ring structures in fused silica. Once the laser was focused at the surface

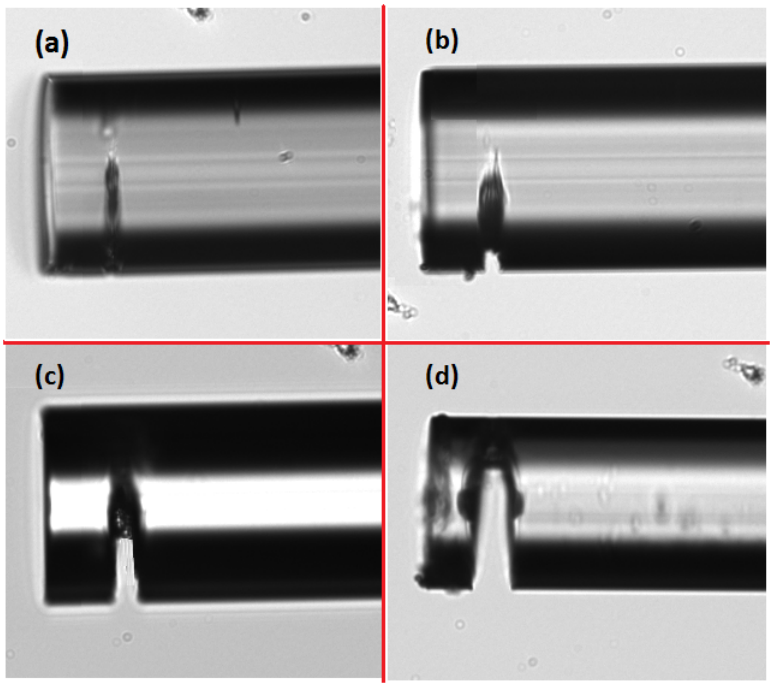

Figure 6.5: (a)Optical microscope image of the sideview of the SMF after the femtosecond laser modification. (b)–(d) Optical microscope images of the sideview of the modified SMF after 35 min, 3.5 hours and 7 hours etching with the 2.5 % volume aqueous hydrofluoric (HF) acid, respectively. The cavity (d) width is 30 μm, 40 μm away from the edge. Cavity depth is 85 μm.

(top/bottom) with a specific energy, the laser focus was scanned with a specific speed at a plane orthogonal to the fiber core along the entire transversal cross-section. The scanning process is repeated several times, only the focussing position of the laser inside the SMF was changed along the z-direction at a step of 5 μm (step size and number of repetition depend on the required depth of the cantilever cavity). For our experiment, the scanning was repeated for 13 times by changing the laser focus inside the SMF at z-direction. The usage of proper laser parameters drastically change the chemical affinity of the glass along the path of laser direct-writing. As a result of the laser-silica interaction, the 5-membered rings is reduced to 3, resulting in densification. In a subsequent step, the modified region of the single mode fiber is made to react with an etchant that attacks the modified material along the laser-illuminated path. In our case we have used 2.5 % volume aqueous hydrofluoric (HF) acid. The resultant dangling oxygen bonds due to reconfiguration of ring structure (resulting from fs laser-silica interaction) are highly reactive to HF. Etching is proportional to the degree of index change. Therefore, depending on the degree of index modification and the etching time, it is possible to control the width and depth of the microcantilever.

Figure 6.5(a) illustrates the sideview of the SMF after femtosecond laser modification with a scanning speed of 0.01 mm/s and pulse energy of 2 μJ. Figure 6.5(b)-(d) shows the sideview of the micro-cantilever after 35 min, 3.5 hours and 7 hours of the etching process begins. The fiber microcantilever used for our experiment had a cavity width and depth of 30 μm and 85 μm, respectively. The walls of the cavity at the end of the etching process are almost parallel to each other.

The experimental set-up for interrogating SMF micro-cantilever reflection spectrum is shown in Figure 6.6(a), where we used a Broad Band Source (BBS) and an optical spectrum analyzer to measure the reflected spectrum. The SMF microcantilever is the device under test. The light is coupled to the sensor via a coupler. The reflected light is partially reflected at the fibre-to-air (f-a), air-to-cantilever (a-c) and cantilever-to-air interfaces(c-a). When the light is propagating backwards, these signals pass through the same fibre coupler because of the higher reflection of the c-a surface (acting as mirror), interference is mainly contributed by (f-a) and (c-a) surface. Finally, reflection spectrum is acquired by an optical spectrum analyzer. Figure 6.6(b) shows that the fringes of the reflection spectrum have very small contrast and the free spectral range (FSR, distance between peaks) is random. It suggests that, the cavity made by femto-etch technique did not form an ideal FabryPerot configuration. Lower fluence and smaller step size in z direction might help to improve the etching condition, and ensure parallel walls inside

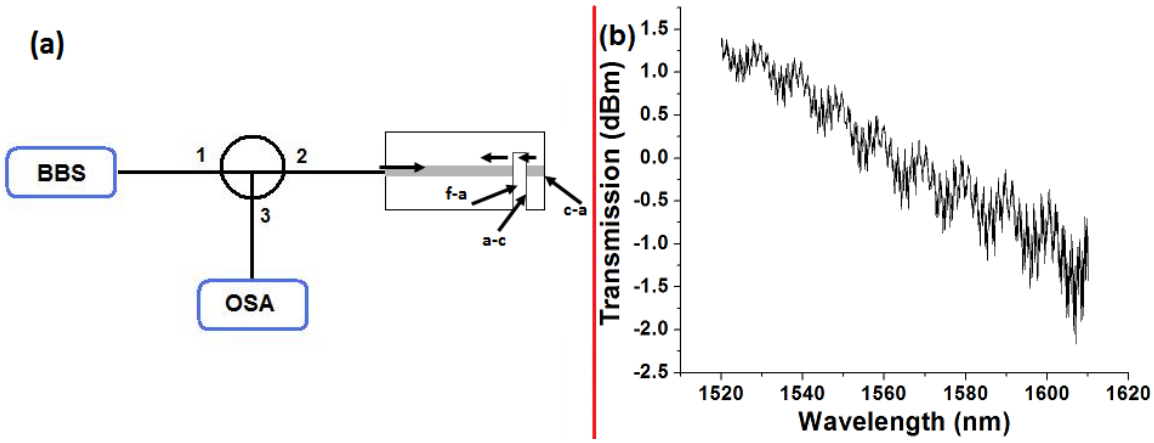

Figure 6.6: (a)Experimental setup of interrogation system of the fiber microcantilever structure.(b)Reflection spectrum of the fiber microcantilever structure.

the Fabry-Perot configuration.

In conclusion, we described micro-cantilevers fabrication using femto-etch technique at the end of a single mode optical fibre. We believe the femto-etch technique may offer potential for low cost mass production. In addition, an interrogation system with broad band source and a optical spectrum analyzer is used to produce a practical detection system. Proper choice of laser parameter and etching condition can significantly influence the walls of the cavity to be completely parallel and smooth, which in turn would improve the sensing quality. The proposed cantilever sensor, has great potential to be used in many areas, such as refractive index measurement, axial strain test, as well as acoustic sensor.

Later, to avoid multi-step processes associated with the femto-etch technique, we came up with a rather simple, single step process to fabricate a microcantilever in bend insensitive fiber with appreciable results. The following section 6.2.3 will provide detail information.

6.2.3 In-line fiber microcantilever vibration sensor

P. Lu, Y. Xu, **F. Baset**, X. Bao and V. R. Bhardwaj
In-line fiber microcantilever vibration sensor
Applied Physics Letters **103**, 211113 (2013)

In this section, we reported a single step process to fabricate an in-line fiber vibration sensor within a bend-insensitive fiber (BIF)[113]. A fiber microcantilever integrated with a readout fiber was fabricated by combining chemical etching and fusion splicing techniques. The microcantilever was fabricated from a BIF (Corning, ClearCurve) with a germanium doped silica core. The inner-cladding region of a BIF is made up with pure silica and enveloped by a ring of randomly distributed air-filled nanopockets, all surrounded by a pure silica outer-cladding region as shown in Figure 6.7(a). After removing the jacket from BIF, it was cleaved perpendicular to its longitudinal axis, and then etched in a solution of 2.5% or 5% volume aqueous hydrofluoric (HF) acid for different times and analyzed using a scanning electron microscope (SEM) and an optical microscope. Figures 6.7(a-d) show the SEM images of the transversal cross-section of the BIF after 30 seconds, 5 minutes, 30 minutes, and 60 minutes etching in the 5% HF solution, respectively. The region consisting of the air-filled nanopockets in the BIF is preferentially etched due to efficient transport of the etchant. As a result the nanoscale air voids gradually increase in size and merge, generating an air trench. The thickness of the air gap between the inner-cladding and outer-cladding layers as well as the trench depth increases with etching times to form a fiber microcantilever as shown in Figure 6.7(e).

Figure 6.8(a) shows the optical microscope image of the transversal cross-section of the BIF after 120 minutes etching in the 5% HF solution. To fabricate a compact fiber vibration sensor with an integrated readout optical fiber, the etched BIF (all experiments were performed with BIF etched for 120 minutes in the 5% HF solution) with microcantilever was spliced to a standard single-mode fiber (Corning, SMF-28) using a fusion splicer (Ericsson, FA995). Figure 6.8(b) shows a schematic illustration of the temperature distribution between the electrode pair of the fusion splicer. To avoid misalignment between the microcantilever and the readout fiber during splicing and to simultaneously guarantee a strong bonding between the two fibers, the arc discharge zone was shifted by 20 μm towards the readout fiber. During the arc discharge process, the microcantilever tip is heated to its softening point. Consequently, surface tension induced fiber deformation causes shrinking of the microcantilever length (L), creating an extended air cavity (gap between the microcantilever and readout fiber core) of length l depending on the discharge current. Figures 6.8(c) and (d) show the optical microscope images of the fiber microcantilever (both under the same 120 minutes of etching time in the 5% HF solution) fused with SMF-28 by applying discharge current of 9.0 mA and 11.5 mA, to create air cavity lengths of 25 μm and 105 μm, respectively. The microcantilever tip is

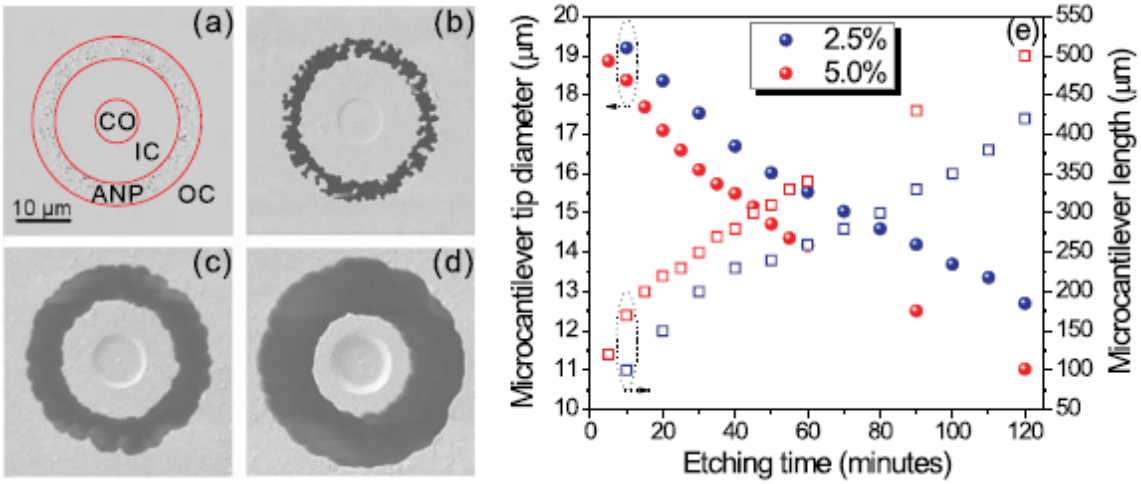

Figure 6.7: (a-d) SEM images of the transversal cross-section of the BIF after 30 seconds, 5 minutes, 30 minutes, and 60 minutes etching with the 5% HF solution, respectively. BIF consists of a germanium doped silica core (CO), a pure silica inner-cladding region (IC), a ring of randomly distributed air-filled nanopockets (ANP), and a pure silica outer-cladding region (OC) (e) Tip diameter (solid symbols) and length (open symbols) of the fiber microcantilever as a function of the etching time in 2.5% (blue) and 5%(red) HF solutions, respectively.

shaped as a hemispherical lens due to the thermal softening and surface tension, as seen in Figures 6.8(c) and (d), which could reduce the amount of back-reflected light without altering light divergence.

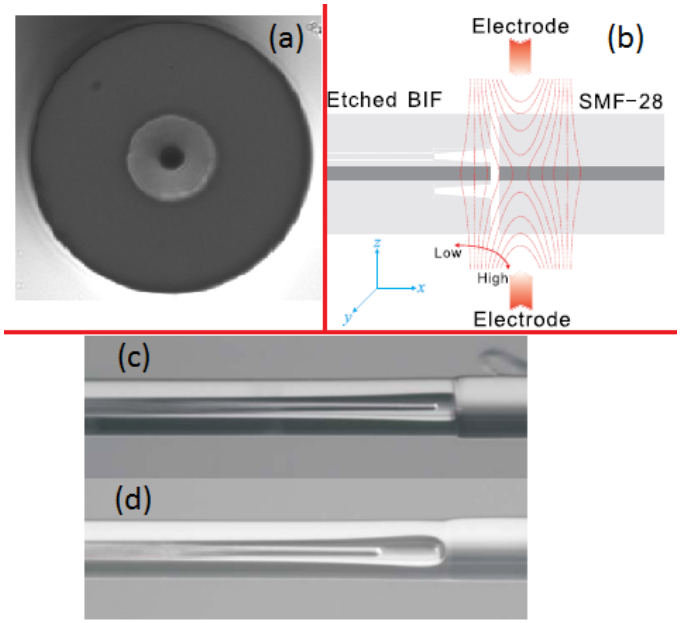

Figure 6.8: (a)Optical microscope image of the transversal cross-section of the BIF after 120 minutes etching in the 5% HF solution. (b) A schematic illustration of the discharge temperature distribution field between a pair of electrodes. Dashed lines represent isotherms and the solid line with arrows illustrates direction of higher or lower temperature. (c, d) Optical microscope images of the joint regions between the etched BIF (left) and the SMF-28 (right) with cavity lengths of 25 μm and 105 μm, respectively.

The principle of the shaker actuated in-line fiber vibration sensor is as follows, light from the microcantilever passes through the air cavity and is collected by the readout fiber. The coupling efficiency of light reaches maximum for zero vibrations as the microcantilever and readout fiber core are aligned. When the shaker is turned on, vibration induced bending of the microcantilever tip would angularly scan the readout fiber core resulting in modulation of transmitted power. This modulation in transmitted power provides an in-line measurement of frequency and amplitude of vibration.

To carry out the experiments, light from a 1550 nm planar waveguide based external cavity laser with the 3 kHz spectral linewidth (PLANEX, Rio) was launched into the in-line fiber microcantilever sensor and then guided through an attenuator and an

AC photodetector (PDB450C-AC, ThorLabs) to a high-speed oscilloscope (WaveRunner 64Xi-A, LeCroy). A shaker (TV51075, TIRA) was utilized as a continuous vibration source driven by a power amplifier and a function generator. A periodic sinusoidal driven signal with a particular peak-to-peak voltage caused a continuous vibration of the shaker that was transmitted to the fiber microcantilever and generated an up-down vibration. Experiments were carried out in a temperature-controlled room where the temperature was maintained at 22.0±0.5 °C.

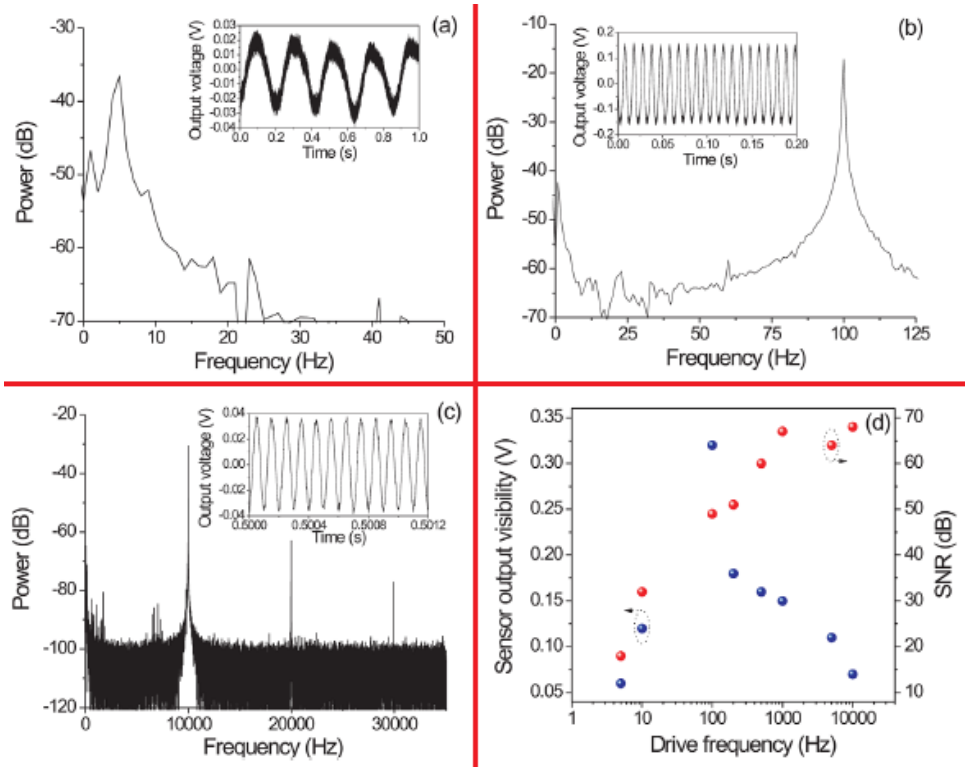

Figure 6.9: (a, b, c) The frequency-domain spectra of the fiber microcantilever sensor when the shaker was driven by sinusoidal signals of 5 Hz, 100 Hz, and 10 kHz, respectively. The insets show the corresponding time-domain spectra. (d) Frequency response of the in-line fiber microcantilever sensor output visibility (blue dots) and SNR (red dots).

Figures 6.9(a-c) show the frequency-domain spectra of the fiber microcantilever sensor (11 μm microcantilever tip diameter, 500 μm microcantilever length, and 105 μm cavity length) when the shaker was driven by the 1.5 volts sinusoidal signals of 5.0 Hz, 100.0 Hz and 10 kHz, respectively. The corresponding time-domain spectra are shown in the insets. The dominant peaks in the frequency-domain spectra are located at 4.9999 Hz,

99.9996 Hz, and 9977.96 Hz respectively, close to their corresponding drive frequencies. Two additional peaks at frequencies of 19954.9 Hz and 29932.9 Hz in Figure 6.9(c) are the high-order harmonics. Figure 6.9(d) shows the measured frequency response of the fiber microcantilever vibration sensor from 5 Hz to 10 kHz with corresponding output visibilities (peak-to-peak voltage) and signal-to-noise ratios (SNR). The sensor output visibility reaches a peak of 0.32 V at about 100 Hz (resonant frequency of the fiber microcantilever). The highest drive voltage of the shaker is 1.5 volts at the resonance frequency of 100 Hz as further increase in the drive voltage will not raise the maximum sensor output visibility anymore. The SNR of the corresponding frequency-domain spectra ranges from 18 dB to 68 dB over drive frequencies ranging from 5 Hz to 10 kHz. The frequency range of 5 Hz - 10 kHz can be actually extended to lower and higher frequency regimes, although with a much lower SNR of the frequency-domain signal for the low frequency vibration and a much smaller visibility of the time-domain signal for the high frequency vibration. This is mainly because: a) The SNR increases with drive frequency because the limit of the DC and near DC noise specifications is removed to avoid a reduced SNR, b) Too high drive frequency away from the resonant frequency of the fiber microcantilever leads to a reduced sensor output visibility or output voltage amplitude.

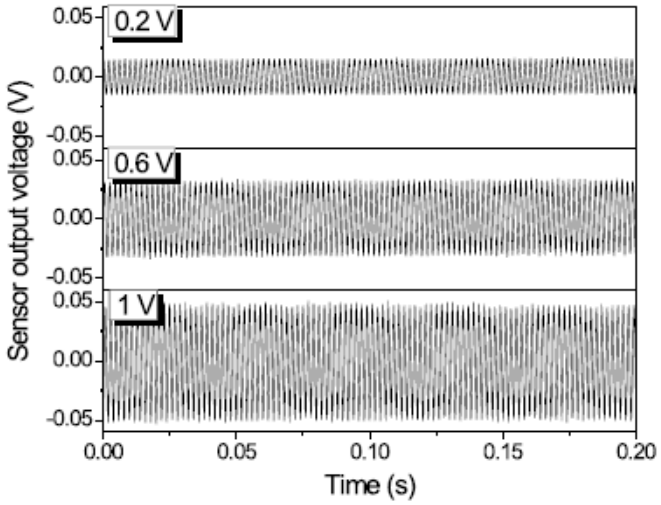

Figure 6.10: The time-domain spectra of the in-line fiber microcantilever sensor when the shaker was driven by sinusoidal signals of 500 Hz for different drive voltages of 0.2 V, 0.6 V, and 1 V, respectively.

Figure 6.10 shows the response of the fiber microcantilever sensor versus the drive voltage amplitude at a certain frequency. All the measurements were performed under the same drive frequency of 500 Hz while the drive voltage of the shaker was changed 0.2 V to 1 V in 0.1 V steps to generate different vibration amplitudes. Figure 6.10 shows the time-domain spectra of the fiber sensor for shaker drive voltages of 0.2 V, 0.6 V, and 1 V, respectively. The corresponding peak-to-peak output voltages are 0.030 V, 0.062 V, and 0.098 V.

In summary, we demonstrated an in-line fiber vibration sensor based on a bend-insensitive fiber that experimentally revealed an extremely wide frequency response from a few Hertz up to tens of kilohertz and a very high SNR up to about 70 dB. Unlike normal amplitude based vibration sensors with problems in alignment and limited reflected light from the vibrating surface, the enclosed microcantilever is immune from external environmental factors such as dust contamination and temperature fluctuation, maintains high mechanical strength, and allows it to be embedded inside structures for monitoring. Furthermore, the high sensitivity and fast response of the microcantilever structure can be integrated into a multiplexing network to realize a quasi-distributed dynamic vibration sensing system. The possibility to adjust the specifications of the microcantilever provides ample opportunities to satisfy requirements from different applications such as intrusion detection and structural health monitoring. Partial metal coating of the microcantilever and the readout fiber core will convert this device into an interferometric sensor with enhanced sensitivity.

6.2.4 Fiber microcantilever chemical sensor

We demonstrates a fiber-based chemical sensor, obtained by etching bend-insensitive fiber (BIF) with 5 % hydrofluoric (HF) acid. The fabrication process of this etched BIF microcantilever can be found in details in section 6.2.3. After 2 and half hours of etching, the tip diameter and the length of the fiber microcantilever was found to be 9 μm and 550 μm, respectively.

This same fiber-based microcantilever has been used as vibration sensor, and discussed in details in section 6.2.3. The experimental set-up for interrogating BIF microcantilever reflection spectrum consists of a Broad Band Source (BBS) and an optical spectrum analyzer to measure the reflected spectrum. The fiber-based microcantilever is the device under test (DUT). The light is coupled to the sensor via a coupler. The reflected light is partially reflected at cantilever-air interfaces(c-a). When the light is

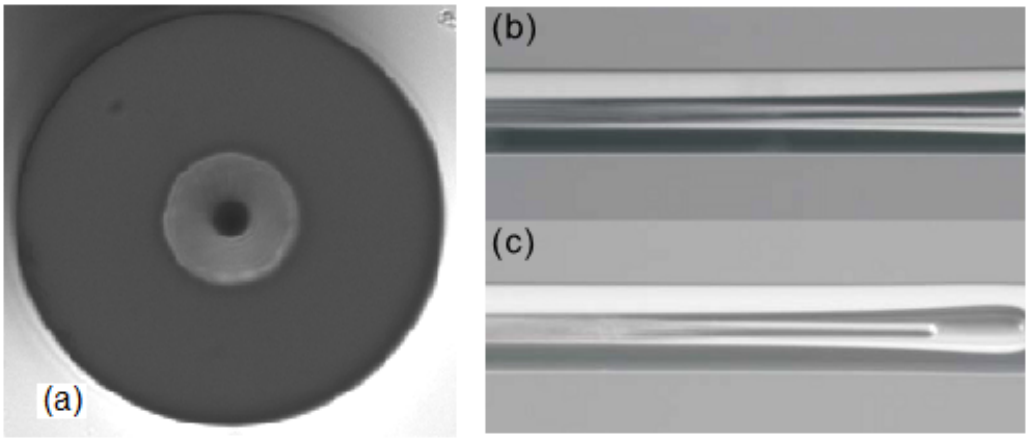

Figure 6.11: (a)Optical microscope image of the transversal cross-section of the BIF after 120 min etching in the 5% HF solution. (b),(c)Optical microscope image of the longitudinal cross-section of the BIF after etching with the 5% HF solution.

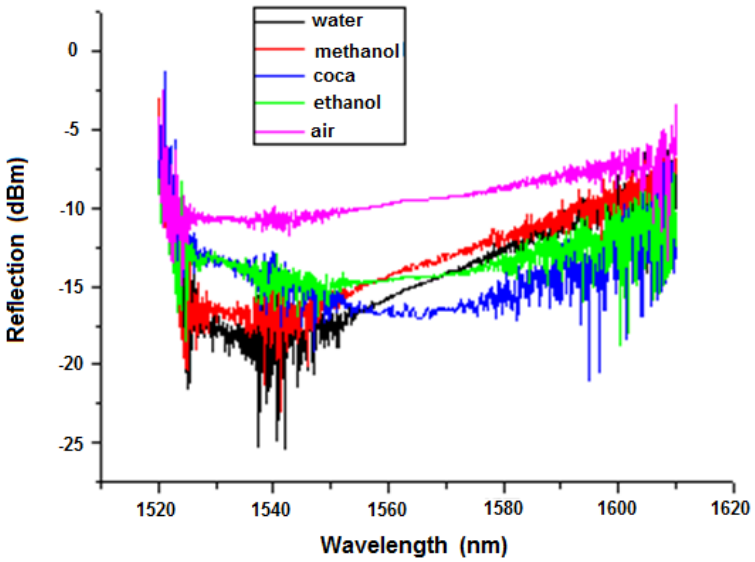

Figure 6.12: Reflection spectra of the fiber microcantilever sensor.

propagating backwards, these signals pass through the same fibre. Finally, reflection spectrum 6.12 is acquired by an optical spectrum analyzer for cantilever-air interfaces(c-a) which is considered as background signal (pink). For a preliminary test, the reflection spectra was acquired for different chemical composition (water, methanol, coca) and cantilever interface. Figure 6.12 shows that the fringes of the reflection spectrum are distinct from each other. Although, the spectrum have very small contrast, we have demonstrated the ability to use this cantilever sensor as chemical sensor. The compact microcantilever hold promises to use extremely small volume of chemicals for detection compared to conventional chemical detection system. For example, while conventional blood cell count tests by automated analyzer or manual process require few mililiters of blood, our proposed fiber-based microcantilever is expected to require few microliters of blood sample. Currently this fiber-based microcantilever is planned to test different concentration of e-coli.

6.3 Femtosecond laser inscribed quasi-random fiber laser

Y. Li, P. Lu, **F. Baset**, Z. Ou, J. Song, A. Alshehri, V. R. Bhardwaj, and X. Bao
Narrow linewidth low frequency noise Er-doped fiber ring laser based on femtosecond laser induced random feedback
Applied Physics Letters **105**, 101105 (2014)

Author contribution

These results come from devising quasi-random fiber, fabricated by F. Baset at Ultrafast Photonics lab, University of Ottawa, ON. Y. Li and P. Lu analysed the characteristics of this quasi-random fiber under supervision of Dr. X. Bao. Y. Li and P. Lu conducted the analysis of the results and F. Baset took SEM and optical microscope images of the microcantilever. Currently, these results are in the process of submission for publishing. Y. Li wrote the first draft of the manuscript.

6.3.1 Introduction

Random lasers with light propagation in amplifying disordered media have been widely investigated in recent years both as a fundamental problem of laser physics and as a promising way to make use of a great variety of materials for engineering applications due to their distinct features [114, 115, 116, 117, 118, 119, 120]. The random laser mechanism depends on the process of multiple scattering with gain, and was first theoretically studied by Letokhov as early as in 1960 [121, 122]. While conventional lasers use an optical cavity to trap light, random laser mechanism uses multiple scattering photons, provided by the amplifying disordered media, to generate laser-like emission [123, 124, 125]. The notable features of random lasers are as follows: there exists a great variety of disordered materials in our nature and it is no longer essential to form a precise optical cavity, unlike conventional lasers. Therefore, lasing in disordered media has been intensively studied both theoretically and experimentally [116, 126].

One of the easiest way to achieve random laser is by pumping bulk materials [127, 128, 129]. Different types of random lasers have been demonstrated in various bulk materials including laser dye with nanoparticles, polymer films and even human tissues. Random lasers in bulk materials generally demand high scattering density and high-power pump pulse to achieve lasing because of the lack of lasing directionality and limited lasing qualities. So, low-dimension random lasers, especially one-dimension random laser are of increased interest and extensively studied[130, 131, 132, 133, 134, 135].

One prominent progress is the Rayleigh-assisted randomly distributed feedback fiber laser [136, 137, 138]. Fiber Rayleigh scattering originates from the structural inhomogeneity in fiber materials, considered as local defects randomly distributed along optical fibers. The fiber geometry provides adequate transverse confinement of light waves and effectively one-dimensional random feedback by the Rayleigh scattering accumulates over a long fiber length. As only a small part of scattered light returns back into the fiber core, the Rayleigh backscattering coefficient is as small as 4.5×10^{-5} in the near-infrared transparency window of fused silica glass fibers. Thus, the two essential (compact configuration and efficient feedback) but incompatible requirements makes the random laser far beyond to challenge the conventional lasers.

In this letter, we demonstrate a rather simple quasi-random fiber laser with comparable performances to a random laser and a commercial fiber laser with fixed cavity. The quasi-random feedback is provided by multiple index modulation points with random spacing precisely located in the fiber core which are inscribed by a high precision

femtosecond laser. The index change is achieved by nonlinear interaction between the fiber core material and the femtosecond pulses. A large number of local Fabry-Perot cavities are formed between two arbitrary modulation points, which endows the proposed laser with some fixed cavity characteristics. The overall effect makes the proposed quasi-random micro-cavities fiber laser comparable with a commercial fiber laser in terms of compact size, linewidth, relative intensity noise and frequency stability. This new type of laser provides a novel choice for the random laser design and propels the development of random lasers in integrated photonics.

6.3.2 Fabrication technique

The same laser set up has been used as in section 6.2.2. 800 nm light from a Ti:Sapphire laser system operating at a repetition rate of 1 kHz and producing 45 fs pulses with a peak energy of 0.5 mJ, was focused at the core of a single mode optical fibre (Corning, SMF-28) by a 0.25 NA microscope objective. The incident pulse energies were measured after the microscope objective and monitored by a calibrated fast photodiode. The position of the laser focus relative to the top and bottom of the fiber surface was accurately determined by imaging the back reflected light with a CCD camera at pulse energies much below the ablation threshold. Then the laser focus was precisely moved to the fiber core for index modification. A single-shot autocorrelator continuously monitored the pulse duration. The pulses were not pre-chirped and the duration was measured to be 70 fs at the back aperture of the objective. The laser-modified regions were characterized by an optical microscope. The laser focal spot radius of 2.7±0.2 μm was obtained from the slope of semi-logarithmic plot of the squared diameter of the modified region measured with the SEM as a function of pulse energy.

The sample fibres are 1 meter long each, cleaved and mounted in a V-groove holder. The jacket of the single mode fiber was removed from the section that interacts with the femtosecond laser. The diameters of the single-mode fiber core and cladding are 8.2 μm and 125 μm, respectively. Each section of the modulated fiber is 1 cm long and the spacing of adjacent modulation points was arbitrarily selected ranging from 10-20 μm. Once the laser was focused at the core with a specific energy, the laser focus was scanned with a specific speed at a plane orthogonal to the fiber core along the entire cross-section (transversal) as shown in Figure 6.13. The optical microscope images in Figure 6.14 (a) and (c) reveals the top view of the modulated region at the fiber core at random separation. The side view in Figure 6.14 (b) and (d) reveals longitudinal cross-section

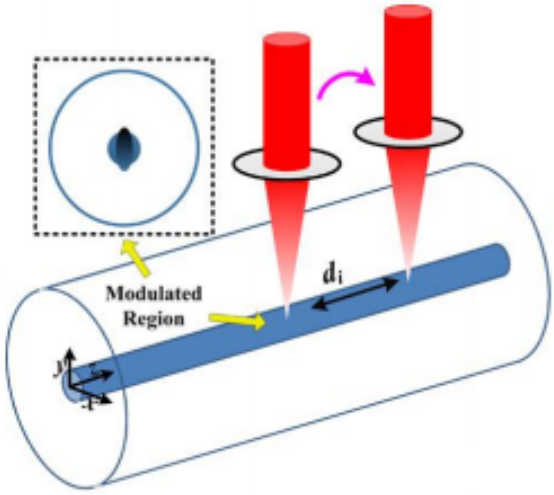

Figure 6.13: Schematic diagram of femtosecond laser writing set up of quasi-random micro-cavities fiber laser. The modulation points are located precisely at the fiber core. The spacing of adjacent modulation points was arbitrarily selected ranging from 10-20 μm.

of the modified fiber core after etching in a solution of 2.5% hydrofluoric acid (HF) for 2 minutes.

The index change at the fiber core is achieved by nonlinear interaction between the fiber core material and the femtosecond pulses. During the fabrication process, different pulse energies and scanning speeds were used to achieve different index modulations. For example, we have samples with 600 nJ writing power, 0.1 mm/s scanning speed and 500 modulation lines with random spacing. In order to improve the reflection intensity, we increased the writing power and decreased the speed to introduce more index changes. The 3 m long fiber consists of 8 pieces of 1 cm long modulated fiber with perfect splicing. The splicing order is based on the reflection intensity with the smallest in the front end and the highest in the output end Figure 6.15.

6.3.3 Laser set up and performance

The laser setup and operation principle are illustrated in Figure 6.16. The feedback part of the proposed laser is provided by 3 m long modulated fiber with 8 sections of modulated region, each 1 cm long. The modulation points located precisely in the fiber

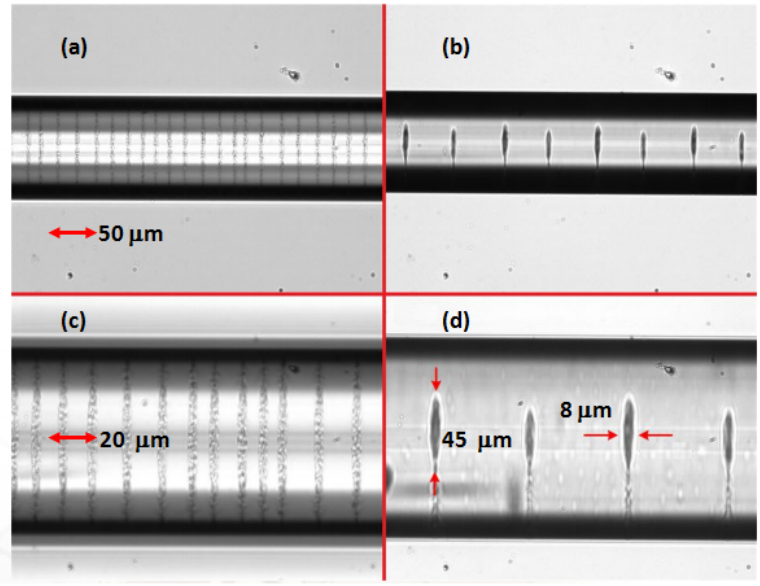

Figure 6.14: Optical microscope image of the modulated fiber. The top view ((a)20X, (c)40X magnification) shows that the multiple modulation points are randomly distributed along the fiber core, across the entire cross-section. The side view ((b)20X, (d)40X magnification) shows the shape of the modulation region within the core.

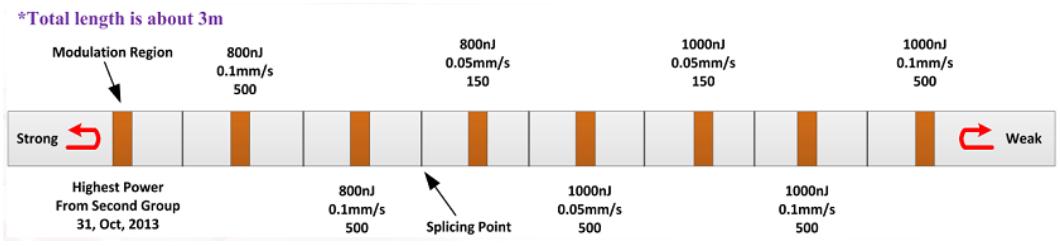

Figure 6.15: Schematic diagram of modulated feedback fiber, composed of 8 pieces of 1 cm long femtosecond laser modulated fiber spliced together. Each section of the fiber is modulated with variable laser writing speed, laser power and variable cavity length (variable mode separation)precisely at the fiber core, across the whole cross-section. The order of the spliced samples is based on the reflection intensity with the smallest in the front and the highest at the end with a total length of about 3 m.

core, were modulated by a femtosecond laser with random spacing, ranging from 10–20 microns with different writing speed and energy. Therefore, these modulation lines are treated as reflection centres with random spacing. The purpose of splicing the 8 pieces of randomly modulated samples together based on the reflection intensity is to make sure that each modulation point weigh equally in the laser operation. The gain is provided by an erbium-doped fiber amplifier (EDFA) and two polarization controllers are employed to ensure orthogonal states of polarization at input and output ends of the EDFA to minimize interference related background noise, as shown in 6.16. One isolator in the ring enforces a unidirectional operation and the other one at the output end ensures that the feedback is due only to the modulated fiber.

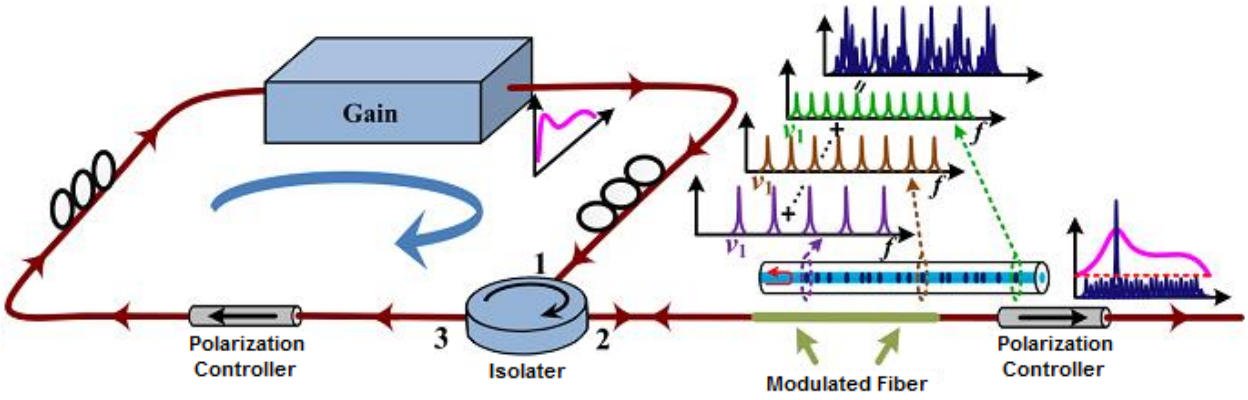

Figure 6.16: Schematic diagram of the laser set up with the femtosecond laser modulated feedback fiber. Each feedback point of the femtosecond laser modulated fiber together with the ring, form a fix cavity with multi-longitudinal mode operation. Multiple feedback points with random spacing play the role of a randomly distributed mirror and the output laser can be considered as the superposition of multiple fix cavity lasers with variable cavity length, and thus variable mode separation. Due to mode competition, only the mode at the gain maximum will obtain enough gain and conquer the cavity loss becoming the lasing mode. The random micro-cavities incorporated with the mode competition phenomenon act as the lasing mode selection element.

Conventional fiber lasers usually employ an optical filter as the wavelength selector and introduce different kinds of mode suppression methods to achieve desired laser output. For the quasi-random micro-cavities fiber laser, the supported lasing mode depends critically on the local Fabry-Perot interferometer (FPI) as well as on the gain profile. The gain itself plays the role of selective wavelength component and mode selection

simultaneously. The quasi-random micro-cavities fiber laser can be considered as the superposition of multiple fixed cavity lasers with variable cavity length, and thus variable mode separation. The local FPIs increase the effective cavity length for every individual modulation points, leading to a huge number of extended modes with decreased mode separation and attenuated magnitude, overlapping with each other. Hence, when an uneven gain profile is added, only the modes near the gain maximum with relative high magnitude will at first cancel the cavity loss and become lasing mode through mode competition effect. Due to the spatially discrete modulation points, the modes are discrete in frequency domain which is quite different from the mode structure of Rayleigh-assisted random fiber lasers. When the Rayleigh backscattering is applied as the feedback, on the contrary, multiple modes will be activated at the same time, which is fundamentally determined by the negligibly small differences between neighbouring scattering centres and the continuous mode structure.

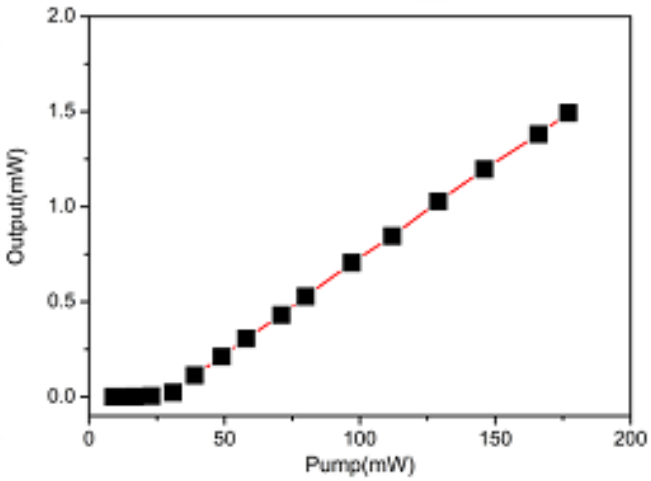

Figure 6.17: Quasi-random micro-cavities fiber laser output power as a function of the pump power. The pump is provided by an EDFA with maximum power of 178 mW. The threshold is 27 mW. The slope efficiency is 1%.

Figure 6.17 clearly demonstrates lasing with a threshold pump power of ∼27 mW and a typical linear growth of the generated output power above threshold. The max output power is 1.5 mW which is limited mainly by the pump laser. Although the slope efficiency is as small as 1% considering the especially broad gain spectrum, the actual slope efficiency is believed to be higher.

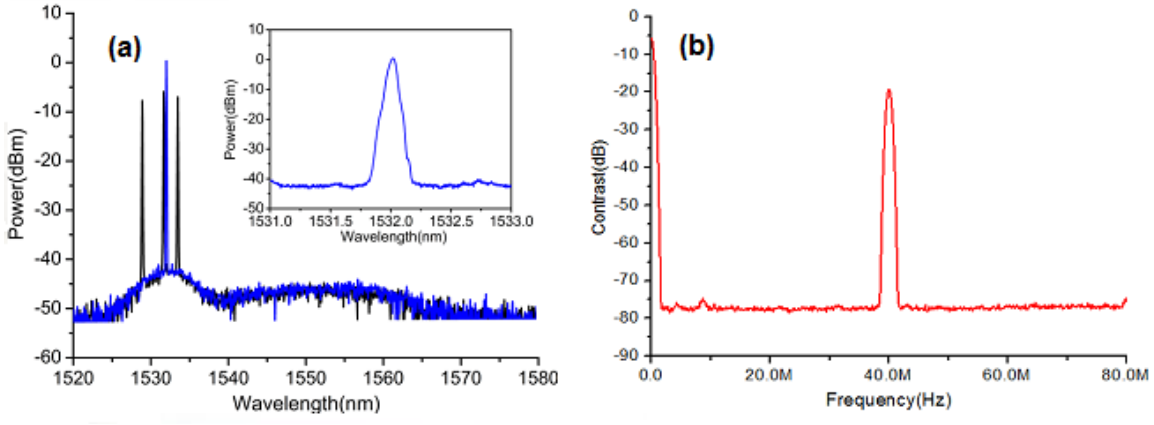

Figure 6.18: (a)Quasi-random micro-cavities fiber laser gain profile. One wavelength peak at the maximum of the gain profile. The blue line represents single lasing mode, while black line represents multiple lasing mode. Inset shows the enlarged figure. The central wavelength is 1532.02 nm and the contrast is 40.6 dB. (b)The peak contrast. There is only one peak with contrast as high as 60 dB in 80 MHz span.

As described above, the output features are associated with the gain profile. In our setup, the gain is provided by an EDFA with the max power of 178 mW. The maximum of the amplified spontaneous emission (ASE) spectrum is located around 1530 nm corresponding to the spontaneous energy levels transition of electrons of Er^{3+}. Figure 6.18(a) shows one stable wavelength peak, centred at 1532.02 nm, with contrast as high as 40.7 dB is localized near the ASE gain maxima. In the radio-frequency spectra, one pronounced peak, $\sim$ 60 dB above the noise level, instead of the mode beatings with spacing corresponding to the round trip in the cavity is observed, leading to a stationary single-mode laser oscillation. In the laser setup (Figure 6.16), there is no filter in the cavity to stabilize the output, so the mode hopping will be inevitable. Sometime it is single-mode lasing (blue), however sometime is multiple modes lasing (black). Figure 6.18(b) shows,there is only one peak with contrast as high as 60 dB in 80 MHz span. We approximately estimated the linewidth of the quasi-random micro-cavities laser by the commonly used delayed self-heterodyne interferometric technique. The 3-dB Lorentzian linewidth is calculated to be 2.1 kHz.

6.3.4 Results

Figure 6.19 shows relative intensity noise (RIN)comparison between different lasers. In Rayleigh-assisted random fiber lasers, tens of kilometers of fibers are usually required to provide adequate feedback due to the low RBS coefficient of fused silica glass fibers in their near-infrared transparency widow. Since silica fiber is an intrinsic disordered medium that contains numerous scattering centres occurring at very short and irregular intervals, incorporating such extremely long fibers into a laser configuration will promote many mode competitions, and thus higher intensity noise. Furthermore, the long laser configuration is sensitive to external perturbations such as sound wave, mechanical vibration and temperature variation. The feedback fiber of quasi-random micro-cavities fiber laser is only a meter long. So the proposed laser is potentially compact in size. And the finite mode number and discrete mode structure make the mode competition effect less intense than the Rayleigh random laser. From this point of view, the quasi-random micro-cavities fiber laser should have a lower relative intensity noise in comparison with the Rayleigh random laser as shown in Figure 6.19(a). The RIN of the proposed laser is 10–20 dB lower than the Rayleigh random laser and has a comparable value to the commercial fiber laser with an integrated electrical feedback mechanism to stabilize its output. In contrast for a normal cavity laser where the frequency noise is higher due to lack of averaging, both the proposed laser and the commercial fiber laser have the RIN as low as the background noise in our lab conditions [139]. It should also be noted that, the RIN spectrum of the proposed laser exhibits some discrete peaks which result from the competition among those discrete modes.

Conventional fiber lasers with a Fabry-Perot cavity or ring cavity are not able to achieve the fundamental limit to frequency noise, which is known as the Schawlow-Townes limit attributed by the spontaneous emission [140]. The frequency noise induced by thermal fluctuation of laser cavity is inversely proportional the cavity length [141]. The changes of the effective cavity length will be negligibly small compared to a long fiber cavity length. The random laser with Rayleigh distributed feedback mechanism gives a Lorentzian envelope over the original frequency noise, leading to efficient suppression at high frequency ranges. Therefore, the Rayleigh random laser is found to have the lowest frequency noise. In our case, Figure 6.19(b) clearly shows a significant suppression of the thermal noise due to the quasi-random feedback, providing a roll-off at about 1 kHz. The relative high frequency noise below 1 kHz is determined by the gain media, since the EDFA exhibits a fluorescence relaxation time in the millisecond-scale.

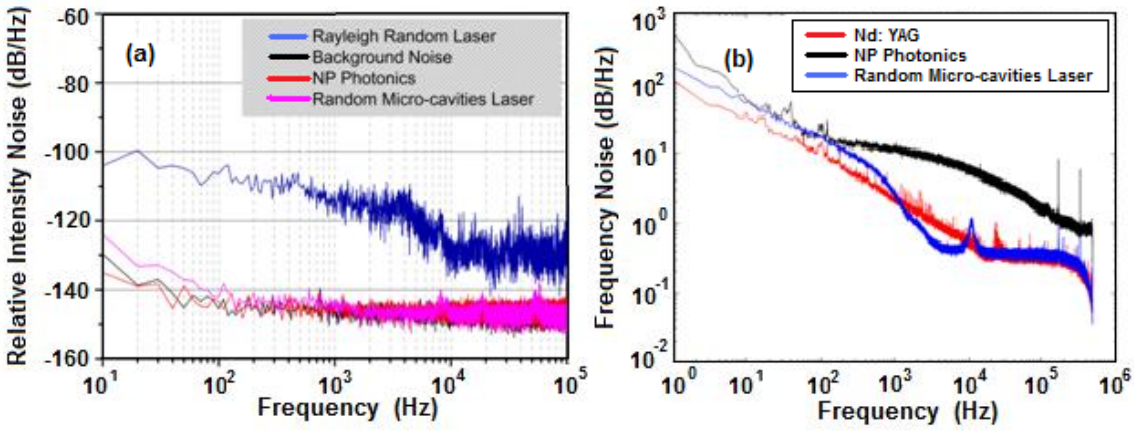

Figure 6.19: (a)The Rayleigh random laser has high density of mode numbers, which promotes many mode competitions, and thus higher intensity noise. And the long cavity length is easily affected by external perturbations. The quasi-random micro-cavities laser has a discrete mode structure and compact laser configuration.(b)Frequency noise comparison between different lasers.

In conventional fiber laser with a Fabry-Perot cavity or ring cavity, the frequency instability is caused by the fluctuation of the effective cavity length through thermal noise-induced perturbations of the silica fibers. This frequency instability is reflected by the central frequency jitter of the lasing mode. Active or passive frequency stabilization techniques have to be introduced to stabilize the laser output. In random fiber lasers, modes superimposed in a large scale of frequency domain will significantly average such a fluctuation, resulting in a low frequency jitter. Although the femtosecond-modulated-fiber is not an intrinsic disordered medium, the inscribed random micro-cavities has the random feature which is characterized by the frequency jitter as deposited in Figure 6.20. Figure 6.20 gives the frequency jitter of the beat signals which can reflect the actual frequency jitter of a laser to some extent. The commercial reference fiber laser has a frequency jitter within ± 20 kHz in the ~ 1.44 h measurement. In contrast, the quasi-random micro-cavities fiber laser almost has the same frequency jitter with the reference. To quantitatively characterize the laser frequency stability, the Allen standard deviations within 100 s are calculated to be 1.80510^{-12} and 1.82710^{-12} for the proposed laser and the NP Photonics reference laser, respectively. The Allen standard deviation is slightly smaller than the reference laser, indicating a high frequency stability of the quasi-random micro-cavities fiber laser.

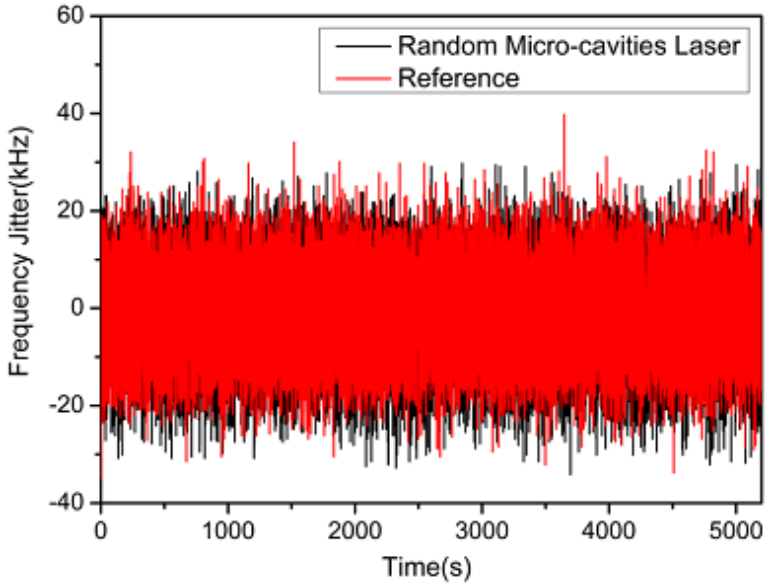

Figure 6.20: Frequency jitter of the quasi-random micro-cavities laser. The frequency jitter of the proposed quasi-random microcavities fiber laser was measured at night when the external perturbations were relative small. The measurements took 5200 s. The Allen standard deviation within 100 s is calculated to be 1.805×10^{-12} and 1.827×10^{-12} for the proposed laser and the NP Photonics reference laser, respectively.

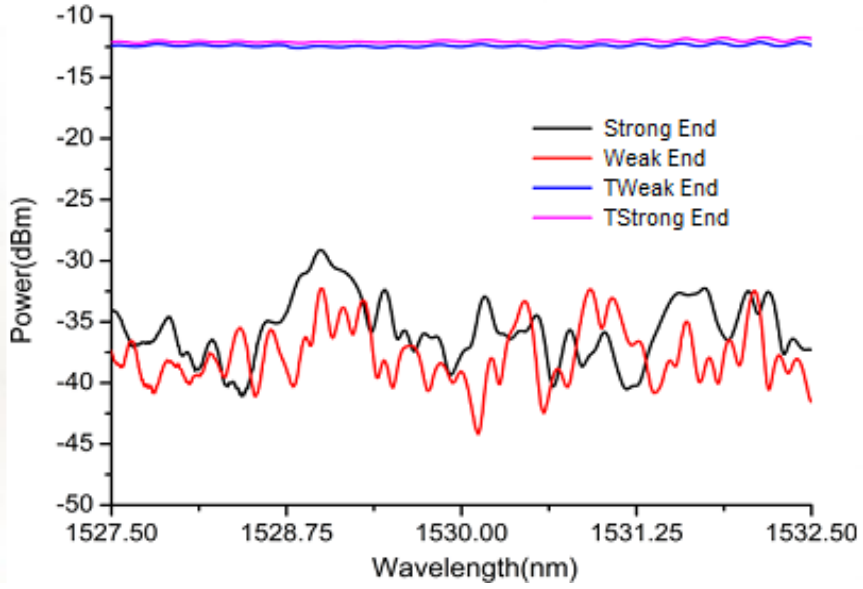

Figure 6.21: Interference from the reflection spectra of the feedback fiber.

Figure 6.21 shows the reflection spectra of the feedback fiber and confirms the existence of interference. A broadband light source (BBS), a circulator and the optical spectrum analyzer (OSA) were used to measure the reflection from the femtosecond laser modulated fiber. From the figure, the black and red curves are the normalized reflection intensity which means, if 0 dBm light is launched, the overall reflection intensity will be approximately -35 dBm. The other two curves (blue and pink) are the transmission spectra. It exhibits how much light is lost. The difference between the black and red curves is due to the different modulation parameters. The reflection is the summation of eight samples with different modulation parameters. Generally, the higher power and lower speed corresponds to the higher index modulation and thus higher reflection. So when all eight samples are spliced together, the reflection from two ends will be different. The strong end and weak end represents as it is referred in Figure 6.15. The interference present in the reflection spectra can be better explained in terms of the Fabry-Perot. However, the transmission loss is about 12 dB in our proposed fiber. To further understand the reflection spectra, it is necessary to further study what really happens in the feedback fiber.

Figure 6.22(a) and (b) show the simulations based on the scanning electron microscope (SEM) images of the unmodulated and modulated SMF, respectively. Since the nonlinear absorption process is independent of the material, the core and cladding have the same Δn in our simulations. Therefore, most of the energy is still confined in the core. But part of the energy will couple to high-order modes in the waveguide. Also, part of the energy from core mode will couple to high order cladding modes. Figure 6.22(c) shows power in the core region. The red curve region contains 24 modulation lines. Since the effective refractive index of the fundamental mode at the modulation line will change due to the index modulation, power from the core mode will couple to high order cladding modes. The power drop from 0.72 to 0.7 is visible at the inset of Figure 6.22(c). On the other hand, multiple scattering will introduce interference effect. In Figure 6.22(c), there exists a large number of low-finesse interferometers similar to Mach-Zehnder (core mode-cladding modes) and Fabry-Perot (core mode-core mode) as demonstrated in the diagram, which results in power fluctuation. And this also explains the interference patterns in Figure 6.21.

Although the simulation proves the presence of coupling and interference between core mode and cladding modes, it can not explain the high transmission loss. The reason is, we simply took the index modulation into consideration but neglected the structural inhomogeneity. We introduced a scattering model to explain the structural

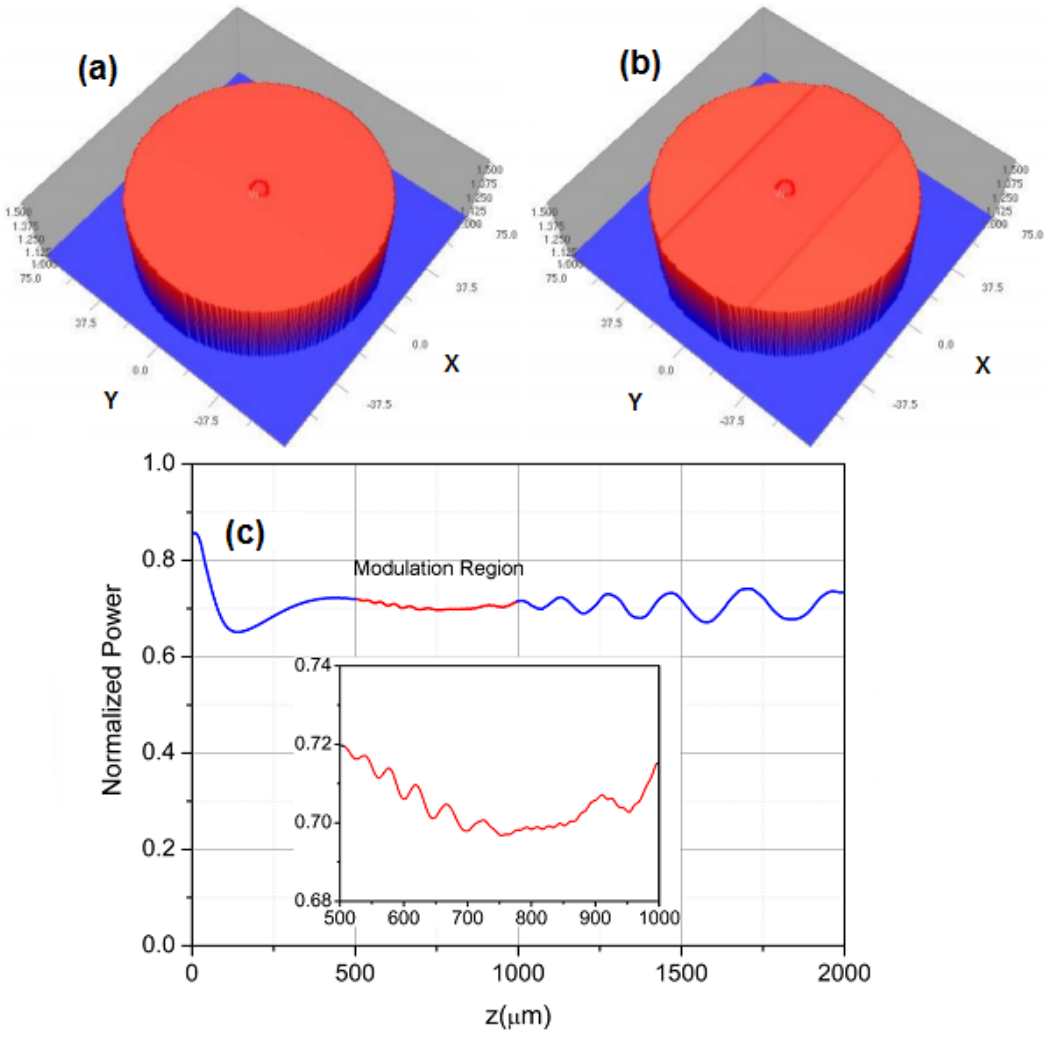

Figure 6.22: Simulations based on the SEM images of the (a)unmodulated and (b)modulated SMF and, (c)Power in the core region. Modulation region contains 24 special waveguides.

inhomogeneity within the modulated region. The model takes into account the following facts,
a)The index modulation surface is not ideal plane but curved surface in Z direction;
b)The index distribution in the modulation region is spatially inhomogeneous;
c)The threshold power E^{th} is around 600 nJ. Increasing the E beyond the threshold (for example,800nJ and 1mJ pulse energy were used for index modulation) will lead to nanocrack formation [142].
The resultant of all these facts associated with the proposed scattering model is, the modulation regions becomes highly scattered.

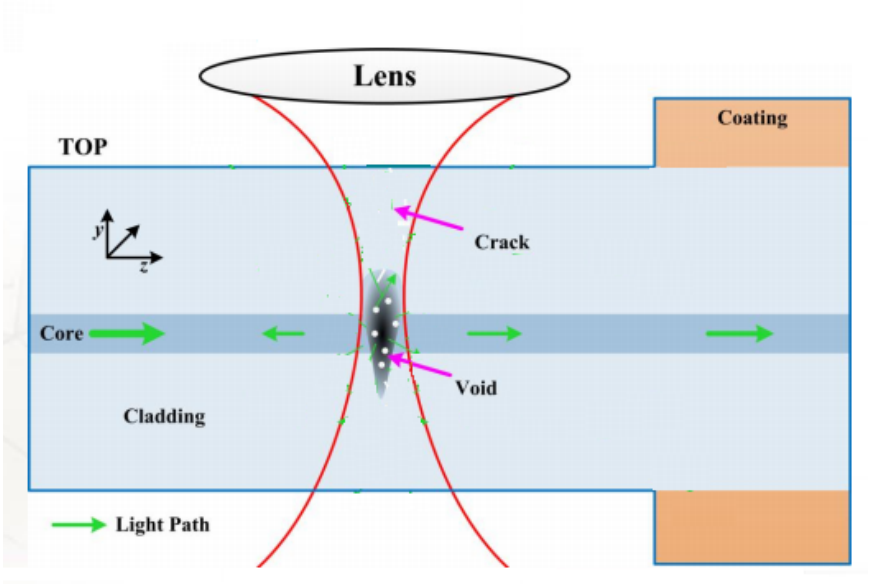

Figure 6.23: Schematic diagram of the scattering model. The modulation region is spatially inhomogeneous and contains irregular cracks and voids (some elements have been greatly exaggerated).

6.3.5 Discussion

At present, for the first time a quasi-random fiber laser with the performances comparable to commercial fiber laser is reported. We have experimentally demonstrated a quasi-random micro-cavities laser with both features from the random lasers and the conventional fix cavity lasers, characterized by simple configuration and potentially compact size, single mode narrow linewidth (2.1 kHz), low RIN, high frequency stability and

truly random feedback. Simulation shows that high-order modes are interfering with the core mode. High transmission loss experienced by this quasi-random fiber laser is due to leaky modes and absorption, and explained by a proposed scattering model. Based on our analysis, pulse energy used for the fs laser writing should be less than the threshold power E^{th} (600 nJ) and the single mode fiber should be replaced with bend-insensitive fiber to reduce the overall transmission loss. We believe, our work will provide a new choice for the realization of compact random laser design and practical applications.

Chapter 7

Conclusions

7.1 Conclusions and future outlook

The interaction of intense laser pulses with transparent materials has remained an active area of research since the advent of lasers. Technology based on femtosecond laser-dielectric interaction holds great promises for material micro/nano structuring, that has become the backbone of rapidly expanding application areas in emerging technologies such as, telecommunications, optics, electronics, biomaterials, and medicine. Understanding and manipulating such interaction would provide an inexpensive yet precise processing technique that can develop and structure materials with a high degree of controllability, accuracy, and reduced residual damage. Despite a long history of the experimental and theoretical considerations involved in focusing short pulses into transparent materials, there remain some open questions. Some issues are addressed in this thesis, others remain unresolved, and the work presented here will lead to some new queries.

The work conducted in this thesis is original research that has contributed to the field of dielectric ablation and modification in micro/nano-scale with femtosecond laser pulses. This research work has resulted in several new insights into the physical mechanisms that occur during the interaction of intense laser fields with transparent bulk dielectrics. The publications in this thesis serve to establish femtosecond laser-dielectric interaction as an effective technique for surface ablation and material modification with micro/nano resolution. This final chapter will review some of the key conclusions of this thesis and briefly discuss areas where further work is sorely required.

For single pulse ablation, this thesis has presented the first ever experimental evi-

dence that surface swelling is the first step in interaction of intense femtosecond pulses with bulk dielectrics, followed by material ejection and ablation with increased fluence. At approximately one and a half times the threshold fluence for surface swelling, the ablated holes become clean; below that range surface swelling dominates and is independent of laser polarization whereas, above that range ablation mechanism dominates, but polarization effects can become prominent in PMMA. Molecular dynamics simulations provide physical insight into swelling dynamics showing that void formation and material swelling are important mechanisms of temperature equilibration at the surface of the laser-heated sample. For pulse energies beyond the threshold values, the polarization dependence becomes prominent in the form of elongated craters (for stationary focus, with linearly and elliptically polarized light) and quasi-periodic structures (for line ablation). Experimental results were compared with numerical studies, carried out by 3D finite difference time domain simulation of the interaction of intense light pulses with bulk PMMA. Simulations show that the elongation of the ablation crater arises from the local field enhancement during light-plasma interaction. In case the initial plasma density is over-critical, field enhancement occurs parallel to the laser polarization (for surface ablation) resulting in elongated structures, whereas, for under-critical plasma density, the field enhancement occurs perpendicular to the laser polarization (for internal modification) resulting in periodic structures. The experimental results are in good agreement with numerical simulations, demonstrating that the polarization-dependent ablation effects can be minimized by using either circularly polarized light or, pulse energies close to ablation threshold.

For multiple pulse ablation, the ablation craters become polarization independent. For the first time, the formation of nano-pillar was observed within the ablation crater on bulk PMMA surface, when irradiated by two fs pulses at a certain delay with energies below single shot ablation threshold. The experimental evidence showed that, with further increase in energy the nano-pillar vanished and the structure within the ablation crater appeared as splash of object in liquid. The 2D molecular dynamics simulation provided an insight into the possible mechanism of this nano-pillar formation exposing the fact that, the presence of the first laser pulse is crucial as it defines the boundaries from which the shockwave induced by the second laser pulse reflects and causes density pinching in the middle of the interaction region that rapidly pushes out the molten material towards the surface. For multiple pulse ablation experiments, it was observed that the fs laser induced porosity on PMMA surface depends on pulse energy, number of shots and scan speeds. The number of pores and their size increase with pulse energy.

Femtosecond laser induced porosity in PMMA enables surface structuring on micro- and nano scale, holding promises to promote cell adhesion and proliferation at the polymer-tissue interface for better implant union.

The applied section of this thesis demonstrated an in-line fiber vibration sensor based on an enclosed suspended microcantilever within a bend-insensitive fiber, integrated with a readout fiber. This novel vibration sensor is immune from external environmental factors and experimentally exhibits an extremely wide frequency response from a few hertz up to tens of kilohertz and a very high SNR ∼70 dB while maintaining high mechanical stability. Moreover, a rather simple quasi-random fiber laser was fabricated by direct laser writing at single mode fiber core with random spacing. This novel quasi-random micro-cavities fiber laser can be characterized by potentially compact size, narrow line width, low relative intensity noise and high frequency stability, exhibiting features from both random lasers and the conventional fix cavity lasers.

The single and multiple pulse ablation and modification experiments were performed with femtosecond pulses, ∼45 fs in duration, centered around 800 nm. In addition to extending the experiments to different materials, several additional possibilities for further research can be considered. Although a great amount of data was gathered from the interaction of light with PMMA, there exist some open questions. Besides post mortem analysis of the ablation crater by single pulse irradiation, detailed time-resolved experiments extending to longer times will provide access to probe more details on swelling dynamics. Application of a time resolved technique would be a noteworthy prequel to the post mortem analysis studies presented here. To gain further insight into the nonlinear interaction of light with matter, the molecular structure of PMMA should be taken into account with sample sizes comparable to the laser spot size, which can be achievable through large scale simulation. Further experiments on polarization dependent study for longer pulse durations would provide more explanations of less significant role of light-plasma effects during the interaction.

Also, finding threshold values using different pulse durations, electric fields, and polarizations will increase the accuracy of the data. Another interesting perspective could be repeating the experiments done throughout this thesis using different laser wavelengths in order to compare it to the results obtained at 800 nm. The waveguides created within the bulk of PMMA are required to be explored either by cutting the PMMA samples along the direction of the waveguides or by etching the PMMA samples in order to have access to the structures within the waveguide. To find out the best parameters for efficient waveguides, tests should be performed by sending light through waveguides and

monitoring the output signal using different light polarizations as well as different beam shapes.

The proposed in-line fiber microcantilever structure with high sensitivity and fast response, is capable to open the possibility of integrating into a multiplexing network to realize a quasi-distributed dynamic vibration sensing system. The unique advantage of adjusting the specifications of the microcantilever should be tested to be exploited as intrusion detection and structural health monitoring application. On-going experiments on this fiber microcantilever have already shown prospects as chemical sensor, and its application can be extended as temperature sensor as well. The vibration sensing capabilities already established for this platform shows prospects to take advantage from partial metal coating of the microcantilever and the readout fiber core, which will convert this device into an interferometric sensor with enhanced sensitivity. Although, special features (low RIN, narrow line width) of quasi-random micro-cavities laser demonstrated satisfactory performances, ongoing projects are focused on improving the waveguide qualities to overcome limitations, such as leaky modes and transmission, and also using bend-insensitive fiber instead of SMF to confine the energy within the core and inner cladding region.

The research work presented in this thesis were greatly exploratory in nature and improved our ability to interpret the material properties and the ionization process of femtosecond laser-dielectric interaction. These experiments serve to identify subtle effects that help to understand the underlying physics of femtosecond laser-dielectric interaction. To address the current unresolved issues for more complete understanding of the ablation and modification process, it is required to constantly improve the experimental techniques, develop new analytical tools and extend theoretical work. The author hopes that the research work during her PhD project presented in this thesis, will provide an excellent foundation for future research in this field and will help to develop a variety of application in microscopy and photonics.

Appendix A

Glossary and terms

AFM Atomic Force Microscopy
BA Back Aperture
BBO Beta Barium borate
BBS Broad Band Source
BIF Bend-Insensitive Fiber
CCD Charged-Coupled Device
CW Continuous Wave
DAQ card Data Aquisition card
EDFA Erbium-Doped Fiber Amplifier
FDTD Finite Difference Time Domain
FPI Fabry-Perot Interferometer
FWHM Full Width at Haft Maximum
GDD Group Delay Dispersion
GVD Group Velocity Dispersion
HAZ Heat Affected Zone
HF Hydrofluoric Acid
IP Ionizing Potential
IR Infrared
MD Molecular Dynamics
MPI Multiphoton Ionization
NA Numerical Aperture
ND Neutral Density
OM Optical Microscope

OPA Optical Parametric Amplifier
OSA Optical Spectrum Analyzer
PMMA Poly(methyl methacrylate)
PMT Photomultiplier Tube
RIN Relative Intensity Noise
SEM Scanning Electron Microscope
SMF Single Mode Fiber
SH Second Harmonic
UV Ultra-Violet

Appendix B

Permission for reproduction of work

Paper presented in Section 4.2 was previously published in the Optics Express. The Optical Society has granted me the rights to reproduce this article in my Thesis. I hereby grant University of Ottawa and the Library and Archives Canada the non-exculsive right to reproduce this article as part of the present Thesis.

Paper presented in Section 4.3 was previously published in the New Journal of Physics. The Institute of Physics has granted me the rights to reproduce this article in my Thesis. I hereby grant University of Ottawa and the Library and Archives Canada the non-exculsive right to reproduce this article as part of the present Thesis.

Paper presented in Section 5.3 was previously published in the Applied Surface Science journal. The Elsevier journal has granted me the rights to reproduce this article in my Thesis. I hereby grant University of Ottawa and the Library and Archives Canada the non-exculsive right to reproduce this article as part of the present Thesis.

Results presented in Section 6.2.3 were previously published in the Applied Physics Letters journal. The American Institute of Physics has granted me the rights to reproduce this article in my Thesis. I hereby grant University of Ottawa and the Library and Archives Canada the non-exculsive right to reproduce this article as part of the present Thesis.

Figure 2.2 and 2.7 used in Chapter 2 were results published by others in the Applied Physics A: Materials Science and Processing and the Physical Review Letters, respectively. The Springer and the American Physical Society have granted me the rights to reprint these images in my Thesis. I hereby grant University of Ottawa and the Library and Archives Canada the non-exculsive right to reprint these images as part of the present Thesis.

Permission for reproduction of work

Permission from The Optical Society

Dear Farhana Baset,

Thank you for contacting The Optical Society.

Because you are the author of the source paper from which you wish to reproduce material, OSA considers your requested use of its copyrighted materials to be permissible within the author rights granted in the Copyright Transfer Agreement submitted by the requester on acceptance for publication of his/her manuscript. It is requested that a complete citation of the original material be included in any publication. This permission assumes that the material was not reproduced from another source when published in the original publication.

Please let me know if you have any questions.

Kind Regards,

Susannah Lehman

Susannah Lehman

September 24, 2014

Authorized Agent, The Optical Society

Permission from Institute of Physics

Dear Farhana Baset,

Thank you for your email and for taking the time to seek this permission.

When you assigned the copyright in your article to IOP, we granted back to you certain rights, including the right to include the article within any thesis or dissertation.

Therefore, please go ahead and make what use you wish of the content of the article.

The only restriction is that if, at a later date, your thesis were to be published commercially, further permission would be required.

Please let me know if you have any further questions.

In the meantime, I wish you the best of luck with the completion of your dissertation.

Kind regards,

Lucy Evans

Publishing Assistant

IOP Publishing

Please note: We do not usually provide signed permission forms as a separate attachment. Please print this email and provide it to your publisher as proof of permission.

Permission for reproduction of work

Permission from Elsevier

Dear Farhana,

Permission is covered by the rights you retain as an Elsevier journal author as outlined at http://www.elsevier.com/journal-authors/author-rights-and-responsibilities, which include Inclusion in a thesis or dissertation, provided that proper acknowledgement is given to the original source of publication. Should you require any further clarification, please let me know.

Best of luck with your thesis.

Thank you,

Laura

Laura Stingelin

Permissions Helpdesk Associate

Elsevier

[redacted]

Suite 1800

Philadelphia, PA 19103-2899

T: [redacted]

F: [redacted]

E: [redacted]@elsevier.com

Questions about obtaining permission: whom to contact? What rights to request?

When is permission required? Contact the Permissions Helpdesk at:

+[redacted] [redacted]@elsevier.com

Permission from American Institute of Physics

Dear Dr. Baset:

Thank you for requesting permission to reproduce material from AIP Publishing LLC publications.

Material to be reproduced:

Ping Lu, Yanping Xu, Farhana Baset, Xiaoyi Bao, and Ravi Bhardwaj, "In-line fiber microcantilever vibration sensor", Applied Physics Letters, 103, 211113 (2013).

For use in the following manner:

Reproduced in your PhD thesis for submission to the University of Ottawa. In addition, an irrevocable, nonexclusive license is also granted to the University of Ottawa and to the National Library of Canada to reproduce this material as a part of the thesis.

Permission is granted subject to these conditions:

1. AIP Publishing LLC grants you non-exclusive world rights in all languages and media. This permission extends to all subsequent and future editions of the new work.

2. The following copyright notice must appear with the material (please fill in the information indicated by capital letters):

"Reproduced with permission from [FULL CITATION]. Copyright [PUBLICATION YEAR], AIP Publishing LLC."

When reusing a full article, the copyright notice must be printed on the first page of the reprinted article or book chapter. When reusing figures, photographs, covers, or tables, the notice may appear in the caption, in a footnote, or in the reference list.

In cases where the new publication is licensed under a Creative Commons license, the full copyright notice as stated above must appear with the reproduced material.

3. If the material is published in electronic format, we ask that a link be created pointing back to the abstract of the article on the journal website. This can be accomplished through the use of the article's DOI.

4. This permission does not apply to any materials credited to sources other than the copyright holder.

Please let us know if you have any questions.

Permission for reproduction of work

Sincerely,

Susann Brailey

Manager, Rights and Permissions

AIP Publishing LLC

[redacted]

Suite 300

Melville, NY 11747-4300

cid:i[redacted]

Tel.[redacted]

[redacted]@aip.org

Permission from Springer

SPRINGER LICENSE
TERMS AND CONDITIONS

Oct 14, 2014

This is a License Agreement between Farhana Baset ("You") and Springer ("Springer") provided by Copyright Clearance Center ("CCC"). The license consists of your order details, the terms and conditions provided by Springer, and the payment terms and conditions.

All payments must be made in full to CCC. For payment instructions, please see information listed at the bottom of this form.

License Number	3474491390555
License date	Sep 22, 2014
Licensed content publisher	Springer
Licensed content publication	Applied Physics A: Materials Science & Processing
Licensed content title	Femtosecond, picosecond and nanosecond laser ablation of solids
Licensed content author	B. N. Chichkov
Licensed content date	Jan 1, 1996
Volume number	63
Issue number	2
Type of Use	Thesis/Dissertation
Portion	Figures
Author of this Springer article	No
Order reference number	None
Original figure numbers	Fig. 1 and Fig. 2
Title of your thesis / dissertation	Micro/nano-scale Manipulation of Material Properties
Expected completion date	Sep 2014
Estimated size(pages)	145
Total	0.00 CAD
Terms and Conditions	

Permission for reproduction of work

Introduction
The publisher for this copyrighted material is Springer Science + Business Media. By clicking "accept" in connection with completing this licensing transaction, you agree that the following terms and conditions apply to this transaction (along with the Billing and Payment terms and conditions established by Copyright Clearance Center, Inc. ("CCC"), at the time that you opened your Rightslink account and that are available at any time at http://myaccount.copyright.com).

Limited License
With reference to your request to reprint in your thesis material on which Springer Science and Business Media control the copyright, permission is granted, free of charge, for the use indicated in your enquiry.

Licenses are for one-time use only with a maximum distribution equal to the number that you identified in the licensing process.

This License includes use in an electronic form, provided its password protected or on the university's intranet or repository, including UMI (according to the definition at the Sherpa website: http://www.sherpa.ac.uk/romeo/). For any other electronic use, please contact Springer at ([redacted]@springer.com or [redacted]@springer.com).

The material can only be used for the purpose of defending your thesis limited to university-use only. If the thesis is going to be published, permission needs to be re-obtained (selecting "book/textbook" as the type of use).

Although Springer holds copyright to the material and is entitled to negotiate on rights, this license is only valid, subject to a courtesy information to the author (address is given with the article/chapter) and provided it concerns original material which does not carry references to other sources (if material in question appears with credit to another source, authorization from that source is required as well).

Permission free of charge on this occasion does not prejudice any rights we might have to charge for reproduction of our copyrighted material in the future.

Altering/Modifying Material: Not Permitted
You may not alter or modify the material in any manner. Abbreviations, additions, deletions and/or any other alterations shall be made only with prior written authorization of the author(s) and/or Springer Science + Business Media. (Please contact Springer at ([redacted]t@springer.com or [redacted]@springer.com)

Reservation of Rights
Springer Science + Business Media reserves all rights not specifically granted in the combination of (i) the license details provided by you and accepted in the course of this licensing transaction, (ii) these terms and conditions and (iii) CCC's Billing and Payment terms and conditions.

Copyright Notice:Disclaimer
You must include the following copyright and permission notice in connection with any reproduction of the licensed material: "Springer and the original publisher /journal title, volume, year of publication, page, chapter/article title, name(s) of author(s), figure number(s), original copyright notice) is given to the publication in which the material was originally published, by adding; with kind permission from Springer Science and Business Media"

Warranties: None

Example 1: Springer Science + Business Media makes no representations or warranties with respect to the licensed material.

Example 2: Springer Science + Business Media makes no representations or warranties with respect to the licensed material and adopts on its own behalf the limitations and disclaimers established by CCC on its behalf in its Billing and Payment terms and conditions for this licensing transaction.

Indemnity
You hereby indemnify and agree to hold harmless Springer Science + Business Media and CCC, and their respective officers, directors, employees and agents, from and against any and all claims arising out of your use of the licensed material other than as specifically authorized pursuant to this license.

No Transfer of License
This license is personal to you and may not be sublicensed, assigned, or transferred by you to any other person without Springer Science + Business Media's written permission.

No Amendment Except in Writing
This license may not be amended except in a writing signed by both parties (or, in the case of Springer Science + Business Media, by CCC on Springer Science + Business Media's behalf).

Objection to Contrary Terms
Springer Science + Business Media hereby objects to any terms contained in any purchase order, acknowledgment, check endorsement or other writing prepared by you, which terms are inconsistent with these terms and conditions or CCC's Billing and Payment terms and

conditions. These terms and conditions, together with CCC's Billing and Payment terms and conditions (which are incorporated herein), comprise the entire agreement between you and Springer Science + Business Media (and CCC) concerning this licensing transaction. In the event of any conflict between your obligations established by these terms and conditions and those established by CCC's Billing and Payment terms and conditions, these terms and conditions shall control.

Jurisdiction
All disputes that may arise in connection with this present License, or the breach thereof, shall be settled exclusively by arbitration, to be held in The Netherlands, in accordance with Dutch law, and to be conducted under the Rules of the 'Netherlands Arbitrage Instituut' (Netherlands Institute of Arbitration).***OR:***

All disputes that may arise in connection with this present License, or the breach thereof, shall be settled exclusively by arbitration, to be held in the Federal Republic of Germany, in accordance with German law.

Other terms and conditions:

v1.3

Questions? [redacted]@copyright.com or +[redacted](toll free in the US) or +[redacted].

Gratis licenses (referencing $0 in the Total field) are free. Please retain this printable license for your reference. No payment is required.

Permission for reproduction of work

Permission from American Physical Society

AMERICAN PHYSICAL SOCIETY

One Physics Ellipse, College Park, MD 20740 · http://www.aps.org

October 6, 2014
Farhana Baset
Department of Physics
University of Ottawa
Ottawa, ON K1N 6N5
Canada

Ref # 28265

Thank you for your permission request dated Sept. 22, 2014. We are pleased to grant you a non-exclusive, non-transferable permission, English rights, limited to **print and electronic format**, provided you meet the criteria outlined below. Permission is for a one-time use and does not include permission for future editions, updates, databases, translations, or any other matters. Permission must be sought for each additional use. This permission does not include the right to modify APS material.

Please print the required copyright credit line on the first page that the material appears: "Reprinted (abstract/excerpt/figure) with permission from [FULL REFERENCE CITATION] as follows: authors names, journal title, volume number, page number and year of publication. Copyright (YEAR) by the American Physical Society.

The following language must appear somewhere on the website: "Readers may view, browse, and/or download material for temporary copying purposes only, provided these uses are for noncommercial personal purposes. Except as provided by law, this material may not be further reproduced, distributed, transmitted, modified, adapted, performed, displayed, published, or sold in whole or part, without prior written permission from the American Physical Society."

Provide a hyperlink from the reprinted APS material (the hyperlink may be embedded in the copyright credit line). APS's link manager technology makes it convenient and easy to provide links to individual articles in APS journals. For information, see: http://link.aps.org/.

You must also obtain permission from at least one of the authors for each separate work, if you haven't done so already. The author's name and address can be found on the first page of the published Article.

Use of the APS material must not imply any endorsement by the American Physical Society.

Permission is granted for use of the following APS material only:

- Figs. 2 and 4, Phys. Rev. Lett. 96, 057404 – Published 7 February 2006

Permission is limited to the single title specified of the publication as follows:
A thesis entitled "Micro/nano-scale Manipulation of Material Properties" to be published by the University of Ottawa and the National Library of Canada.

If you have any questions, please refer to the Copyright FAQ at: http://publish.aps.org/copyrightFAQ.html or send an email to [redacted]@aps.org.

Sincerely,
Jamie L. Casey
Circulation and Fulfillment Assistant

Appendix C

Bibliography

Bibliography

[1] M. Stewart D. Ryan C. G. Willson B. D. Gates, Q. B. Xu and G. M. Whitesides. New approaches to nanofabrication: Molding, printing, and other techniques. *Chem. Rev.*, 105:1171–1196, 2005.

[2] P. F. Nealey J. D. Foley, E. W. Grunwald and C. J. Murphy. Cooperative modulation of neuritogenesis by pc12 cells by topography and nerve growth factor. *Biomaterials*, 26:3639–3644, 2005.

[3] C. R. Halberstadt W. He and K. E. Gonsalves. Lithography application of a novel photoresist for patterning of cells. *Biomaterials*, 25:2055–2063, 2004.

[4] Y. Xia and G. Whitesides. Soft lithography. *Annu. Rev. Mater. Sci.,*, 28:153–184, 1998.

[5] S. C. Chen G. Mapili, Y. Lu and K. Roy. Laser-layered microfabrication of spatially patterned functionalized tissue-engineering scaffolds. *J Biomed Res Part B: Appl Biomater*, 75B:414–424, 2005.

[6] A. J. Garcia W. P. King J. L. Charest, L. E. Bryant. Hot embossing for micropatterned cell substrates. *Biomaterials*, 25:4767–4775, 2004.

[7] T. H. Maiman. Stimulated optical radiation in ruby. *Nature*, 187:493–494, 1960.

[8] A. Gawande W. Z. Lin R. W. Schoenlein R. Birngruber, C. A. Puliafito and J. G. Fujimoto. Femtosecond laser tissue interactions - retinal injury studies. *IEEE J. Quantum Electron.*, 23:1836–1844, 1987.

[9] L. Huang R. J. Finlay T.-H. Her J. P. Callan E. N. Glezer, M. Milosavljevic and E. Mazur. Three-dimensional optical storage inside transparent materials. *Opt. Lett.*, 21:2023–2025, 1996.

[10] K. Itoh Y. Li, W. Watanabe and X. D. Sun. Holographic data storage on nonphotosensitive glass with a single femtosecond laser pulse. *Appl. Phys. Lett.*, 81:1952–1954, 2002.

[11] S. Nolte K. Itoh, W. Watanabe and C. B. Schaffer. Ultrafast processes for bulk modification of transparent materials. *Mrs Bulletin*, 31:620–625, 2006.

[12] N. Sugimoto K. M. Davis, K. Miura and K. Hirao. Writing waveguides in glass with a femtosecond laser. *Opt. Lett.*, 21:1729–1731, 1996.

[13] A. Brodeur C. Schaffer and E. Mazur. Laser induced breakdown and damage in bulk transparent materials induced by tightly focused femtosecond laser pulse. *Meas. Sci. Technol.*, 12:1784 – 1794, 2001.

[14] M. C. Nadeau S. Petit S. L. Chin A. Saliminia, N. T. Nguyen and R. Vallee. Writing optical waveguides in fused silica using 1 khz femtosecond infrared pulses. *J. Appl. Phys.*, 93:3724–3728, 2003.

[15] S. Mao C. Aguilar, Y. Lu and S. Chen. micro-patterning of biodegradable polymers using ultraviolet and femtosecond lasers. *Biomaterials*, 26:7642–7649, 2005.

[16] E. Andideh M. Khan D. Oslen I. Adesida, A.M. and J. Kuznia. Reactive ion etching of gan in silicon tetrachloride plasmas. *Appl. Phys. Lett.*, 63(20):2777–2779, 1993.

[17] J. Poate J. Borland M. Current T. Rubia D. Eaglesham O. Holland M. Law C. Magee J. Melngailis E. Chanson, S.P. and A. Tasch. Ion beams in silicon processing and characterization. *J. Appl. Phys.*, 81(10):6513–6561, 1997.

[18] C. Weng T. Fang and J. Chang. Machining characterization of the nano-lithography process using afm. *Nanotechnology*, 11:181–187, 2000.

[19] Y. Kim and C. Lieber. Machining oxide thine films with an afm: Pattern and object formation on the nanometer scale. *Science*, 257(5068):375–377, 1992.

[20] J.K. H. Klank and O. Geschke. Co2 laser micomachining and back end processing for rapid production of pmma based microfluidic systems. *Lab on a chip*, 2(4):242–246, 2002.

[21] J. Fost B. Seddon, Y. Shao and H. Girault. The application of excimer-laser micromachining for the fabrication of disc microelectrodes. *Electrochimica Acta*, 39(6):783–791, 1994.

[22] J. Ihlemann. Excimer laser micro machining of inorganic dielectrics. *Applied Surface Science*, 106:p. 282–286, 1996.

[23] C. David A. Wokaun G. Kopitkovas, T.L. and J. Gobrecht. Surface micromachining of uv transparent materials. *Thin solid films*, 453:31–35, 2004.

[24] E. Illy A. Glover and J. Piper. High speed uv micro machining of polymers with frequency doubled copper vaport lasers. *IEEE journal of quantum electronic*, 1(3):830–836, 1995.

[25] P. Daele K. Naessens, H.O. and R. Baets. Flexible fabrication of microlenses in polymer layers with excimer laser ablation. *Applied Surface Science*, 208-209:159–164, 2003.

[26] M. Withford E. Illy, D.B. and J. Piper. Enhanced polymer ablation rates using high-repetition-rate ultraviolet lasers. *IEEE journal of quantum electronic*, 5(6):1543–1548, 1999.

[27] R.P. H. Endert and D. Basting. Excimer laser: A new tool for precision micromachining. *Optical and Quantum electronics*, 27(12):1319–1335, 1995.

[28] D. Du X. Liu and G. Mourou. Laser ablation and micromachining with ultrashort laser pulses. *IEEE journal of quantum electronics*, 33(10):1706–1716, 1997.

[29] B. Luther-Davies E.G. Gamaly, A.V. Rode and V.T. Tikhonchuk. Ablation of solids by femtosecond lasers: ablation mechanism and ablation thresholds for metals and dielectrics. *Phys. of Plas.*, 9:949–957, 2002.

[30] K. Richardson A. Zoubir, L. Shah and M. Richardson. Practical uses of femtosecond laser micro-materials processing. *Appl. Phys. A*, 77:311–315, 2003.

[31] S. Herman A. M. Rubenchik B. W. Shore B. C. Stuart, M. D. Feit and M. D. Perry. Optical ablation by highpower short-pulse lasers. *J. Opt. Soc. Am. B*, 13(2):459468, 1996.

[32] R. M. Wood. *Laser Damage in Optical Materials.* Hilger, Boston, U.S.A., 1986.

[33] E. W. Van Stryland T. F. Boggess M. J. Soileau, W. E. Williams and A. L. Smirl. Temporal dependence of laserinduced breakdown in nacl and sio_2. *Natl. Bur. Stand. (U.S.) Spec. Publ.*, 669:387–405, 1984.

[34] S. Herman A. M. Rubenchik B. W. Shore B. C. Stuart, M. D. Feit and M. D. Perry. Nanosecond-to-femtosecond laser-induced breakdown in dielectrics. *Physical Review B*, 53:1749, 1996.

[35] S. Nolte F. von Alvensleben B. N. Chichkov, C. Momma and A. Tnnermann. Femtosecond, picoseconds and nanosecond laser ablation of solids. *Appl. Phys. A*, 63(2):109–115, 1996.

[36] X. Mao R. Russo and S. Mao. The physics of laser ablation in microchemical analysis. *Anal. Chem.*, 74:70 A–77 A, 2002.

[37] M. Vicanek A. Kaiser, B. Rethfeld and G. Simon. Microscopic processes in dielectrics under irradiation by subpicosecond laser pulses. *Phys. Rev. B*, 61:11437, 2000.

[38] T. Correll E. Gibb B. W. Smith J. D. Winefordner, I. B. Gornushkin and N. Omenetto. Comparing several atomic spectrometric methods to the super stars: special emphasis on laser induced breakdown spectroscopy (libs), a future super star. *J. Anal. At. Spectro.*, 19:1061–1083, 2004.

[39] A. Komashko M. Feit and A. Rubenchik. Ultra-short pulse laser interaction with transparent dielectrics. *Appl. Phys. A:Mater. Sci. Process.*, 79:1657–1661, 2004.

[40] S. Chin. From multiphoton to tunnel ionization. *Advances in Multi-Photon Processes and Spectroscopy*, 16:249, 2004.

[41] A. Brodeur and S. Chin. Band-gap dependence of the ultrafast white-light continuum. *Phys. Rev. Lett.*, 80:4406–4409, 1998.

[42] M. D. Shirk and P. A. Molian. A review of ultrashort pulsed laser ablation of materials. *J. Laser Appl.*, 10:18–28, 1998.

[43] T.L. G. Gibson and C. Rhodes. Tunneling ionization in the multiphoton regime. *Physical Review A*, 41(9):5049 – 5052, 1990.

[44] C. B. Schaffer. *Interaction of Femtosecond Laser Pulses with Transparent Materials.* PhD thesis, Harvard University, Cambridge, MA, 2001.

[45] G. Mainfray and G Manus. Multiphoton ionization of atoms. *Reports on progress in physics*, 54(10):1333 – 1372, 1991.

[46] M. Franco B. Lamouroux B. Prade S. Tzortzakis L. Sudrie, A. Couairon and A. Mysyrowicz. Femtosecond laser-induced damage and filamentary propagation in fused silica. *Phys. Rev. Lett.*, 89:186601, 2002.

[47] L. V. Keldysh. Ionization in the field of a strong electromagnetic wave. *Sov. Phys. JETP*, 20:1307–1314, 1965.

[48] R. T. Casper X. A. Shen S. C. Jones, P. Braunlich and P. Kelly. Recent progress on laser-induced modifications and intrinsic bulk damage of wide-gap optical-materials. *Opt. Eng.*, 28:1039–1068, 1989.

[49] S. Sartania C. Spielmann G. Mourou W. Kautek M. Lenzner, J. Kruger and F. Krausz. Femtosecond optical breakdown in dielectrics. *Physical Review Letters*, 80:4076, 1998.

[50] J.Kruger M. Lenzner, F. Krausz and W. Kantek. Photoablation with sub-10 fs laser pulses. *Appl. Sur. Sci.*, 154-155:11–16, 2000.

[51] Robert W. Boyd. *Nonlinear Optics*. Academic Press, Boston, U.S.A., 1992.

[52] H. Kapteyn M. Murnane A. Tien, S. Backus and G. Mourou. Short-pulse laser damage in transparent materials as a function of pulse duration. *Phys. Rev. Lett.*, 82:3883, 1999.

[53] G-B Ma D. Kim and G-Y Xiao. Theoretical studies on the threshold dependence of laser-induced damage. *J. of the Korean Phys. Society*, 32(1):60–63, 1997.

[54] X. Liu D. Du and G. Mourou. Reduction of multi-photon ionization in dielectrics due to collisions. *Appl. Phys. B*, 63:617–621, 1996.

[55] K. K. Thornber. Applications of scaling to problems in highfield electronic transport. *J. Appl. Phys.*, 52:279, 1981.

[56] M. Lenzner. Femtosecond laser-induced damage of dielectrics. *Internat. J. Modern Phys. B*, 13:1559–1578, 1999.

[57] A.M. Rubenchik B.W. Shore B.C. Stuart, M.D. Feit and M.D. Perry. Laser-induced damage in dielectrics with nanosecond to subpicosecond pulses. *Phys. Rev. Lett.*, 74:2248–2251, 1995.

[58] N. Bloembergen. Laser-induced electric breakdown in solids. *IEEE J. Sel. Top. Quant. Electron.*, 10:375386, 1974.

[59] Y. R. Shen. *The Principles of Nonlinear Optics*. Wiley, New York, U.S.A., 1984.

[60] E. Yablonovitch and N. Bloembergen. Avalanche ionization and the limiting diameter of filaments induced by light pulses in transparent media. *Phys. Rev. Lett.*, 29:907–910, 1972.

[61] J. Koch F. Korte and B. Chichkov. Formation of microbumps and nanojets on gold targets by femtosecond laser pulses. *Appl. Phys. A:Mater. Sci. Process.*, 79:879–881, 2004.

[62] S. Ebara Y. Yamashita, T. Yokomine and A. Shimizu. Heat transport analysis for femtosecond laser ablation with molecular dynamics-two temperature model method. *Fusion Eng. Des.*, 81:1695–1700, 2006.

[63] L. Jiang and H. L. Tsai. Femtosecond laser ablation: Challenges and opportunities. *Proceeding of NSF Workshop on Research Needs in Thermal Aspects of Material Removal*, pages 163–177, 2003.

[64] A. Harkin J. Ashmore H. A. Stone M. Shen A. Ben-Yakar, R. L. Byer and E. Mazur. Morphology of femtoseocnd laser ablated borosilicate glass surfaces. *Appl. Phys. Lett.*, 83:3030–2, 2003.

[65] S. Rathbone J. Wright W. Weaver S. Ameer-Beg, W. Perrie and H. Champoux. Femtosecond laser microstructuring of materials. *Appl. Surface Phys.*, 127129:87580, 1998.

[66] A. Thoss A. Rosenfeld G. Korn I. Hertel R. Stoian, M. Boyle and E. Campbell. Laser ablation of dielectrics with temporally shaped femtosecond pulses. *Appl. Phys. Lett.*, 80:353, 2002.

[67] H. L. Tsai L. Jiang. Materials removals during femtosecond laser non-thermal ablation of dielectrics. *Proceedings of IMECE*, pages 1–9, 2006.

[68] E. N. Glezer A. M. T. Kim C. B. Schaffer, N. Nishimura and E. Mazur. Dynamics of femtosecond laserinduced breakdown in water from femtoseconds to microseconds. *Opt. Express*, 10:196203, 2002.

[69] M. Sakakura and M. Terazima. Initial temporal and spatial changes of the refractive index induced by focused femtosecond pulsed laser irradiation inside a glass. *Phys. Rev. B*, 71:024113, 2005.

[70] S. K. Sundaram and E. Mazur. Inducing and probing non-thermal transitions in semiconductors using femtosecond laser pulses. *Nature Mater.*, 1:217224, 2002.

[71] M. Doing A Cavalieri D. von der Linde A. Oparin J. Mayer-ter-Vehn K. Sokolowski-Tinten, J. Bialkowski and S. I. Anisimov. Transient states of matter during short pulse laser ablation. *Phys. Rev. Lett.*, 81:224, 1998.

[72] D. von der Linde and K. Sokolowski-Tinten: . I (2000). The physical mechanisms of short-pulse laser ablation. *App. Surf. Sci.*, 154-155:1–10, 2000.

[73] C. Belin V. N. Tokarev, S. Lazare and D. Debarre. Viscous flow and ablation pressure phenomena in nanosecond uv laser irradiation of polymers. *Appl. Phys. A:Mater. Sci. Process.*, 79:717–720, 2004.

[74] Ph. Martin F. Ladieu and S. Guizard. Measuring thermal effects in femtosecond laser-induced breakdown of dielectrics. *Appl. Phys. Lett.*, 81:957, 2002.

[75] P. S. Banks M. D. Feit V. Yanovsky M. D. Perry, B. C. Stuart and A. M. Rubenc. Ultrashort-pulse laser machining of dielectric materials. *J. Appl. Phys.*, 85(9):6803–6810, 1999.

[76] A. Miotello and P. M. Ossi. *Laser-Surface Interactions for New Materials Production: Tailoring Structure and Properties*. Springer Verlag, 2009.

[77] L. J. Lewis P. Lorazo and M. Meunier. Short-pulse laser ablation of solids: From phase explosion to fragmentation. *Phys. Rev. Lett.*, 91:225502, 2003.

[78] D. Von Der Linde B. Rethfeld, K. Sokolowski-Tinten and S. Anisimov. Timescales in the response of materials to femtosecond laser excitation. *Appl. Phys. A*, 79:767–769, 2004.

[79] L. Zhigilei. Dynamics of the plume formation and parameters of the ejected clusters in short-pulse laser ablation. *Appl. Phys. A*, 76:339–350, 2003.

[80] R. R. Gattass and E. Mazur. Femtosecond laser micromachining in transparent materials. *Nat. Photonics*, 2:219 225, 2008.

[81] C. Hnatovsky E. Simova R. S. Taylor P. B. Corkum D. M. Rayner P. P. Rajeev, M. Gertsvolf and V. R. Bhardwaj. Transient nanoplasmonics inside dielectrics. *J. of Phys. B; Atomic Molecular and Optical Physics*, 40(11):S273–S282, 2007.

[82] N. Sugimoto K. M. Davis, K. Miura and K. Hirao. Writing waveguides in glass with a femtosecond laser. *Opt. Lett.*, 21:1729–1731, 1996.

[83] P. B. Corkum V. R. Bhardwaj, P. P. Rajeev and D. M. Rayner. Strong field ionization inside transparent solids. *Journal of Physics B Atomic Molecular and Optical Physics*, 39(13):S397–S407, 2006.

[84] P. Ballard D. Devaux R. Fabbro, J. Fournier and J. Virmont. Physical study of laser-produced plasma in confined geometry. *J. of Appl. Phys.*, 68(2):775–784, 1990.

[85] N. Sugimoto K. M. Davis, K. Miura and K. Hirao. Writing waveguides in glass with a femtosecond laser. *Opt. Lett.*, 21:1729–1731, 1996.

[86] E. Simova P. P. Rajeev D. M. Rayner R. S. Taylor, C. Hnatovsky and P. B. Corkum. Femtosecond laser erasing and rewriting of self-organized planar nanocracks in fused silica glass. *Opt. Lett.*, 32(19):2888–2890, 2007.

[87] E. Simova V. R. Bhardwaj D. M. Rayner C. Hnatovsky, R. S. Taylor and P. B. Corkum. Polarization selective etching in femtosecond laser-assisted microfluidic channel fabrication in fused silica. *Opt. Lett.*, 30:1867–1869, 2005.

[88] E. N. Glezer and E. Mazur. Ultrafast-laser driven micro-explosions in transparent materials. *Appl. Phys. Lett.*, 71:882–884, 1997.

[89] W. Perrie D. Liu A. Baum, P. J. Scully and V. Lucarini. Mechanisms of femtosecond laser-induced refractive index modification of poly(methyl methacrylate). *J. of the Opt. Society of America B*, 27:107, 2009.

[90] R. Martinez-Vazquez R. Ramponi S. Turri G. Cerullo S. M. Eaton, C. De Marco and R. Osellame. Femtosecond laser microstructuring for polymeric lab-on-chips. *J. Biophoton.*, 5:687702, 2012.

[91] N. R. Desai D. L. N. Kallepalli and V. R. Soma. Fabrication and optical characterization of microstructures in poly(methylmethacrylate) and poly(dimethylsiloxane)

using femtosecond pulses for photonic and microfluidic applications. *Applied Optics*, 49(13):2475, 2010.

[92] E. Hecht. *Optics*. 4th edition edition, 2001.

[93] M. E. Heller A. H. Firester and P. Sheng. Knife-edge scanning measurements of subwave- length focused light beams. *Appl. Opt.*, 16:1971–1974, 1977.

[94] J. M. Khosrofian and B. A. Garetz. Measurement of a gaussian laser beam diameter through the direct inversion of knife-edge data. *Appl. Opt.*, 22:3406–3410, 1983.

[95] H. R. Bilger and T. Habib. Knife-edge scanning of an astigmatic gaussian beam. *Appl. Opt.*, 24:686–690, 1985.

[96] J. M. Liu. Simple technique for measurements of pulsed gaussian-beam spot sizes. *Opt. Lett.*, 7:196–198, 1982.

[97] J. Kruger S. Baudach, J. Bonse and W. Kautek. Ultrashort pulse laser ablation of polycarbonate and polymethylmethacrylate. *Applied Surface Science*, pages 3–8, 2000.

[98] H. D. Hoffmann H. G. Treusch J. Jandeleit, G. Urbasch and E. W. Kreutz. Picosecond laser ablation of thin copper films. *Appl. Phys. A*, 63(2):117–121, 1996.

[99] J. KrUger J. Bonse, J. M. Wrobel and W. Kautek. Ultrashort pulse laser ablation of indium phosphide in air. *Appl. Phys. A*, 72:89–94, 2001.

[100] E. G. Gamaly. The physics of ultra-short laser interaction with solids at non-relativistic intensities. *Physics Reports*, 508(4):91–243, 2011.

[101] J. C. Diels and W. Rudolph. Ultrashort laser pulse phenomena. *Academic Press*, 36, 2006.

[102] R. Trebino. *Frequency-Resolved Optical Grating: The Measurement of Ultrashort Laser Pulses*. Kluwer Academic Publishers, Boston, U.S.A., 2006.

[103] R. Paschotta. *Encyclopedia of Laser Physics and Technology*. Wiley-VCH, 2008.

[104] D. S. Ivanov and L. V. Zhigilei. Combined atomistic-continuum modeling of short-pulse laser melting and disintegration of metal lms. *Phys. Rev. B*, 68:064114, 2003.

[105] A. Q. Wu C. Cheng and X. Xu. Molecular dynamics simulation of ultrashort laser ablation of fused silica. *J. Phys: Conference Series*, 59:100–104, 2007.

[106] Hagness S. C. Taflove, A. and. *Computational Electrodynamics: The Finite-Difference Time-Domain Method*. Artech House Inc, Boston, U.S.A., 3rd edition, 2005.

[107] D.B. Davidson. *Computational Electromagnetics for RF and Microwave Engineering*. Cambridge University Press, 2011, 2nd edition.

[108] K. Briggs S. Mack K. I. Popov, C. McElcheran and L. Ramunno. Morphology of femtosecond laser modication of bulk dielectrics. *Opt. Exp.*, 19(1):271–282, 2011.

[109] S. Wang H. Xiao Y. Lu L. Zhao, L. Jiang and H. L. Tsai. A high-quality mach-zehnder interferometer fiber sensor by femtosecond laser one-step processing. *Sensors (Basel Switzerland)*, 11(1):5461, 2011.

[110] D. N. Wang S. Liu Y. Wang, M. Yang and P. Lu. Fiber in-line mach-zehnder interferometer fabricated by femtosecond laser micromachining for refractive index measurement with high sensitivity. *J. Opt. Soc. Am. B*, 27(3):370374, 2010.

[111] H. L. Tsai T. Wei, Y. Han and H. Xiao. Miniaturized fiber inline fabry-perot interferometer fabricated with a femtosecond laser. *Opt. Lett.*, 33(6):536538, 2008.

[112] D .W. Duan X. C. Yang T. Zhu Y. J. Rao, M. Deng and G. H. Cheng. Micro fabry-perot interferometers in silica fibers machined by femtosecond laser. *Opt. Express*, 15:14123–14128, 2007.

[113] F. Baset X. Bao P. Lu, Y. Xu and R. Bhardwaj. In-line fiber microcantilever vibration sensor. *Applied Physics Letters*, 103:211113, 2013.

[114] M. Stoytchev A. A. Chabanov and A. Genack. Statistical signatures of photon localization. *Nature*, 404:850–853, 2000.

[115] C. Vanneste and P. Sebbah. Selective excitation of localized modes in active random media. *Physical Review Letters*, 87:183903, 2001.

[116] J. Y. Xu C. Q. Cao H. Cao, Y. Ling and P. Kumar. Photon statistics of random lasers with resonant feedback. *Physical Review Letters*, 86:4524–4527, 2001.

[117] H. Cao A. L. Burin, M. A. Ratner and R. P. H. Chang. Model for a random laser. *Physical Review Letters*, 87:215503, 2001.

[118] H. Cao. Lasing in random media. *Waves in Random Media*, 13:R1–R39, 2003.

[119] M. Noginov. *Solid-state random lasers*, volume 105. Springer, New York, U. S. A., 2005.

[120] C. Conti M. Leonetti and C. Lopez. The mode-locking transition of random lasers. *Nat. Photon*, 5:615–617, 2011.

[121] V. Letokhov. Generation of light by a scattering medium with negative resonance absorption. *Soviet Journal of Experimental and Theoretical Physics*, 26:835, 1968.

[122] P. G. Kryukov R. V. Ambartsumyan, N. G. Basov and V. S. Letokhov. A laser with a nonresonant feedback. *Quantum Electronics, IEEE*, 2:442–446, 1966.

[123] M. P. van Albada D. S. Wiersma and A. Lagendijk. Random laser? *Nature*, 373:203–204, 1995.

[124] D. S. Wiersma and A. Lagendijk. Light diffusion with gain and random lasers. *Physical Review E*, 54:4256, 1996.

[125] N. Lawandy and R. Balachandran. Random laser? *Nature*, 373:204, 1995.

[126] R. Torre S. Mujumdar, M. Ricci and D. S. Wiersma. Amplified extended modes in random lasers. *Physical Review Letters*, 93:053903, 2004.

[127] R. C. Polson and Z. V. Vardeny. Random lasing in human tissues. *Applied Physics Letters*, 85:1289–1291, 2004.

[128] M. A. Choma B. Redding and H. Cao. Speckle-free laser imaging using random laser illumination. *Nat. Photonics*, 6:496–496, 2012.

[129] A. S. L. Gomes N. M. Lawandy, R. M. Balachandran and E. Sauvain. Laser action in strongly scattering media. *Nature*, 368:436–438, 1994.

[130] M. Gagn and R. Kashyap. Demonstration of a 3 mw threshold er-doped random fiber laser based on a unique fiber bragg grating. *Opt. Express*, 17:19067–19074, 2009.

[131] E. I. Chaikina T. A. Leskova N. Lizrraga, N. P. Puente and E. R. Mndez. Single-mode er-doped fiber random laser with distributed bragg grating feedback. *Opt. Express*, 17:395–404, 2009.

[132] H. Cao A. L. Burin, M. A. Ratner and S. H. Chang. Random laser in one dimension. *Physical Review Letters*, 88:093904, 2002.

[133] A. M. Brito-Silva M. A. M. Gamez A. S. L. Gomes C. J. S. de Matos, L. D. S. Menezes and C. B. De Araujo. Random fiber laser. *Physical Review Letters*, 99:153903, 2007.

[134] V. Milner and A. Z. Genack. Photon localization laser: Low-threshold lasing in a random amplifying layered medium via wave localization. *Physical Review Letters*, 94:073901, 2005.

[135] T. Wang Q. Fu D. Zhang H. Ming Z. Hu, B. Miao and Q. Zhang. Disordered microstructure polymer optical fiber for stabilized coherent random fiber laser. *Optics Letters*, 38:4644–4647, 2013.

[136] X. Bao M. Pang and L. Chen. Observation of narrow linewidth spikes in the coherent brillouin random fiber laser. *Optics Letters*, 38:1866–1868, 2013.

[137] P. Harper E. V. Podivilov S. A. Babin, A. E. El-Taher and S. K. Turitsyn. Tunable random fiber laser. *Physical Review A*, 84:021805, 2011.

[138] A. E. El-Taher P. Harper-D. V. Churkin S. I. Kablukov J. D. Ania-Castan V. Karalekas S. K. Turitsyn, S. A. Babin and E. V. Podivilov. Random distributed feedback fibre laser. *Nat. Photon*, 4:231–235, 2010.

[139] Y. Hu Y. Kaneda S. Jiang C. Spiegelberg, J. Geng and N. Peyghambarian. Low-noise narrow-linewidth fiber laser at 1550 nm. *Journal of Lightwave Technology*, 22:57, 2004.

[140] A. L. Schawlow and C. H. Townes. Infrared and optical masers. *Physical Review*, 112:1940–1949, 1958.

[141] G. A. Cranch and G. A. Miller. Fundamental frequency noise properties of extended cavity erbium fiber lasers. *Opt. Lett.*, 36:906–908, 2011.

[142] R. R. Gattass and E. Mazur. Femtosecond laser micromachining in transparent materials. *Nat. Photonics*, 2:219–225, 2008.